GREENHOUSE GAS CATALYTIC REFORMING TO SYNGAS

A thesis submitted in partial fulfillment of the requirements for the degree of
Master of Science
Earth Resources Engineering

NOAH W. WHITMORE

Dr. Marco J. Castaldi, Advisor
Dr. Robert Farrauto, Advisor

Department of Earth and Environmental Engineering (HKSM)
Fu Foundation School of Engineering and Applied Science
Columbia University in the City of New York

May, 2007

ACKNOWLEDGEMENTS

I would to thank Dr. Castaldi for allowing me to engage in fundamental and socially relevant research and for cultivating a research environment which promotes student growth. I would like to thank Dr. Farrauto for his guidance and support through my duration at Columbia. Also, I wish to acknowledge soon-to-be Dr. Eilhann Kwon for his assistance and advising in the lab. Finally, I'd like to acknowledge my family and friends in the Pacific Northwest whom I've missed over the past two years.

TABLE OF CONTENTS

GREENHOUSE GAS CATALYTIC REFORMING TO SYNGAS

CMASS TECHNOLOGY DEMONSTRATIONS

1. LANDFILL GAS TO ENERGY

In the United States, approximately 1 ton of municipal solid waste (MSW) is generated per person per year [1]. Of this waste, approximately 22 % is recycled, 14 % is combusted in waste-to-energy facilities, and 55 % is landfilled [2]. When MSW is deposited at a landfill, it decomposes anaerobically via the simplified reaction

$$C_6H_{10}O_4 + 1.5H_2O = 3.25CH_4 + 2.75CO_2,$$

generating a gaseous mixture of roughly 50 % methane and 50 % carbon dioxide by volume, as well as trace amounts of volatile organic compounds [2]. Untreated, landfill gas poses various environmental concerns; captured, LFG is a local renewable energy source. While approximately 2.6 million tons of methane is captured annually from landfills in the United States, 70 % of which is used to generate heat or electricity [3], efficient utilization of LFG is an area for research and development.

1.1 Landfill gas: an environmental hazard.

Landfill gas, if not flared or utilized, poses an explosion hazard, is an emission source of volatile organic compounds (VOCs), and is composed primarily of potent greenhouse gases [1]. The VOCs with the greatest concentrations in LFG are toluene and dichloromethane at respective levels of 26 and 35 ppm, and the total amount of non-captured VOCs is approximately 2350 tons per year [2]. Landfills are also the largest source of anthropogenic methane emissions in the United States [4], producing 7.2 billion Nm^3 per year [2]. Currently, only 4.3 billion Nm^3 is captured, resulting in atmospheric emissions of 2.9 billion Nm^3 per year [2]. It is estimated that the global warming potential of methane is 23 times greater than an equal volume of carbon dioxide [5], so the successful capture and conversion of CH_4 to produce energy and its less

potent products of combustion, or to CO and H_2 to be used for chemical synthesis, rapidly reduces the global warming impact. Methane lost from landfills in the US is equivalent to 35.7 million tons atmospheric carbon per year, or 2 % of the total US anthropogenic carbon emissions. In addition to this uncaptured methane released from landfills are 3.29 millions tons carbon in the form of uncaptured CO_2, and 2.3 million tons carbon equivalent from the successful combustion of captured CH_4 [2]. While it is clear that improvements in the percentage of captured methane will yield the greatest reductions in global warming impact from landfills, more efficient utilization of captured LFG as a renewable energy source is an intriguing area for research and development.

1.2 Landfill gas: a renewable energy resource.

Landfill gas is a low-cost, local, renewable energy resource. Two viable methods of LFG usage are direct combustion on or near a landfill site and conversion of the LFG to syngas which can then be further converted to a liquid fuel for distribution. While LFG is a low-to-medium-BTU gas with an average heating value of 540 kJ/Nm^3, it contains enough chemical energy to sustain the operation of a gas turbine or internal combustion engine, and can be used to produce heat and power. The presence of a significant amount of CO_2 in the mixture means that the flame characteristics are substantially different from those of natural gas. The result is reduced flame temperatures and burning rates, and a narrower range of flame stability, yielding lower combustion efficiency [6]. Further, the high concentration of CO_2 increases the amount of NO_x produced per gram of CH_4 through enhancement of the prompt mechanism [6]. One way to increase the combustion efficiency is to recuperate some of the thermal energy of the products of combustion to pre-heat the reactants, increasing the temperature in the reaction zone. Another approach would be to raise the heating value of the reactants by adding a high-grade fuel to the

mixture. Hydrogen enhanced combustion would provide the benefits of reducing undesired emissions, allow ignition at lean conditions and low temperatures, and provide flame stability at low temperatures. However, a high fraction of hydrogen fuel would typically result in higher costs if hydrogen is produced and purchased off-site.

As mentioned above, landfill gas can also be reformed catalytically to syngas (hydrogen and carbon monoxide) via the dry reforming reaction:

$$CH_4 + CO_2 \rightarrow 2CO + 2H_2 \; ; \quad \Delta H_{298} = +247 \text{ kJ/mol}$$

While this process is currently an area for continuing research in catalysis, recent studies, including this work, suggest that Rhodium or Nickel based catalysts may be formulated for this process and could be commercially available for use in the near future.

To illustrate ideal combustion performance characteristics for various degrees of landfill gas reforming, adiabatic flame temperatures were calculated for varying equivalence ratios, along with the stoichiometric enthalpy of combustion of the various fuel compositions in Figure 1.1. As the syngas content in LFG increases, the adiabatic flame temperature increases, as does the zone of high flame temperature with respect to equivalence ratio.

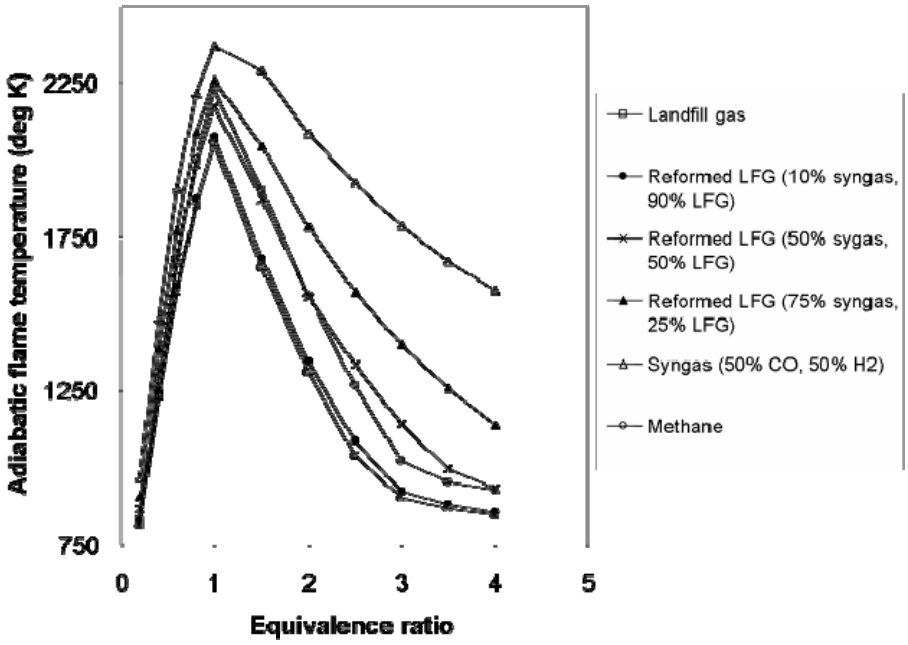

(a)

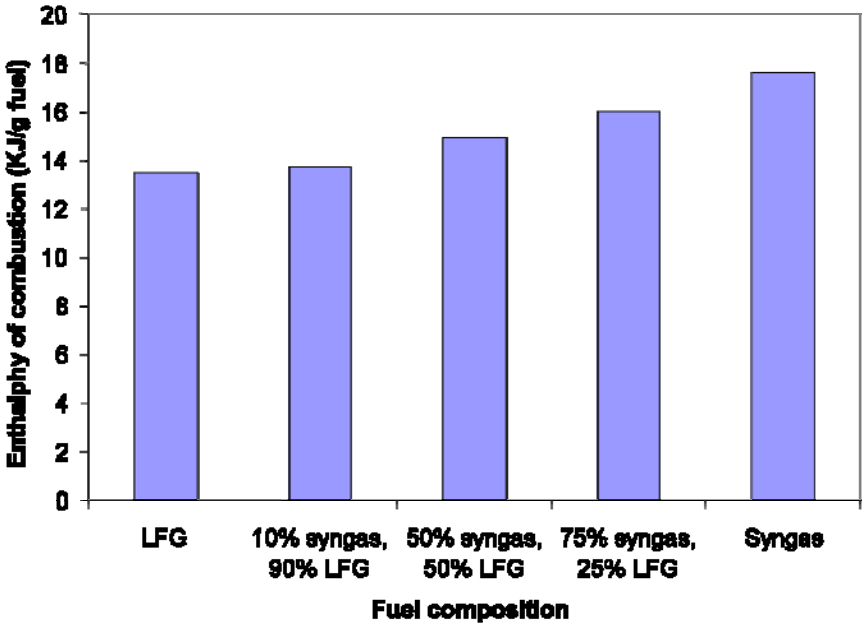

(b)

Fig. 1.1. (a) Adiabatic flame temperature is shown versus equivalence ratio for various fuel compositions with air as the oxidant. (b) Enthalpies of combustion are shown for various fuel compositions at stoichiometric air:fuel ratios where the fuel is considered to be the mix of LFG and syngas.

1.3 Scaling: estimations of gas flow rates from landfills.

The amount of LFG that is generated from a landfill is primarily affected by the amount of solid waste in place, the depth of the landfill, the age of the landfill, the type of waste, the rate at which the landfill receives waste, and the amount of precipitation the landfill receives (EPA). In arid climates which receive less than about 25 inches of rain per year, the gas flow rate is likely to be low, but may continue for a longer period of time than for moist climates [1]. Taking an average of reported industrial values for different landfills in the United States, about 5.7 m^3 of landfill gas is produced per ton of MSW in place per year [1]. Therefore, a rough estimate of the gas flow from a 5 million ton landfill would be 28.5 million m^3/yr.

A first-order decay model can be used to account for changing gas flow rates during the lifetime of a landfill (EPA). Where Q is the amount of landfill gas generated per year (m^3/yr), C_0 is the total methane generation potential of the waste (m^3/ton), R is the average waste disposal rate during the years which the landfill is open (tons/yr), f is the fraction of landfill gas captured, k is the rate of methane generation (1/yr), t_0 is the time since the landfill was opened (yr), and t_c is the time since the landfill was closed (yr), a model can be generated to estimate the flow rate of captured gas at a particular point in time:

$$Q = 2\, f\, C_0\, R\, (\exp(-kt_c)-\exp(-kt_0))$$

The total methane generation potential C_0 is dependent on the type of waste, but an average can be taken as approximately 150 m^3/ton. The rate of methane generation k depends on climate, but an average can be taken as 0.05/yr for a medium moisture climate. So, given an average rate of MSW disposal and the time of operation of the landfill, a gas flow rate can be estimated, as shown in Figure 1.2.

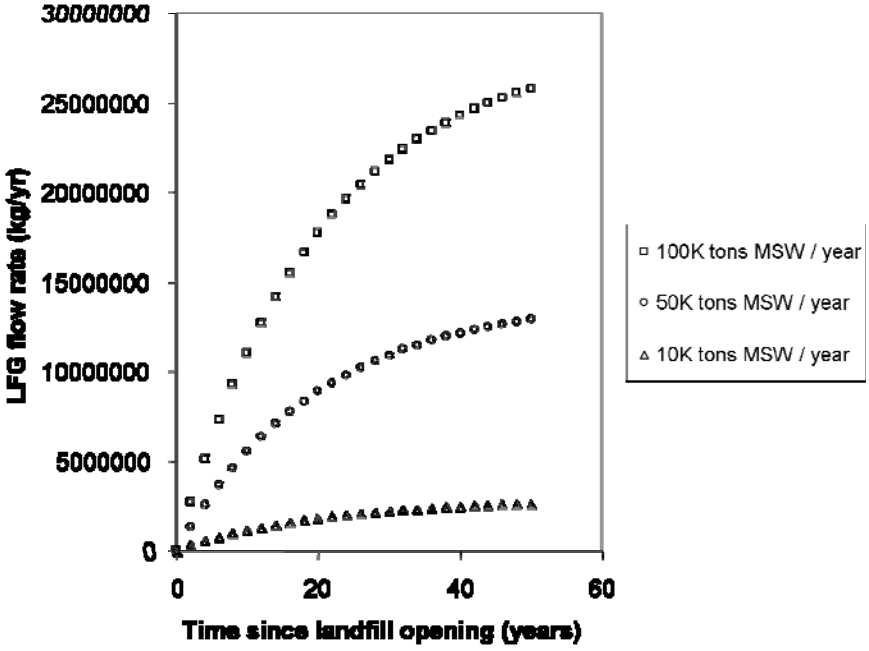

(a)

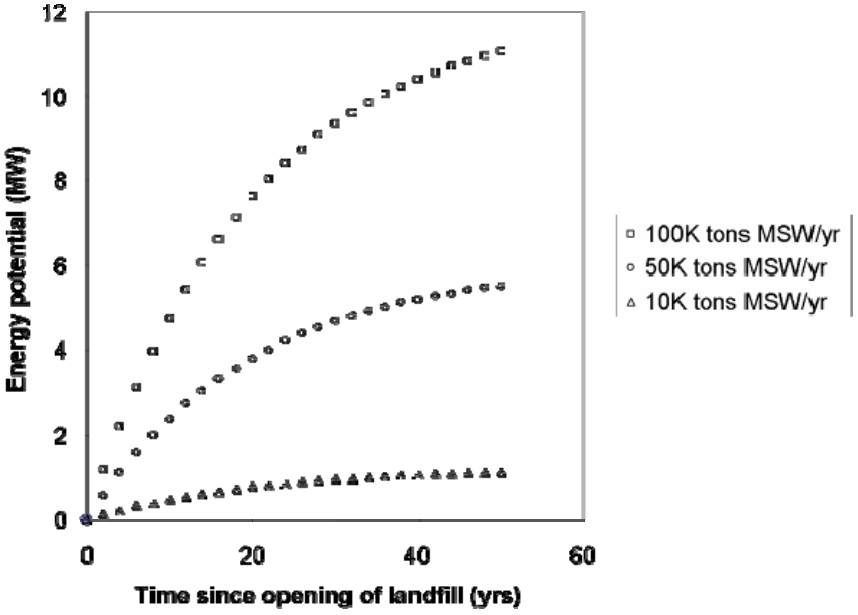

(b)

Fig. 1.2. (a) Landfill gas flow rate versus length of time since the landfill has been in operation for different rates of MSW deposition. An estimated fraction of 75 percent gas capture was used, along with C_0 and k values of 150 m^3/ton and 0.05/yr, respectively. (b) Energy potential (based on the LHV) of the generated landfill gas is shown versus time following the same assumptions as in (a).

1.4 Energy conversion: alternative options.

Several technologies exist which are suitable for either direct use or power production and cogeneration from landfill gas. Depending on several different factors, such as the size of the landfill, the presence of an existing energy market, project costs, and potential revenue sources, any given recovery system may be most suitable for a particular landfill.

1.4.1 Direct use: sale of landfill gas for small scale boiler applications

One simple and cost effective method to utilize landfill gas is to sell the gas as a low-Btu fuel for boiler or industrial process use where heat is needed. In this case, the major capital cost lies in the construction of a pipeline for the customer to access the supply. This cost may range between $250,000 to $500,000 per mile. In addition, if landfill gas is used directly in a boiler application, the cost of retrofitting a boiler can range from $120,000 - $300,000 for boilers from 10,000 to 80,000 lb/hr. Once the retrofits are made to the boiler, the operating and maintenance costs are similar to the costs of using conventional fuels. Additionally, the need to retrofit, which is caused by the low-Btu value of the fuel, may be avoided through reforming the fuel to a mixture of synthesis gas.

1.4.2 Cogeneration: internal combustion engine with combined heat and power:

The internal combustion engine is the most widely used conversion technology in landfill gas applications. This is due to the relatively high efficiency, low cost, and good size match for many landfills, which commonly produce between 1 and 3 MW. The efficiency of an engine modified for landfill gas use sacrifices less than 5 percent when compared to a natural gas engine, and when waste heat is recovered from the engine cooling jacket and lube system to make hot water, as well as from the engine exhaust to make low pressure steam, efficiencies

increase dramatically. The capital costs for internal combustion engine projects are approximately $1,200 per kW output.

1.4.3 Cogeneration: gas turbine with combined heat and power

As the size of the landfill increases, and electricity production increases to around 5 MW, it becomes more cost-effective to use a gas turbine, taking advantage of the economies of scale of the technology. The gas turbine cycle is especially useful to utilize exhaust heat to produce steam and heat for reforming and heating applications. Capital cost estimates range from about $1,200 – 17,000 per kW for landfills from 1-10 million tons. A schematic of the gas turbine with combined heat and power and reformer is shown in Fig. 1.3.

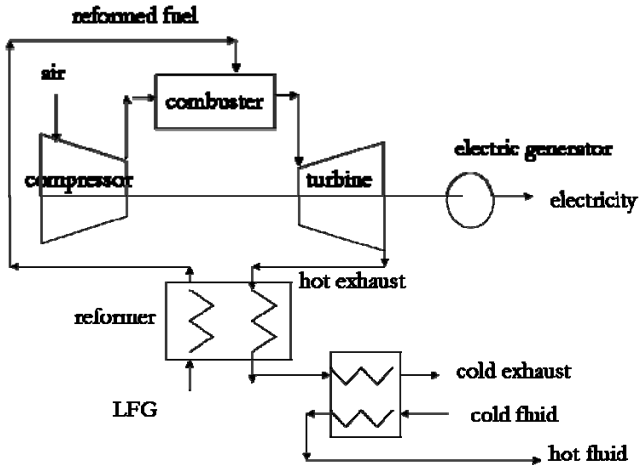

Fig. 1.3. Schematic of gas turbine with combined heat and power and reforming technology.

1.4.4 Cogeneration: fuel cell with combined heat and power

Another promising energy conversion technology is the fuel cell, which offers a high ideal efficiency, small size and quiet operation, and flexibility with regard to sizing. However, fuel cell systems are still in the development phase and their cost-effectiveness is currently low. Nonetheless, it is worthwhile to determine the efficiency of a fuel cell system, assuming that the

cost comes down and some basic engineering issues become resolved in the near future. A common fuel cell, the proton exchange membrane fuel cell, runs on hydrogen and oxygen, and could be used to provide electricity from fully reformed landfill gas, as long as the carbon monoxide is reduced to a level of 10 ppm before the fuel mixture reaches the fuel cell. A schematic of the fuel cell system is shown in Figure 1.4.

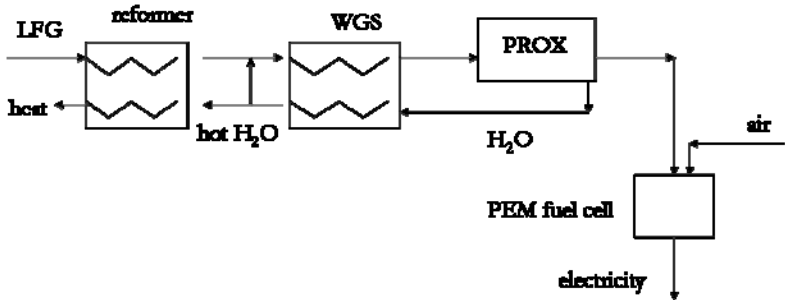

Fig. 1.4. Schematic of fuel cell system to convert landfill gas into electricity and useable heat.

1.5 System efficiencies and energy production

Electrical production, electrical efficiency, and overall combined heat and power efficiencies were calculated for varying extents of reforming and various energy conversion technologies. Calculations were performed for two different sizes of open landfills. A capture factor of 75 % was included, which is reflected in the overall electricity production, but not in the efficiencies of the energy conversion systems. Electrical efficiency was defined as the ratio of electrical work output to the total lower heating value of the captured landfill gas. Overall combined heat and power efficiency was defined as the ratio of combined electricity and leftover heat available divided by the lower heating value of the captured landfill gas.

As seen in Figures 1.5 and 1.6, electricity generation and efficiency increases as the percent of reformed landfill gas increases. The internal combustion engine is more efficient than the gas turbine in this regime of power production, but the fuel cell system provides the greatest potential for electricity production. However, if you consider only the hydrogen generated from the reformed methane and CO_2 molecules, as the electricity carrier for the system, the efficiency decreases by about a factor of two. The water gas shift reaction serves to double the amount of hydrogen in the system, as well as add heat to the system, increasing electrical and overall combined heat and power efficiencies to very high values.

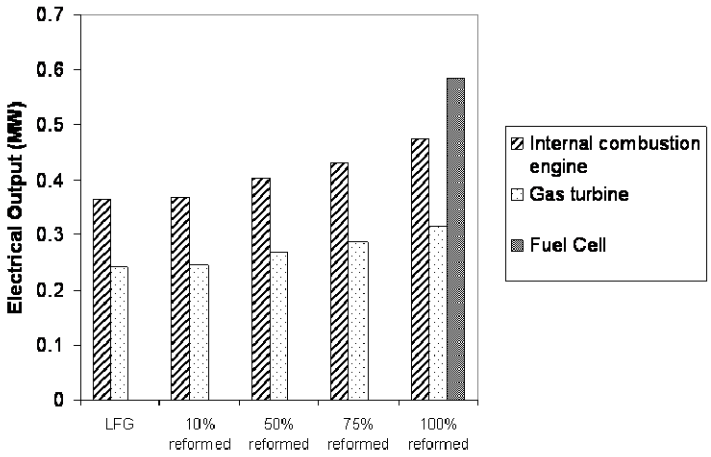

(a)

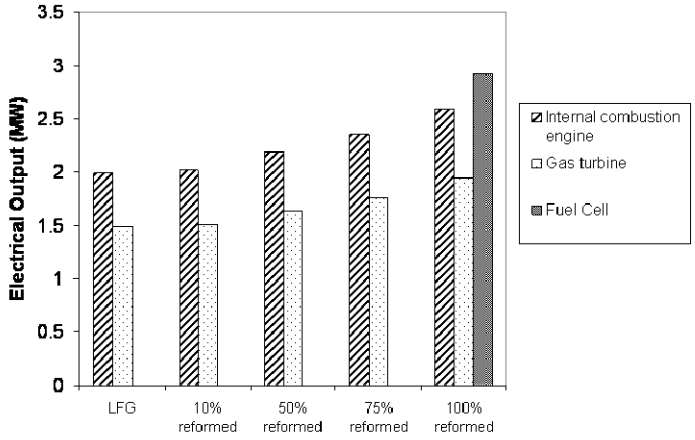

(b)

Fig. 1.5. Electricity generation is shown for different fuel compositions and energy conversion systems for a 0.5 megaton landfill (a), and for a 2.5 megaton landfill (b).

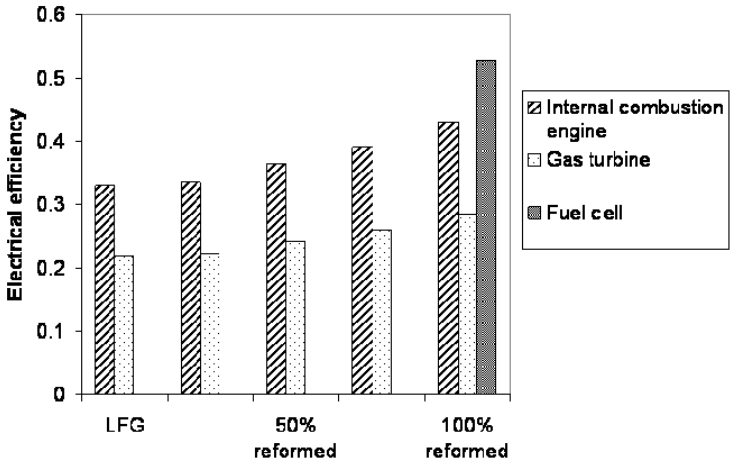

(a)

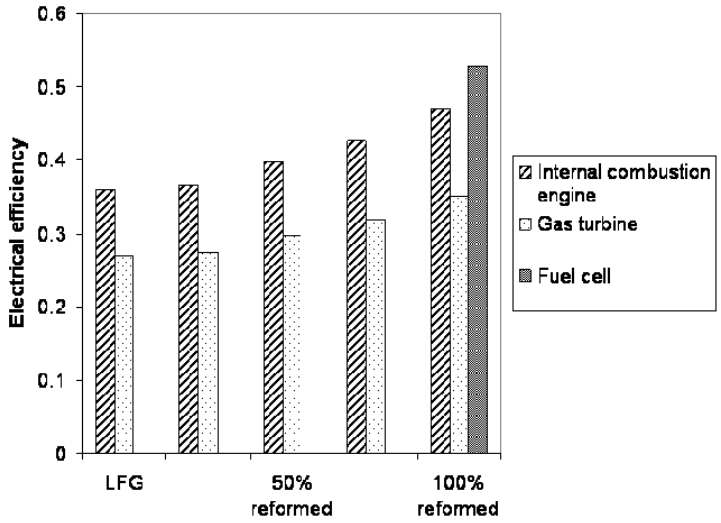

(b)

Fig. 1.6. Electrical efficiency is shown for different fuel compositions and energy conversion systems for a 0.5 megaton landfill (a), and for a 2.5 megaton landfill (b).

While the electrical efficiency increases with increasing synthesis gas content, overall combined heat and power efficiency declines. This is due to the fact that the waste heat that would

otherwise be available must be used to supply the heat for the highly endothermic reforming reaction.

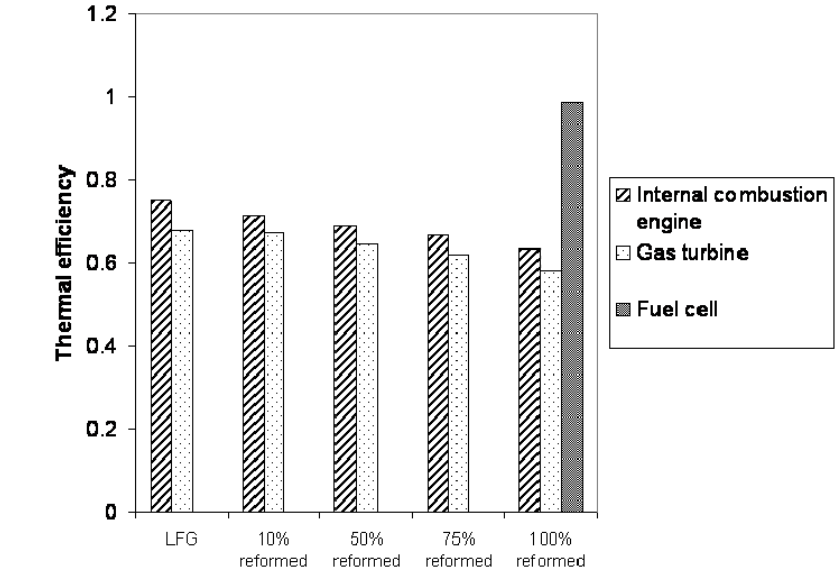

(a)

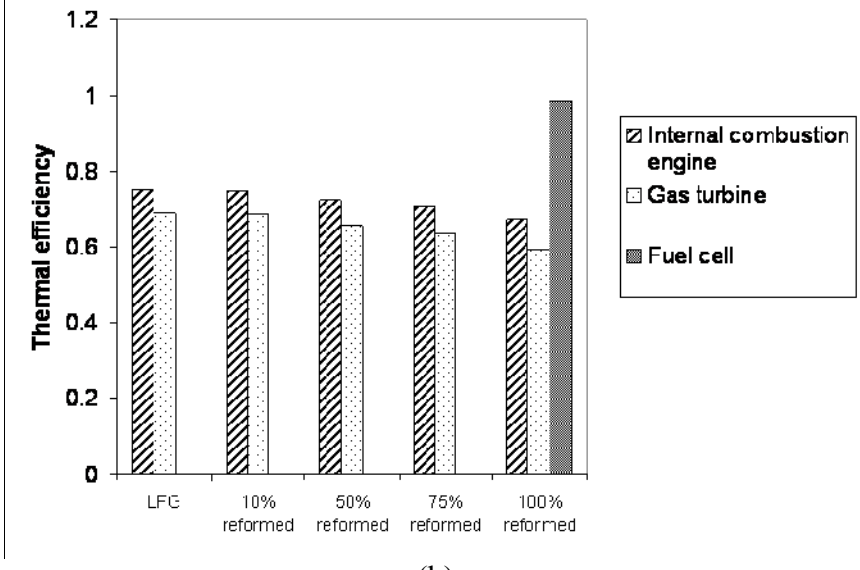

(b)

Fig. 1.7. Overall thermal efficiency is shown for different fuel compositions and energy conversion systems for a 0.5 megaton landfill (a), and for a 2.5 megaton landfill (b).

From the standpoint of generating electricity, high degrees of reforming make sense. If waste heat is a valuable commodity, using the landfill gas as-is is most efficient, not considering the fuel cell system.

Using the electricity production generated from a 2.5 megaton landfill under the fuel cell system as a basis for scaling, electricity potential from United States municipal solid waste production is on the order of 16.5 GW. This represents approximately almost 4 % of the approximately 400 GW electricity demanded in the Unites States. At this scaling, the potential for electricity generation from landfills should not be ignored.

Alternative waste management involves the direct combustion of municipal solid waste in mass burn facilities. While the landfill gas to energy system produces about 370 kWh electricity and 330 kWh heat per ton MSW at peak production, highly efficient waste-to-energy facilities generate 302 kWh net electricity and 878 kWh heat per ton MSW. As the direct combustion method employed by waste-to-energy facilities also provides a substantial land-use advantage, the waste-to-energy approach is probably a more effective approach to generating useable energy from MSW. But, as the current MSW management practice in the US involves landfilling 55 % of the total MSW generated, LFG is a significant source of renewable energy to be utilized, and the development and commercialization of a reforming technology would serve to vastly improve the efficiency of LFG utilization.

2. DRY REFORMING TECHNOLOGY

The development of stable dry reforming technology is attractive for social, environmental, and economical reasons, and is suited for many applications. Aside from LFG utilization, the reaction is an attractive route to produce syngas with low H_2:CO ratios and is also well-suited for use in chemical energy transmission systems (CETS).

Syngas is typically produced via steam methane reforming or methane partial oxidation, resulting in high H_2:CO ratios.

$$CH_4 + H_2O \rightarrow CO + 3H_2 \; ; \; \Delta H_{298} = +206 \text{ kJ/mol}$$

$$CH_4 + \tfrac{1}{2} O_2 \rightarrow CO + 2H_2 \; ; \; \Delta H_{298} = -71 \text{ kJ/mol}$$

However, synthesis of methanol and long-chain liquid hydrocarbons via the Fischer-Tropsch process, which use syngas as the starting feedstock, would be more efficient if conducted with syngas of low H_2:CO ratios. For these end uses, the dry reforming reaction is a more advantageous route to generate syngas.

The high endothermicity of the dry reforming reaction also makes it suitable to store abundant thermal solar or nuclear energy as chemical energy in chemical energy transmission systems (CETS), shown in Fig 2.1.

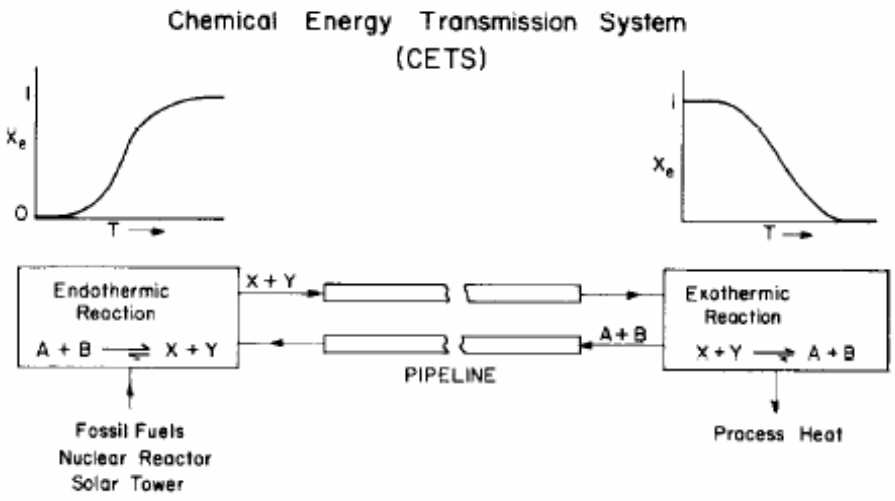

Fig. 2.1. Diagram of chemical energy transmission system [7].

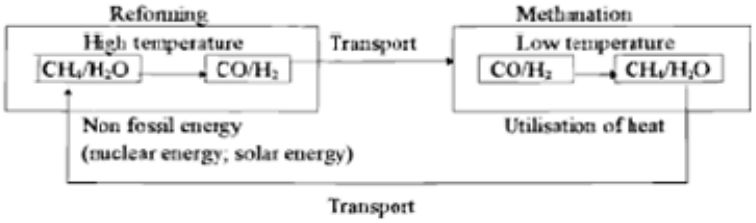

Fig 2.2. Diagram of the steam reforming-methanation CETS, known as the Eva-Adam process [8].

Under the CETS scheme, abundant thermal energy from solar, nuclear, or fossil fuel sources is used to drive a reversible endothermic reforming reaction to equilibrium. The gaseous products can then be stored or transported off-site. When energy is needed, the reverse, exothermic reaction can be driven to equilibrium, generating process heat. The products of the exothermic reaction can then be recycled back to the original reactor to be reformed once again through the aid of the abundant thermal energy source. This process, when conducted with steam methane reforming-methanation, is known as the Eva-Adam process (Fig 2.2) and has been established in Germany, the US, Israel, and the former Soviet Union. However, dry reforming would be superior to steam reforming in terms of a CETS due to the fact that all species are in gas phase at atmospheric conditions, making transport and recycling of the species easier. In addition, the dry

reforming is energetically superior. The major disadvantage lies in the thermodynamic tendency for coke formation during the dry reforming reaction, deactivating the catalyst.

Thermodynamics

Occurring simultaneously with the dry reforming reaction are side reactions which may cause the formation of coke or alter the relative concentrations of species being produced. One possible side reaction is the reverse of the water-gas-shift (WGS) reaction:

$$CO + H_2O \rightarrow CO_2 + H_2 \qquad \text{(WGS)}$$

In addition, there are several side reactions to consider which may result in coke formation, including:

$$2CO \rightarrow C + CO_2 \qquad \text{(CO disproportionation)}$$

$$CO + H_2 \rightarrow C + H_2O \quad \text{(CO reduction)}$$

$$CH_4 \rightarrow C + 2H_2 \qquad (CH_4 \text{ decomposition})$$

To gauge the thermodynamic tendency for these reactions to occur, the change in Gibbs free energy was plotted versus temperature for the different reactions.

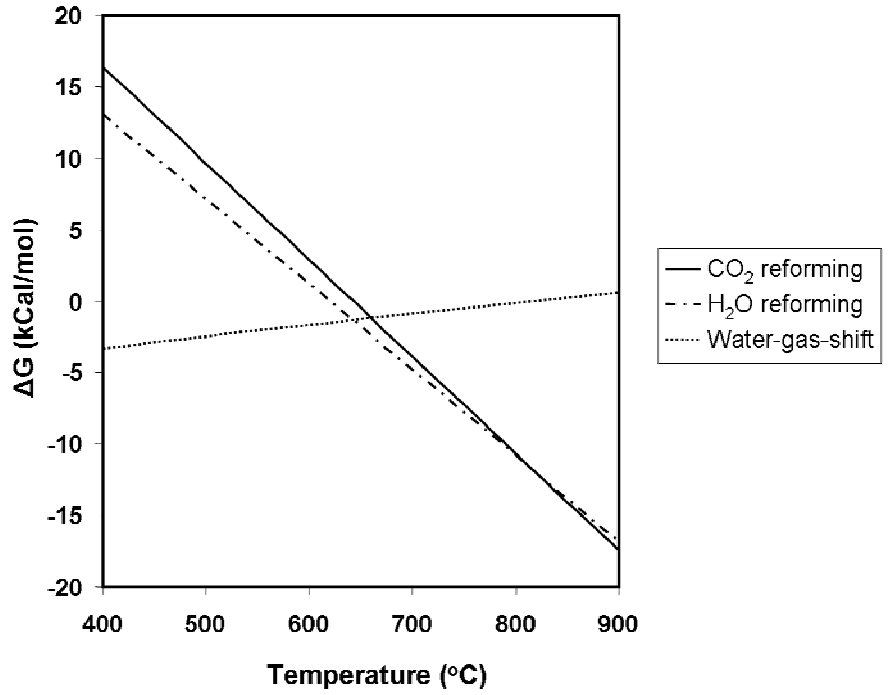

(a)

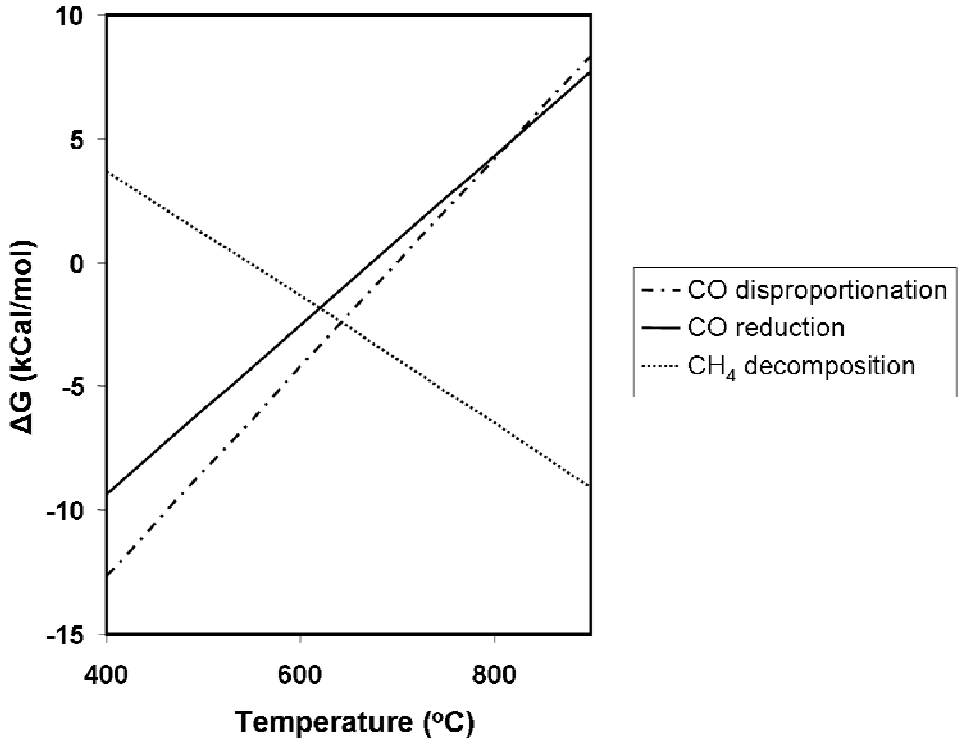

(b)

Fig. 2.3. The change in Gibbs free energy is plotted versus temperature for various reactions.

Taking $\Delta G < 0$ to predict thermodynamic favorability for the forward reaction to occur, the dry reforming reaction is not favored until the temperature reaches 650°C. The water-gas-shift reaction is favored up until 825°C, then the reverse reaction becomes favorable. However, the magnitude of ΔG for the WGS is relatively low, meaning that the presence of both of either the product or reactant species could drive the reaction in either direction.

The CO disproportionation (Boudouard reaction) and CO reduction reactions are favored at temperatures up to 700°C and 675°C, respectively. CH_4 decomposition does not become favorable until temperatures beyond 550°C. In the temperature range from 550°C to 675°C, carbon deposition is favored by each of the CO disproportionation, CO reduction, and CH_4 decomposition reactions. This can be considered the region where severe coking is expected.

Thermodynamic equilibrium calculations were performed with GASEQ to measure the equilibrium mole fraction of solid carbon generated due to each of the carbon deposition reaction, as seen in Fig 2.4. The program GASEQ determines the equilibrium concentrations by minimizing Gibbs free energy. The Gibbs free energy G of the mixture at pressure p is given by:

$$\frac{G}{RT} = \sum_{i=1}^{nSp} \left(\frac{x_i G_i^0}{RT} + x_i \ln \frac{x_i}{\sum x_i} + x_i \ln p \right)$$

where the equilibrium number of moles of species i is x_i (i = 1 to nSp), G_i^0 is the molar free energy at 1 atmosphere of species i, and $\sum x_i$ is the total number of moles in the mixture. At equilibrium G/RT is at a minimum.

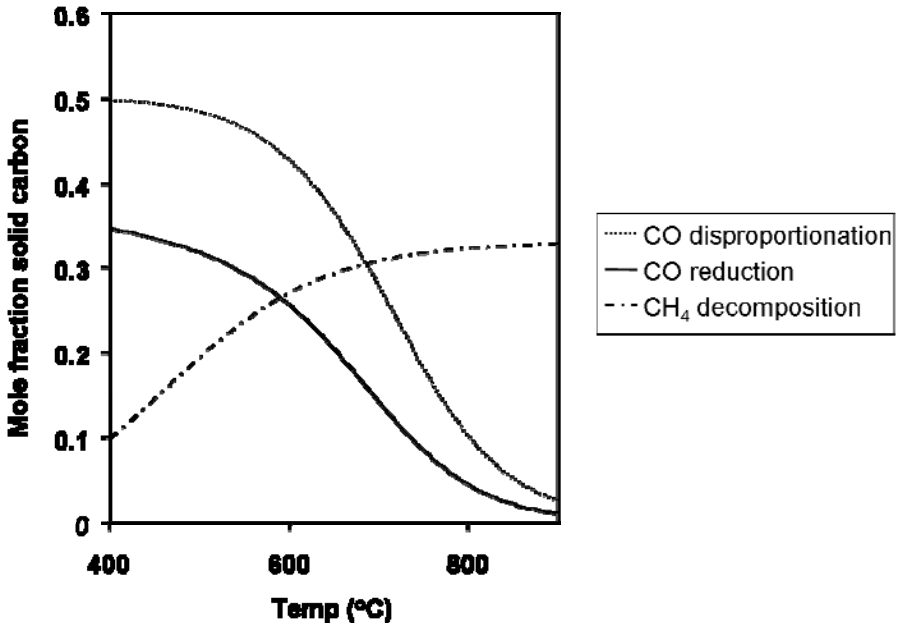

Fig. 2.4. Equilibrium mole fraction of solid carbon formed from various carbon deposition reactions is plotted versus temperature.

As expected, the equilibrium mole fractions of carbon follow the trends predicted by the relative values of the change in Gibbs free energy for the reactions that were discussed previously. At temperatures up to about 600°C, CO disproportionation generates the greatest equilibrium mole fraction of solid carbon, followed by CO reduction and CH_4 decomposition. Then, from about 600°C to 700°C, CO disproportionation generates the greatest equilibrium mole fraction of solid carbon, followed by CH_4 decomposition and CO reduction. Above 700°C, CH_4 decomposition results in the highest mole fraction, followed by CO disproportionation and CO reduction.

To provide a better picture of the expected concentrations of species which result from reforming CH_4 with CO_2, thermodynamic equilibrium calculations were conducted for the dry reforming reaction. Calculations were performed for a temperature range of 400°C to 900°C with an inlet of 0.083 moles CH_4, 0.083 moles CO_2, and 0.834 moles Ar which are the inlet conditions for many of the catalytic reforming studies performed, described in the following sections.

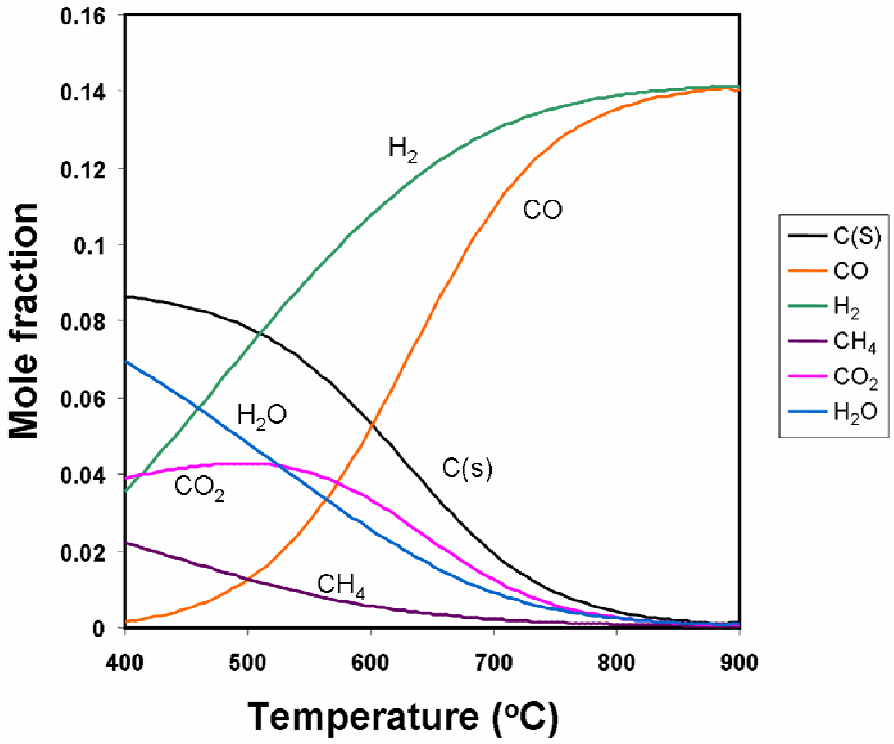

Fig. 2.5. Equilibrium mole fraction is plotted versus temperature.

From these calculations, it is shown that the greatest amounts of solid carbon are expected at low temperatures, with the equilibrium mole fraction decreasing with increasing temperature until about 900°C. While the thermodynamic favorability of the CH_4 decomposition reaction increases with increasing temperature, the reverse of both the CO disproportionation and CO reduction are favored at increasing temperature, which results in less carbon formation at higher temperatures.

In the region where carbon forms, the H_2:CO and CO_2:CH_4 ratios are greater than one. In addition, a high fraction of water is also expected, decreasing with increasing temperature. Each of these results can be attributed to the dominance of the CO disproportionation and reduction

reactions with respect to CH_4 decomposition, resulting in the generation of C, H_2O, and CO_2 while consuming CO.

Calculations for the effects of pressure and the feed ratio of CO_2:CH_4 on equilibrium concentrations and carbon deposition regions have been presented in literature [8]. The reports have shown that increasing the ratio of CO_2:CH_4 decreases the equilibrium mole fraction of solid carbon, while increasing the pressure increases the mole fraction of carbon present. No experimental studies have been found which have explored the effects of increasing pressure on the kinetics.

2.2 Literature review

The first comprehensive dry reforming experiments were conducted by Fischer and Tropsch in 1928 [9]. They studied the reaction over Fe, Co, Ni, Cu, Mo and W supported on clay, silica and $MgCO_3$ or mixed with Al_2O_3. Gas compositions corresponding to thermodynamic calculations were measured and Ni and Co were found to be the preferred catalysts with activity increasing with loading of Al_2O_3.

The first comprehensive kinetic study was conducted by Bodrov et al in 1967, who found that the kinetics for dry reforming over a Ni film matched the kinetic model they had constructed from a similar study of steam reforming [10]. Bodrov proposed the following model to describe the dry reforming reaction in which * denotes an active site on the catalyst surface, → denotes a slow irreversible reaction, and ←→ denotes a quasi-equilibrated reaction:

$$CH_4 + * \rightarrow CH_2* + H_2 \quad (1)$$

$$CO_2 + * \leftrightarrow CO + O* \quad (2)$$

$$O* + H_2 \leftrightarrow H_2O + * \quad (3)$$

$$CH_2* + H_2O \leftrightarrow CO* + 2H_2 \quad (4)$$

$$CO* + \leftrightarrow CO + * \quad (5)$$

In this model, after methane has dissociated to CH_2 and H_2 (1), and after RWGS has produced H_2O (2 and 3), the remaining methane-derived CH_2 species is reformed with H_2O to produce a net result of 2CO and $2H_2$ (4 and 5). If you remove steps 3 and 4, which is the equilibriated RWGS, then you are left with a simple steam reforming mechanism, resulting in a 1:3 product ratio of CO and H_2. Since the RWGS is assumed to be fast relative to the first step of methane activation and decomposition, you can expect the kinetics to be nearly the same for CO_2 reforming as for H_2O reforming of methane. The early proposal of a reaction mechanism by Bodrov formed the initial model from which recent studies have attempted to refine and build upon.

With increasing research, considerable insight has been attained in recent years resulting in proposals of both modified and alternative reaction mechanisms, dependent on the type of catalyst, the carrier, and even the temperature. But before the kinetics of the overall catalytic dry reforming reaction can be understood fully, an understanding of the elementary steps which may or may not be involved in the mechanism is necessary.

In 1972, Jens Rostrup-Nielsen studied the equilibria of the methane decomposition and carbon monoxide decomposition (disproportionation) in the temperature range of 450-750°C on various

Ni catalysts [11]. It was found that the equilibria constants of the CO disproportionation and methane decomposition reactions were influenced by Ni catalysts resulting in higher equilibrium concentrations of CO and CH_4, respectively, than those predicted using graphite equilibria. At lower temperatures, the deviation is more pronounced, becoming less pronounced as temperature increases. The experimental equilibrium correlates with crystallite size of the catalyst; the greatest deviations from the graphite data were observed on catalysts with small Ni crystallites. The deviation from the thermodynamic graphite calculation was explained by a more disordered structure of the carbon (which formed as whiskers, as seen in Fig. 2.6), and by a contribution from the surface energy of the carbon whisker. As the whisker diameter is related to the size of the Nickel crystal, the size of the Ni crystal affects the carbon formation. The deviations were less for the methane decomposition than they were for the CO disproportionation reaction. Chemical composition, such as the use of carriers or promoters, did not appear to have an effect on the observed equilibria data. Further, it was found that sulfur chemisorbed on the Ni surface prevented the carbon deposition reactions.

Fig 2.6. Whisker carbon formed by CH_4 decomposition over Ni catalyst. (Rostrup-Nielsen 1972)

In later publications in the 1980s and 1990s, Rostrup-Nielsen further details his research and insights into the carbon deposition reactions over Ni catalysts [12]. As stated previously, the Boudouard and methane decomposition reactions are catalyzed by Ni, causing carbon to grow as a fibre/whisker. The chemisorption of methane on Ni involves the breaking of a C-H bond, which necessitates that the molecule has sufficient energy to overcome a barrier of about 52 kJ (12.4 kilocalories)/mol. The methane is converted to carbon through stepwise dehydrogenation:

$$CH_4 = CH_3^* \rightarrow CH_2^* \rightarrow CH^* = C^*$$

Adsorbed carbon atoms that don't react away with gaseous molecules dissolve inside the nickel crystal and solve as carbon nucleated from the unexposed backside of the crystal. It was found

that adsorbed oxygen atoms had no effect on the chemisorption of methane, except decreasing the number of available sites.

In the context of steam methane reforming, in which the primary carbon deposition route is methane decomposition, Rostrup-Nielsen describes carbon formation as to be related to one of two different general conditions. One limit which will result in carbon formation is a kinetic allowance in spite of overall thermodynamics. In these conditions, local processes allow methane to decompose into carbon instead of reacting with steam even though thermodynamics predict no carbon formation after equilibrium of the reforming and shift reactions. The other limit in which carbon may form is dictated by thermodynamics; carbon will be formed if the equilibriated gas shows affinity for carbon.

Methane dissociation, carbon dioxide dissociation, and the dry reforming reaction were studied by Erdohelyi et al in 1993 using Rh catalysts on various supports [13]. The dissociation of CH_4 on Rh was seen at 423°K, producing H_2 and small amounts of C_2H_6; the intermediate species is undoubtedly CH_3, which primarily and rapidly decomposes further to surface carbon and hydrogen atoms, as no CH_3 or CH_x species were identified. With regard to the decomposition of CH_4, Al_2O_3 was the best support for Rh, followed by TiO2, MgO, and SiO2. The amounts of C_2H_6 also decreased in this order.

The same study showed that the dissociation of CO_2 was aided by the addition of CH_4; the hydrogen formed in the CH_4 decomposition promotes the dissociation of CO_2. Erdohelyi et al postulated that the dissociation of CH_4 is facilitated by the adsorbed O formed in the decomposition of CO_2, activating the CH_4. This seemingly conflicts with Rostrup-Nielsen's

findings over Ni catalysts that oxygen atoms only affected CH_4 chemisorption and activation by restricting the amount of available sites. Erdohelyi et al also found that the rate of carbon aging from reactive carbidic carbon to amorphous carbon to graphite increases with increasing temperature. But in the dry reforming studies, no deactivation of the Rh catalysts was experienced, meaning that the surface carbon formed reacted away efficiently before stable amorphous or graphitic carbon is formed. In addition, the ratio of $CO:H_2$ was found to be greater than one, indicating the presence of secondary processes.

Rostrup-Nielsen & Hansen expanded upon previous studies of methane decomposition, CO disproportionation, and reforming over Ni to include the use of noble metals as catalysts, publishing a report in 1993 [14]. The equilibrium constants for methane decomposition were found to be even smaller for noble metals than Ni, deviating further from the graphite equilibrium. At 500°C, the highest rate of carbon formation through methane decomposition followed the order Ni >> Rh> Ir,Ru > Pt, Pd, while at 650°C, the order was Ni > Pd, Rh > Ir > Pt > Ru. For the dry reforming studies conducted in the temperature range of 550-600°C, the activity followed the order Ru, Rh > Ir > Ni, Pt, Pd. The dry reforming catalyst activity trend followed a similar trend for steam reforming, but dry reforming had slower rates and less of a pronounced difference between Ni and the noble metals. In addition, there was no significant difference in the activation energies between steam and dry reforming.

In a study conducted by Richardson & Paripatyadar, Rh and Ru were shown to be suitable catalysts for dry reforming, both displaying high activity, and Rh showing no evidence of carbon deposition in the temperature range from 600-800° C [7]. While Ru and Rh had similar activities, Rh showed greater stability. After 8hrs on stream, deactivation was seen at

temperatures of 600 and 700 deg C on both Ru and Rh, with deactivation decreasing with increasing temperature. However, the Rhodium catalyst was not regenerable, so the deactivation on Rh is assumed to have been from a poison in the feed, which desorbs more easily at the higher temperatures. Carbon formation via methane thermal decomposition was not a likely source of decomposition, as the equilibrium constant increases with increasing temperature. Carbon deposition via CO disproportionation would be the likely cause, as its equilibrium constants decrease with increasing temperatures. The higher resistance to deactivation for Rh agrees with other studies which have shown it to be inactive towards the Boudouard reaction, while Ru quickly deactivates.

Significant controversy exists regarding whether or not the support affects the mechanism, activity, and deactivation of Rh based catalysts. While some studies have suggested that activity is greater on unreducible oxides than on reducible oxides, other studies show no influence from support on dry reforming rates. Of great significance in these studies is the effect of dispersion of Rh crystallites from the support, which must be held constant if supports are to be compared.

In 1996, Zhang et al found that the specific activity of Rh catalysts decreases with respect to carrier in the order of yttria-stabilized zirconica (YSZ) > Al_2O_3 > TiO_2 > SiO_2 > La_2O_3 > MgO, while deactivation rates decreased in the order of TiO_2, MgO >> YSZ, Al_2O_3, La_2O_3, SiO_2 [15]. They also found that deactivation decreased with increasing Rh particle size, which conflicts with reports earlier reports of deactivation on Ni catalysts. Further, the study showed that activity increased with dispersion, or with decreasing Rh crystal size. Sigl et al closely examined the role of vanadia promoted SiO_2 on Rh, finding activity to increase by a factor of 15-20 [16].

Ceria is an intriguing promoter or carrier that should be considered for the dry reforming reaction, selectively producing CO and H_2. It has been shown that CeO_2 supported catalysts have high levels of basic sites, which selectively favor the formation of CO over CO_2 in steam methanol reforming [17]. In addition, CeO_2 provides stabilization for the Al_2O_3 carrier against sintering and serves as a good steam reforming catalyst for the reactions of unburned hydrocarbons. However the reducibility of ceria and its ability to store and release oxygen is the most intriguing aspect, possibly resulting in a new and attractive mechanism. Possible advantages include the facilitation of CH_4 dissociation due to the presence of available oxygen, and the conversion of deposited carbon to CO. On $Pt/Ce_xZr_{1-x}O_2$ catalyts, it was found that the conversion of CH_4 and CO_2 was strongly correlated with Ce content in the support and that maximum conversion occurred at the composition that exhibited the maximum reducibility [18].

Recently, Wei and Iglesia conducted studies on Rh/Al_2O_3 and Rh/ZrO_2, measuring forward rates and activation energies for CO_2 and H_2O reforming of methane [19]. Forward methane reaction rates were found to be proportional to CH_4 pressures and were independent of the identity and concentration of co-reactants or products at 600°C. Forward rates were calculated by correcting measured net rates for approach to equilibrium, η:

$$\eta = \frac{[P_{CO}]^2[P_{H2}]^2}{[P_{CH4}][P_{CO2}]} \times \frac{1}{K_{eq}}$$

where K_{eq} is the equilibrium constant at the given temperature and P_i is the prevalent partial pressure of species i. Then the forward rate, r_n, was given in terms of the observed net rate, r_n, as:

$$r_f = \frac{r_n}{1-\eta}.$$

It was found that the concentration of reactant products influenced net rates only by varying the distance from equilibrium for the overall reaction; their effects disappear when these thermodynamic effects are taken into account by converting experimental net rates to forward reaction rates. Forward CO_2 rates also increased linearly with CH_4 partial pressure but were independent of CO_2 partial pressure. A mechanism was proposed:

$$CH_4 + 2* \rightarrow CH_3* + H* \quad (1)$$

$$CH_3* + * \rightarrow CH_2* + H* \quad (2)$$

$$CH_2* + * \rightarrow CH* + H* \quad (3)$$

$$CH* + * \rightarrow C* + H* \quad (4)$$

$$CO_2 + 2* \leftrightarrow CO* + O* \quad (5)$$

$$C* + O* \leftrightarrow CO* + * \quad (6)$$

$$CO* \leftrightarrow CO + * \quad (7)$$

$$H* + H* \leftrightarrow H_2* + * \quad (8)$$

$$H* + O* \leftrightarrow OH* + * \quad (9)$$

$$OH* + H* \leftrightarrow H_2O* + * \quad (10)$$

$$H_2O* \leftrightarrow H_2O + * \quad (11)$$

Further, this study concluded that forward reaction rates were dependent on dispersion, but not on support type.

Most recently, Rh/La_2O_3 catalysts were studied for dry reforming, suggesting a support-dependent mechanism (Munera, 2006 #102). Oxycarbonates were detected via laser Raman spectroscopy, at it was proposed that there are two rate limiting steps, including the decomposition of CH_4 to C and $2H_2$, and the reaction of surface C with oxycarbonates present in the working catalyst. Under this mechanism, after following Wei & Iglesia's method of correction for forward rates, it was found that the forward methane reaction rate had a reaction order of 0.61 with respect to CH_4 and 0.37 with respect to CO_2. The proposed mechanism is shown:

$$CH_4 + * \leftrightarrow CH_4*$$

$$CH_4* \rightarrow C* + 2H_2$$

$$CO_2 + La_2O_3 \leftrightarrow La_2O_2CO_3$$

$$La_2O_2CO_3 + C* \rightarrow La_2O_3 + 2CO + *$$

The following experimental work was conducted to further explore and substantiate different proposals for the kinetics of the dry reforming reaction, a topic of great interest for environmental, social, and economic benefit.

3. EXPERIMENTAL DESIGN

In order to experimentally obtain dry reforming reaction and deactivation kinetics and to conduct preliminary process simulation of the LFG reforming reaction, a plug-flow reactor (PFR) system was designed and fabricated. Steady-state, isothermal experiments were performed over Rh/γ-Al_2O_3 monoliths and Ni based pellet catalysts in the PFR. Thermogravimetric Analysis was performed to determine the amount of carbon deposition on Rh/γ-Al_2O_3 powder.

3.1 Reactor design

Based on literature reports of dry reforming conversions over various catalysts, a differential plug-flow reactor was designed to perform kinetic studies. Dry reforming reaction rates and corresponding catalyst volumes were obtained from literature, and space velocities were calculated to determine the appropriate scaling for reactor components. Space velocity was defined in terms of the total volumetric flowrate Q and the bulk volume of the monolith or pellet catalyst bed V:

$$GHSV = \frac{Q}{V}$$

Starting with a fixed monolith reactor volume of 3.62 cm^3, mass flow controllers were ordered to provide a total flow of 240-960 ml/min, while staying at least 20 % from the maximum or minimum output of the flow controller. This resulted in a GHSV of 4,000-16,000 1/hr, which was calculated to be an appropriate range to conduct kinetic studies for Ni based catalysts. The catalyst volume could then be adjusted to increase or decrease the space velocity if needed.

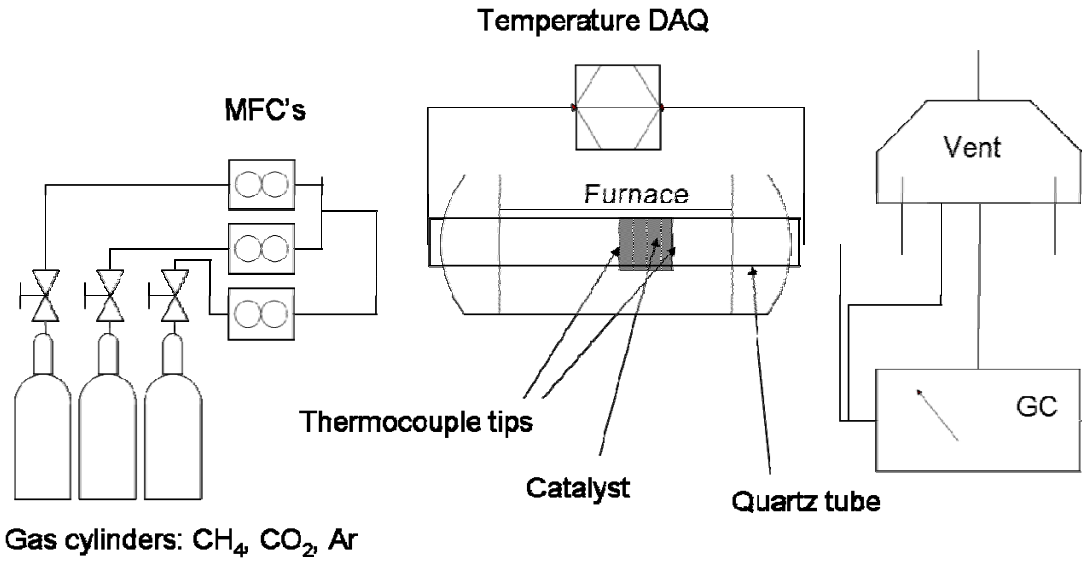

Fig 3.1. Schematic of dry reforming gas delivery, reactor, and analysis.

3.2 Catalysts

Two catalyst formulations were compared in these experiments. The first catalyst tested, from Engelhard Corp., (now BASF Catalysts, LLC) was a Rh/γ-Al_2O_3 monolith. This catalyst was 4 % Rh on Al_2O_3, with a washcoat loading of 1.62g/in^3. The bulk density was measured to be 0.44 g/cm^3. Two sizes of monoliths were used, each from the same batch. The larger catalyst was 0.5" in length with a diameter of 0.75", while the smaller catalyst had a diameter of 0.5". Each monolith had 400 cells per square inch.

The second catalyst was Ni based and was purchased from Süd-Chemie Inc. The product name of the catalyst, with spheres of diameter ranging from 2-4 mm, was G-90 and contained the chemical formulation NiO/CaO/Al_2O_3. In terms of weight percent, the catalyst was 57-87 % aluminum oxide, 10-25 % nickel oxide, and 3-18 % calcium oxide. The bulk density was measured to be 1.04 g/cm^3.

3.3 Reactor Specifications

As the dry reforming reaction is notorious for producing coke when performed over base metals, a quartz tube was chosen to house the catalyst, rather than stainless steel. The straight quartz tubing was purchased at 40" in length, with an OD of 1" and ID of 0.75". While quartz is a poor conductor of heat, which is undesirable for an endothermic reforming reaction, it was important to ensure no reaction occur aside from that which was aided by the catalyst. The quartz tube was connected on both ends with Ultra-Torr fittings to conventional stainless steel tubing and compression fittings, from which gas was transported in polyethylene tubing. Ultra-Torr fittings provide an O-ring seal which can be used against glass, plastic, or metal tubing, and the seal is composed of standard fluorocarbon FKM which is rated to 200°C. The fittings are shown in the figure below:

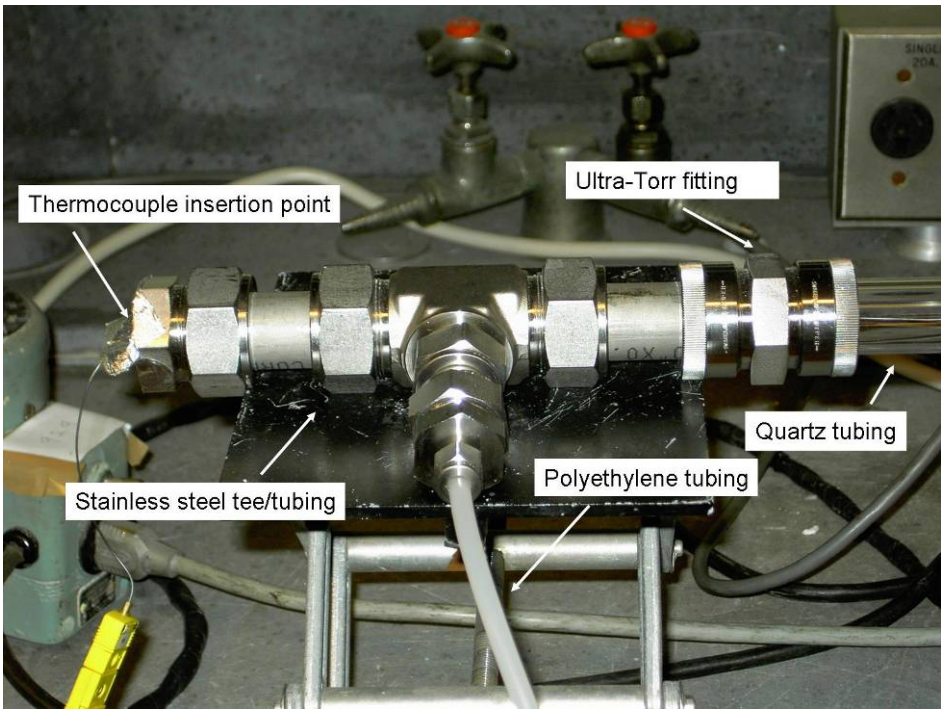

Fig 3.2. Reactor fittings.

The tube was taken to BASF (Engelhard) to be shortened to 32” in length to ease the operation of the reactor for a single researcher. Before cutting the tube, calculations were conducted to ensure that the temperature of the gas leaving the reactor would not be so high as to melt the O-ring seals in the fittings outside.

3.4 Heat supply

A two-stage 750 Watt Multiple Unit ™ furnace was used to provide heat for the reaction. The maximum operating temperature of the furnace is approximately 1000°C, the length is 64cm, and maximum tube diameter is 2”. The temperature of each furnace was controlled via two Variac voltage transformers.

3.4.1 Furnace temperature profile

Before the catalyst could be positioned in the reactor, an experiment was performed to obtain a temperature profile for the furnace, illustrating the heat loss and regions of constant temperature. Each stage of the two-stage furnace was heated to approximately 300°C at its hottest point. A 2.5 cm OD Pyrex tube extended 9.5 cm out from each end of the furnace. Temperature readings were attained by placing a K-type thermocouple inside of a 0.5 cm OD ceramic tube with the thermocouple protruding 6 cm from the end of the tube. The accuracy of the K-type readings were confirmed by comparing temperature readings with an E-type at a couple different positions within the furnace, and the readings were within about 1 degree C.

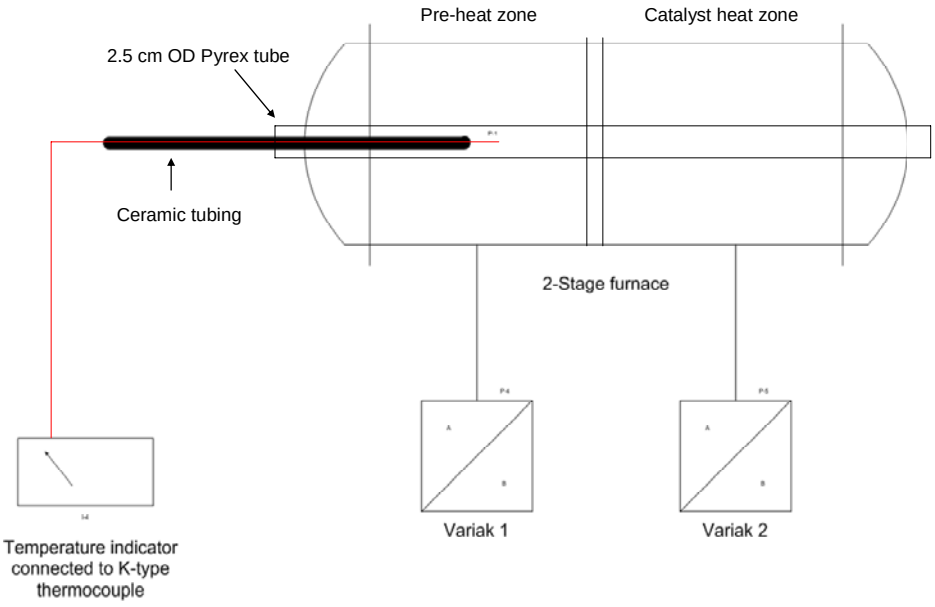

Fig. 3.3. Schematic for temperature profile experiment.

The position of the ceramic tube was fixed radially with insulating material inside of the Pyrex tube such that the tip of the thermocouple would be centered radially in the tubular furnace. It was also essential that the insulating material not pack the ceramic tube into a fixed position too tightly, as it was necessary for the ceramic tube to slide easily in and out of the furnace. The same insulating pattern was repeated at the other end of the Pyrex tube for consistency. Temperature was read in 1 cm increments as the tube and thermocouple proceeded axially in the furnace. As shown in Fig 3.4, the temperature profile for each furnace establishes a uniform temperature over a considerable distance. This profile enabled the catalytic monolith to be placed well within a constant temperature zone, as the length of the monoliths, or pellet reactors, were always shorter than 2 cm.

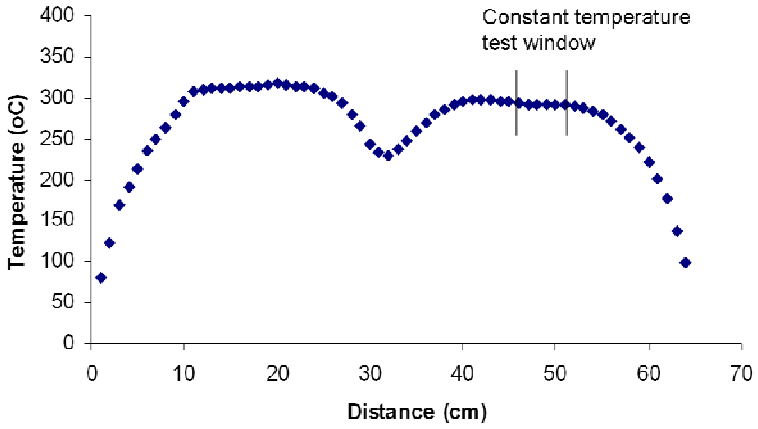

Fig. 3.4. Temperature profile for furnace, showing a test window of about 7 cm.

3.4.2 Heat transfer from furnace to gas

In addition to the temperature profile acquisition, calculations were conducted to ensure that the furnace would provide enough heat to bring the flowing gas up to the reaction temperature before it reached the catalyst bed. The gas temperature $T_m(x)$ at an axial distance x inside the furnace can be calculated from the following equation for forced convection in a tubular pipe with constant heat flux:

$$T_m(x) = T_{m,i} + \frac{q''_s P}{\dot{m} c_p} x$$

where $T_{m,i}$ is the initial gas temperature before entering the furnace, q"$_s$ is the heat flux, P is the perimeter of the cross-sectional area, $\dot{m}$ is the mass flowrate of the gaseous mixture, and c_p is the heat capacity of the gas. It was found that the gaseous mixture would easily reach the desired temperatures at the flowrates desired for the experiments.

3.4.3 Temperature versus flowrate

Experiments were performed to gauge the extent at which the gas temperature inside the furnace changed due to varying flow velocity. It was found that the temperature change was minimal, but with the greatest change at higher temperatures, as expected. However, once a stable,

targeted flow was established, the temperature stabilized and remained unchanged as long as the flow remained constant.

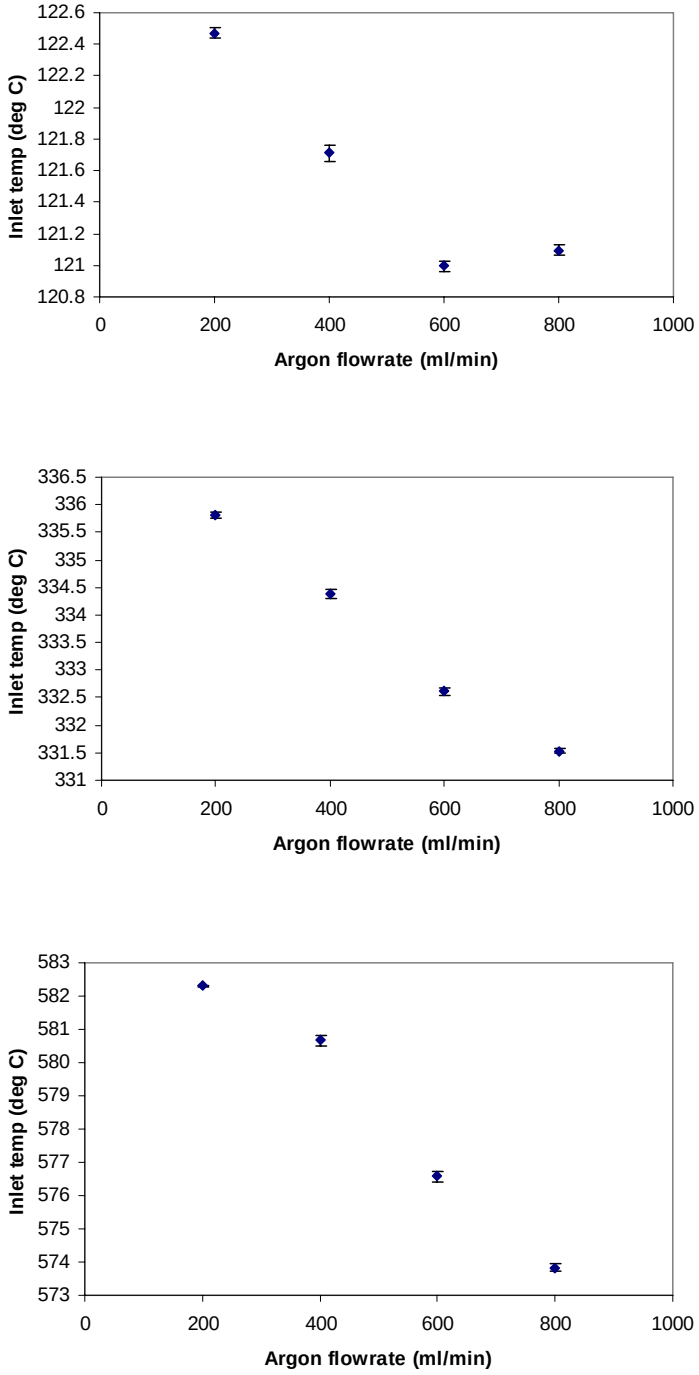

Fig. 3.5. At three different fixed voltage settings, temperature at the inlet of the reactor is shown versus varying flowrate.

3.5 Temperature acquisition

Closed-bead, grounded, K-type thermocouples from Omega were used to acquire temperature at the inlet and outlet of the catalyst bed. Holes were drilled in stainless steel caps at the ends of the tube-fittings 1/32 inch diameter, and the thermocouples were inserted through these holes and fed towards the reactor. The thermocouples were centered radially by placing them in blank ceramic monoliths. Initially, quartz fritted discs were used to fix the radial position of the thermocouples on either end of the reactor, but the ceramic putty which was used to fix the thin thermocouples to the frits proved to form too fragile of a bond. Temperature readings were acquired with an Omega OMB-DAQ-54 data acquisition system.

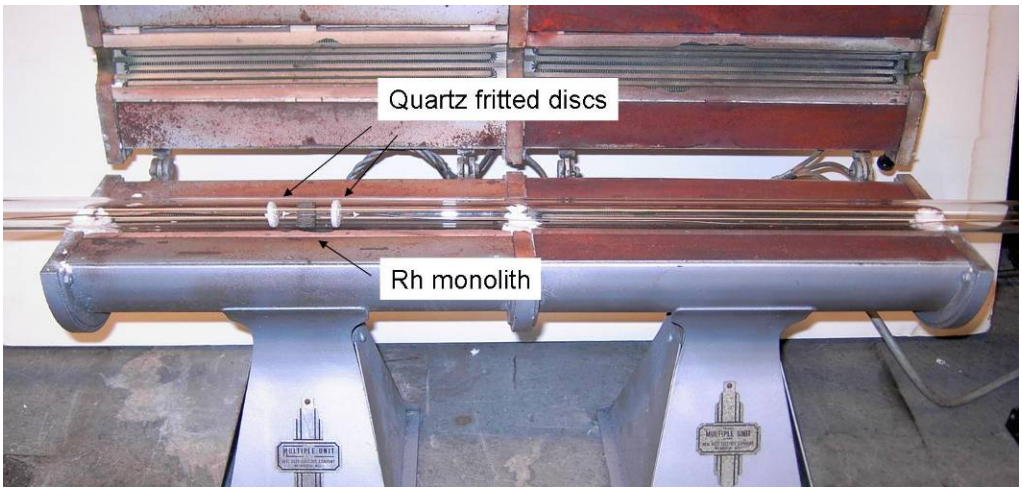

Fig 3.6. Reactor shown with fritted discs holding thermocouples on either end of the monolith.

Fig 3.7. Reactor shown with blank monoliths holding thermocouples on either end of the Rh monolith, wrapped with insulating material.

3.6 Gas feed system

Gas was fed from research grade cylinders of CH_4, CO_2, and Ar into respectively calibrated Aalborg mass flow controllers of model number GFC17.

Fig 3.8. Aalborg GFC17 mass flow controllers.

A bubble meter was used to generate calibrations between actual flowrate and the mass flow controller setting. A sample calibration is provided below.

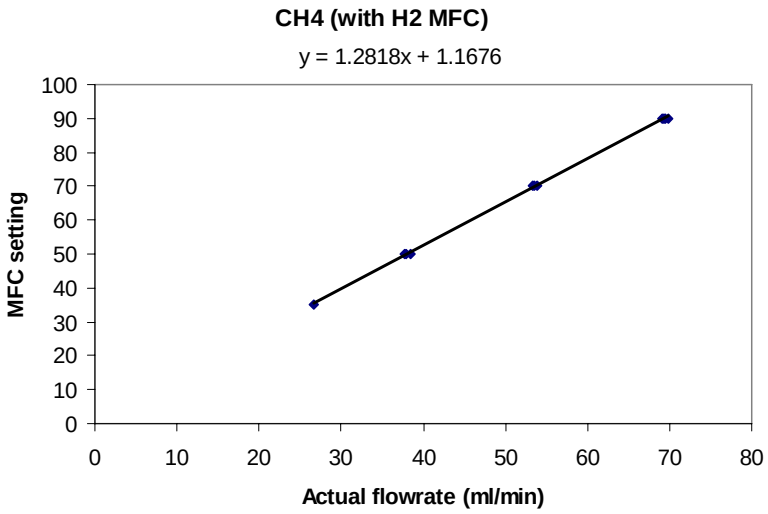

Fig 3.9. Calibration for methane using MFC originally calibrated for hydrogen.

Table 2.1. Items purchased to conduct reactor studies.

Unit	Vendor	Item	Part No. (quantity)
Mass flow control	Aalborg Instruments	Mass flow control (NH3) 500ml/min)	SKUW9459 (1)
		Mass flow control (H2) 100ml/min)	GFCS010031 (1)
		Mass flow control (Ar) 1000ml/min)	GFCS010047 (1)
		Power adapters	PS-GFC-110NA-2 (3)
Reactor tube	Chemglass	Quartz tube (32" length, 1" OD, 3/4" ID)	CGQ-0800-66 (2)
		Quartz fritted disk (3/4", extra coarse)	CGQ-0207-09 (2)
Reactor fittings	Swagelok	Ultra Torr union (1" OD)	SS-16-UT-6 (2)
		Reducing union tee	SS-1610-3-16-12 (2)
		Cap (1" tube OD)	SS-1610-C (2)
		Stainless steel tube (1" length, 3/4" OD)	321-12-X-3 (2)
		Stainless steel tube (1" length, 1" OD)	321-16-X-1 (4)
Themocouples	Omega	K-type (32" length, 1/32" OD)	KMQXL-032G-32 (5)

3.7 Gas analysis

Gas analysis was conducted with an Agilent 3000 Micro GC, pictured below.

Fig. 3.10. Agilent 3000 Micro GC and notebook computer to acquire gas chromatograph data.

A gas chromatograph is a chemical analysis instrument used to separate and analyze chemicals in a complex sample. The MicroGC intakes a gaseous sample and allows it to pass through a narrow tube, known as a column. Different molecules pass through at different rates depending on physical and chemical interactions with the column; the time at which they exit the column is known as the retention time of the molecule. A thermal conductivity detecter identifies and quantifies each molecule as it exits the column. The area under a given peak on the chromatogram correlates with the number of moles of a particular molecule. The rate at which a gas passes through the column increases with increasing temperature. So if greater separation is desired, the temperature should be decreased. However, this results in longer run-times. H_2, CH_4, and CO were identified against an Ar carrier coming out of a mole sieve column, while CO_2 was identified against Ar coming out of the Plot U column. A sample GC calibration is shown below.

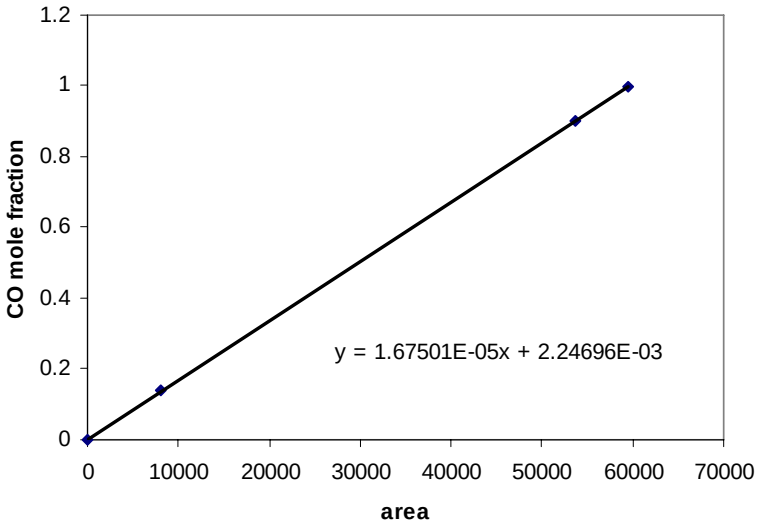

Fig 3.11. Calibration curve for CO is shown.

4. EXPERIMENTAL METHODS

4.1 Steady state reactor studies

Experiments were performed using the catalytic PFR system described previously to explore dry reforming conversion and kinetics at varying temperatures, space velocities, and feed ratios.

4.1.1 Baseline reactor studies

Prior to conducting catalytic dry reforming PFR studies, reactant gas compositions were sent through the PFR at high temperatures and varying space velocities without catalyst to measure baseline conversion. Total gas flows ranged from 420-900 ml/min (furnace residence times of 0.43-0.2 min) with furnace temperatures up to 900°C. Partial pressures of the feed gases, dictated by mass flow controller settings, were 0.083 atm CH_4, 0.083 CO_2, and 0.834 atm Ar. Conversion was measured by taking GC samples of the reactor effluent.

Detailed procedure.

1. The MFCs were plugged in to warm up; the local setpoints on the units were checked to be dialed off.
    a. After 30 minutes of warming up, the valves at the gas cylinders were opened to provide a pressure of 25 psi to the MFCs while leaving the MFC flow dialed off.
2. GC calibration.
    a. The calibration gas cylinder was connected to a spare mass flow controller or rotometer, which sent pure calibration gas with known concentrations of H_2, CO, CH_4, and CO_2 into the GC. Calibrations and retention times were checked.
3. Reactor assembly.

a. Thermocouples were inserted through the tiny holes in the end caps and were fed through until they protruded out of the fittings. Then, the ends of the thermocouples were pushed through the center channel of the blank monoliths so that they protruded 1 cm out from the end.
b. The blank monoliths (containing thermocouples) were placed inside of the quartz tube, and the Ultra-Torr fittings were sealed.
c. The thermocouple/monoliths were pushed into the tube such that one thermocouple tip was located 47 cm downstream into furnace and the other was 48.5cm downstream. Then, they were taped in place on the outside of the cap with alumina tape, sealing the hole in which they were inserted.

4. The mass flow controllers were dialed to the desired setting, and then sent to the GC to check the calibrations. If they did not hit the expected mole fractions from the GC calibrations, the gas flow on the mass flow controllers was adjusted. Typically, an adjustment of more than 5 ml/min was not needed. When the calibrations were in order, the MFCs were turned off.
5. Tube connections were checked from gas cylinders to mass flow controllers (MFCs), from the MFCs to the connecting cross, from the cross to the reactor, and from the reactor to the GC.
6. The argon flow was turned on to 500 ml/min, leaving the CH_4 and CO_2 off.
7. The two-stage furnace was turned on. The Variacs were set very high initially to the ramp up to the desired temperature quickly. Then small adjustments were made to keep the temperature constant at the desired temperature.
8. The CO_2 and the CH_4 MFCs were dialed on.

9. Six GC samples were taken at each condition. Each time the GC took a sample, temperature was recorded.
10. CH_4 and CO_2 MFCs were turned off.
11. Furnace was turned off.
12. When the reactor temperature dropped below 200°C, the Ar MFC was turned off.
13. Gas cylinders were closed.

4.1.2 Stoichiometric reforming studies

Stoichiometric dry reforming studies were performed over Rh/γ-Al_2O_3 monolith and Ni catalysts at space velocities from 7,000-34,000 1/hr and temperatures from 500-590°C. Partial pressures of the feed gases, controlled by mass flow controllers, were 0.083 atm CH_4, 0.083 CO_2, and 0.834 atm Ar. Conversion was measured by taking GC samples of the reactor effluent.

Detailed procedure.

1. Insulation pretreatment.
    a. The insulating material that was to be used to wrap the Rh/γ-Al_2O_3 monolith was placed inside of the empty quartz tube.
    b. The reactor was assembled with thermocouples, but no catalyst, as in the baseline experiments.
    c. 200 ml/min air was flowed through the reactor, while the temperature was increased to 700°C. Air flow was held for 15 minutes at 700°C.
    d. The air flow and furnace was shut off and allowed to cool.
    e. The pre-treated insulation was removed from the empty tube and wrapped around the Rh/γ-Al_2O_3 monolith to the appropriate 0.75” diameter.

2. The MFCs were plugged in to warm up; the local setpoints on the units were checked to be set at zero ml/min of outlet flow.
    a. After 30 minutes of warming up, the valves at the gas cylinders were opened to provide a pressure of about 25 psi to the MFCs while leaving the MFC flow dialed off.
3. GC calibration.
    a. The calibration gas cylinder was connected to a spare mass flow controller or rotometer, which sent pure calibration gas with known concentrations of H_2, CO, CH_4, and CO_2 into the GC. Calibrations and retention times were checked.
4. Reactor assembly.
    a. The catalyst was placed inside of the quartz tube so that the tube was centered in the furnace and the front end of the monolith was 47 cm downstream in the furnace.
    b. Thermocouples were inserted through the tiny holes in the end caps and were fed through until they protruded out of the fittings. Then, the ends of the thermocouples were pushed through the center channel of the blank monoliths so that they protruded 1 cm out from the end.
    c. The blank monoliths (containing thermocouples) were placed inside of the quartz tube, and the Ultra-Torr fittings were sealed.
    d. The thermocouple/monoliths were pushed into the tube such that one thermocouple tip was located 47 cm downstream into furnace and the other was 48.5cm downstream. Then, they were taped in place with alumina tape, sealing the hole in which they were inserted.

5. The mass flow controllers were dialed to the desired setting and the mixture was sent directly to the GC to check the calibrations. If they did not meet the expected mole fractions from the GC calibrations, the gas flow on the mass flow controllers was adjusted. When the calibrations were in order, the MFCs were turned off.
6. Tube connections were checked from gas cylinders to mass flow controllers (MFCs), from the MFCs to the connecting cross, from the cross to the reactor, and from the reactor to the GC.
7. The argon flow was turned on to 500 ml/min, leaving the CH_4 and CO_2 off.
8. The two-stage furnace was turned on. The Variacs were set very high initially to the ramp up to the desired temperature quickly. Then small adjustments were made to keep the temperature constant at the desired temperature.
9. The CO_2 and the CH_4 MFCs were dialed on.
10. Six GC samples were taken at each temperature for a given space velocity. Each time the GC took a sample, temperature was recorded.
11. CH_4 and CO_2 MFCs were turned off.
12. Feed gas was routed to the GC, where the calibrations for the next flow settings were to be checked. When the calibrations were in line, experiments were repeated at the new space velocity, at the same temperature range.
13. When experiments were finished, reactive gases were turned off and the furnace was turned off.
14. When the reactor temperature dropped below 200°C, the Ar MFC was turned off.
15. Gas cylinders were closed.

4.1.3 Varying CO_2

Dry reforming studies were performed over a Rh/γ-Al_2O_3 monolith with CO_2 partial pressures from 0.042-0.25 atm and temperatures from 500-590°C, at space velocities of 15,000 and 34,000 1/hr. The partial pressure of CH_4 was held constant at 0.083, while the partial pressure of Ar was tuned to maintain a constant space velocity. Conversion was measured by taking GC samples of the reactor effluent. The detailed procedure was very similar to that of the stoichiometric reforming procedure.

4.1.4 Varying CH_4

Dry reforming studies were performed over a Rh/γ-Al_2O_3 monolith with CH_4 partial pressures from 0.042-0.25 atm and temperatures from 500-590°C, at space velocities of 15,000 and 34,000 1/hr. The partial pressure of CO_2 was held constant at 0.083, while the partial pressure of Ar was tuned to maintain a constant space velocity. Conversion was measured by taking GC samples of the reactor effluent. The detailed procedure was very similar to that of the stoichiometric reforming procedure.

4.2 Deactivation studies

Experiments were conducted with the PFR, as well as with thermogravimetric analysis, to examine catalyst deactivation. A preliminary TGA-DTA test was also conducted over a spent Rh/γ-Al_2O_3 sample to measure thermal evolution in an oxidizing atmosphere.

4.2.1 On-stream activity

Throughout the Rh/γ-Al_2O_3 monolith PFR studies, initial test conditions were periodically repeated so that changes in activity could be checked.

4.2.2 TGA

Thermogravimetric analysis was also conducted in a TG-DTA/DSC Apparatus STA 409PC/4/H *Luxx* manufactured by Netsch. After a background test was performed a $Rh/\gamma\text{-}Al_2O_3$ powder sample was placed in the TGA and gas flow rates of 10 ml/min CH_4, 10 ml/min CO2, and 100 ml/min Ar were turned on, controlled by Aalborg MFCs. Temperature was ramped up to the desired temperature, where isothermal conditions were maintained for over three hours while mass percent change was recorded.

4.2.3 TGA-DTA

After the TGA study was conducted to measure mass percent change while reforming, simultaneous DTA-TGA in an oxidizing atmosphere was conducted over the spent sample to measure heat of reaction and mass change. Gas flowrates of 10 ml/min O_2 and 100 ml/min Ar were sent into the TGA which held the spent sample, and temperature was ramped up to 800°C. Mass percent change and differential thermal analysis were conducted simultaneously.

5 RESULTS

5.1 Baseline studies.

Experimental measurements of outlet species from the PFR without catalyst showed no measurable conversion up to 900°C, with furnace residence times of 0.43-0.20 minutes (inlet gas composition of 0.083 atm CH_4, 0.083 atm CO_2, 0.834 atm Ar). At 900°C and at the longest residence time, H_2 and CO were detected at ppm level.

5.2 Stoichiometric dry reforming studies.

Experimental measurements of effluent species concentrations from the Rh/γ-Al_2O_3 monolith reactor deviated from thermodynamic equilibrium calculations which included the possibility for solid carbon formation (Fig 5.1a). Concentrations of CO were far beyond that which was predicted resulting in a CO:H_2 ratio greater than unity, and other species showed no correlation to predicted concentrations over the temperature range from 500-590°C. When compared with thermodynamic equilibrium calculations which restrict the possibility of forming solid carbon, however, the experimental data shows strong correlation (Fig 5.1b).

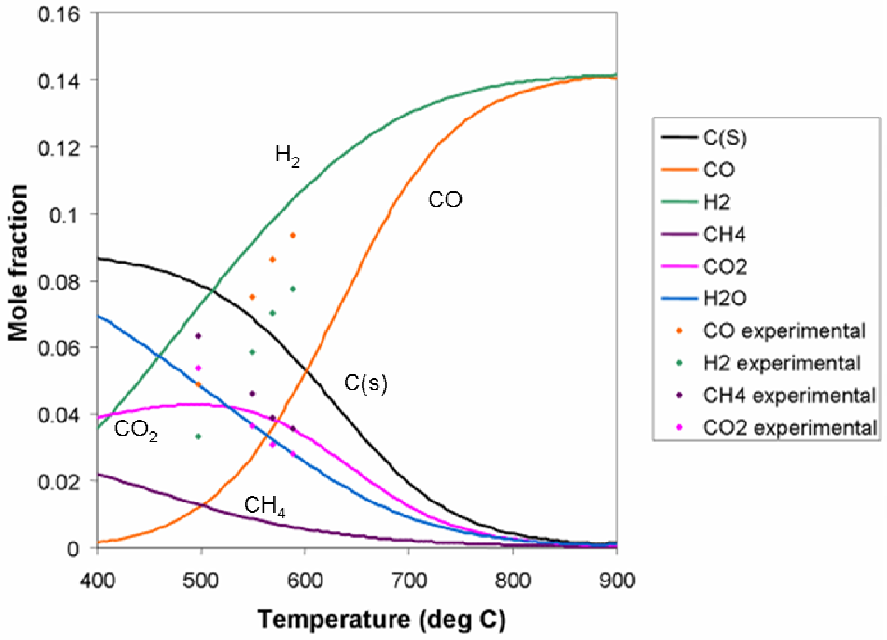

(a)

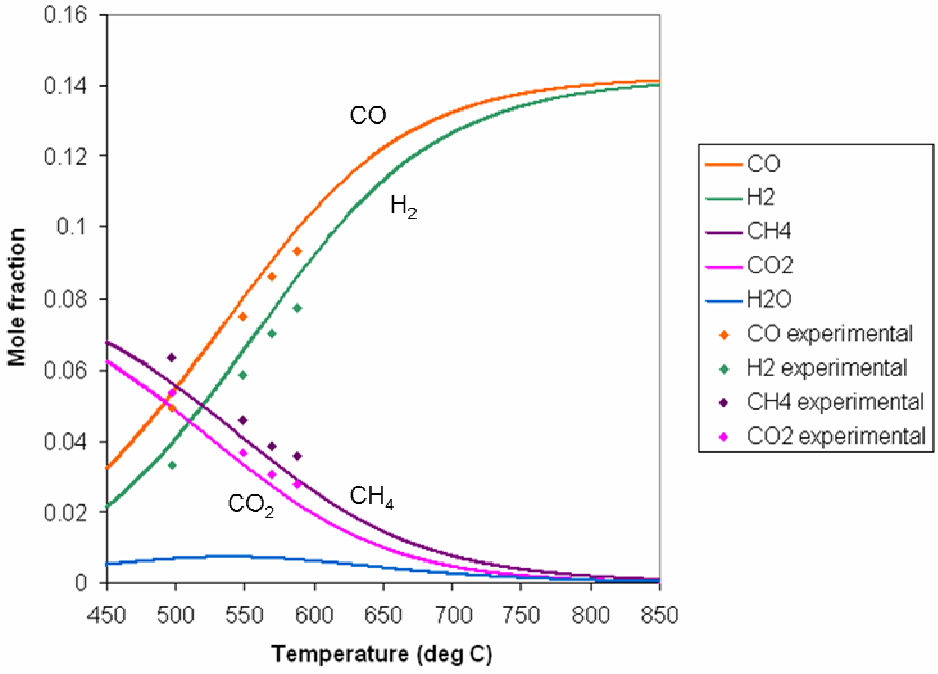

(b)

Fig 5.1. Experimental wet mole fraction with equilibrium calculations at varying temperatures. Equilibrium calculations take into account the possibility of solid carbon formation (a) and withhold the possibility of solid carbon formation (b). Inlet gas composition was 0.083 atm CH_4, 0.083 atm CO_2, 0.834 atm Ar for both experimental and calculated results. Experimental results at 15,000 1/hr GHSV over Rh/γ-Al_2O_3 monolith.

As the space velocity was decreased to 7,000 1/hr, the observed mole fractions approached the thermodynamic equilibrium predictions that precluded the possibility of carbon formation, with closest approach at the highest temperature (Fig 5.2). At 7,000 1/hr and 590°C, equilibrium is achieved ± 5 %, with conversions of nearly 70 % of the reactants. As space velocity is increased by a factor of 5, conversions drop to approximately 20 % at 500°C (60 % of equilibrium). Conversion *x* is calculated as the change in flowrate divided by the initial flowrate:

$$x = \frac{\dot{m}_{io} - \dot{m}_{if}}{\dot{m}_{io}}.$$

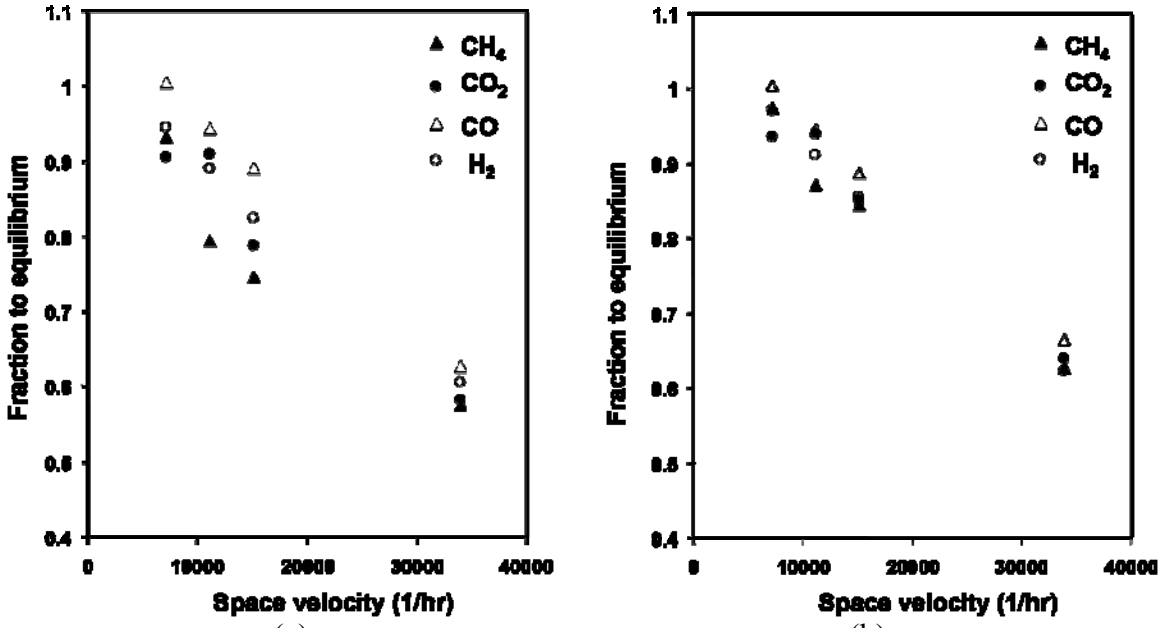

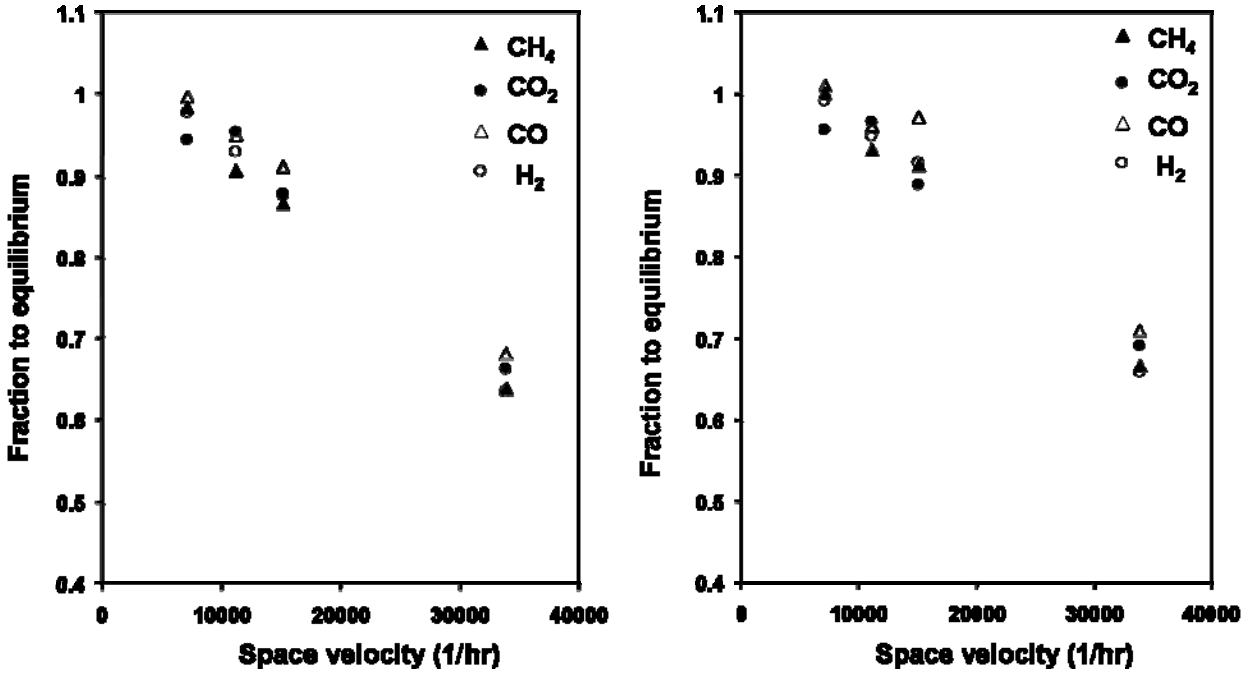

Fig 5.2. Fraction to equilibrium versus GHSV at 500°C (a), 550°C (b) 570°C (c), and 590°C (d). Inlet gas composition was 0.083 atm CH_4, 0.083 atm CO_2, 0.834 atm Ar.

Data reproducibility

As each experimental condition was repeated six times to produce a data point, a range was produced; the mean average was taken, along with x and y error bars representing maximum and minimum temperatures and mole fractions. A representative illustration of the typical range throughout PFR investigations is seen in Fig 5.3. As indicated by the error bars, the range from minimum to maximum is very tight. While there was little deviation in the GC measurements or between the mean temperatures, a gradient of up to 40°C was measured between the inlet and outlet of the reactor, resultant of the strong endothermicity of the reactions occurring.

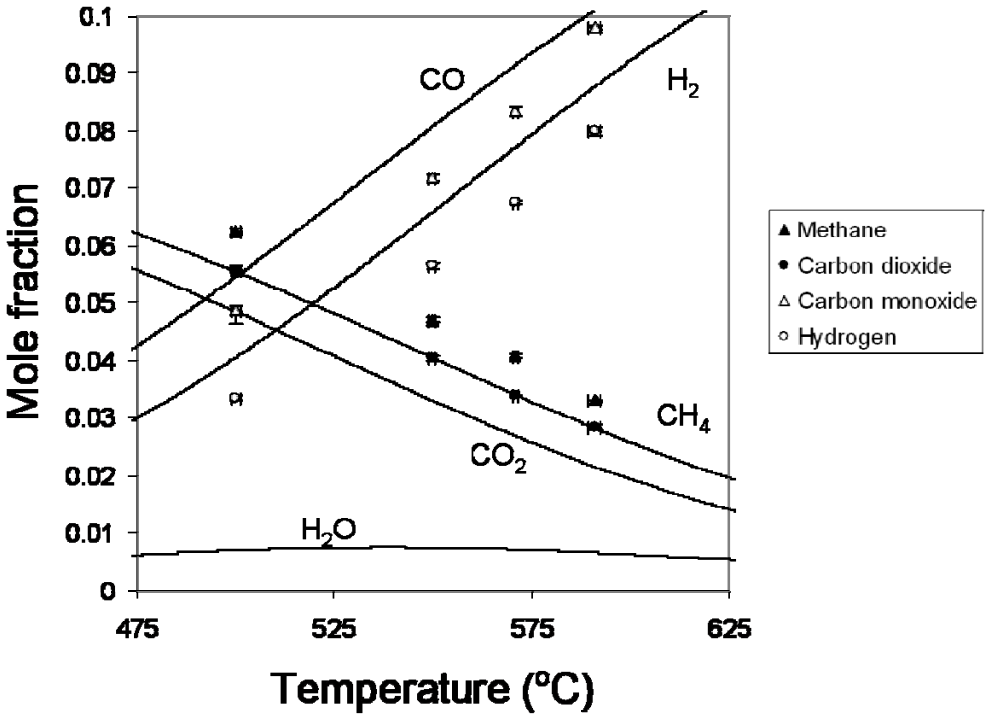

Fig 5.3. Wet mole fraction versus temperature for inlet gas composition of 0.083 atm CH_4, 0.083 atm CO_2, 0.834 atm Ar and GHSV of 15,000 1/hr. Error bars indicate maximum and minimum temperatures and mole fractions in a dataset of six repetitions.

Net reaction rates were calculated for CH_4 and CO_2 in terms of rate of disappearance, and for H_2 and CO in terms of rate of appearance. First, measured inlet and outlet mole fractions, X_{io} and Xi_f, were converted to inlet and outlet mass fractions Yi_o and Yi_f

$$Y_i = X_i \frac{MW_i}{MW_{mix}}$$

where MW_i is the molecular weight of the species and MW_{mix} is the calculated molecular weight of the mix, with Ar composing the balance of the measured species and neglecting other unmeasured species. Reaction rate r_i was then calculated as

$$r_i = (Yi_f - Yi_o)\frac{\dot{m}_{tot}}{MW_i gRh}$$

where $\dot{m}$ is the mass flowrate, and g-Rh is the amount of Rhodium deposited on the catalyst in grams. The value of g-Rh is calculated on the basis that the entire catalyst (ceramic monolith and washcoat) was measured to have a bulk density of 1.99 g-cat/in^3, and the Rh/Al_2O_3 washcoat is loaded at 1.62 g-Rh/Al_2O_3/in^3 with 4 % Rh. Reaction rates versus space velocities are shown below in Fig 5.4, at temperatures from 500-590°C, and reaction rate is plotted versus temperature in Fig 5.5. As seen in Fig 5.4, reaction rates are increasing with space velocity, even at the lowest residence time. This indicates that the reaction is likely to be limited by bulk mass transfer. For this reason, this study will consider only net rates of reactions without a correction for approach to equilibrium, as suggested by Wei & Iglesia to rigorously obtain forward rates. Reaction rates with respect to increasing space velocity or temperature decrease in the order of $CO > H_2 > CO_2 > CH_4$.

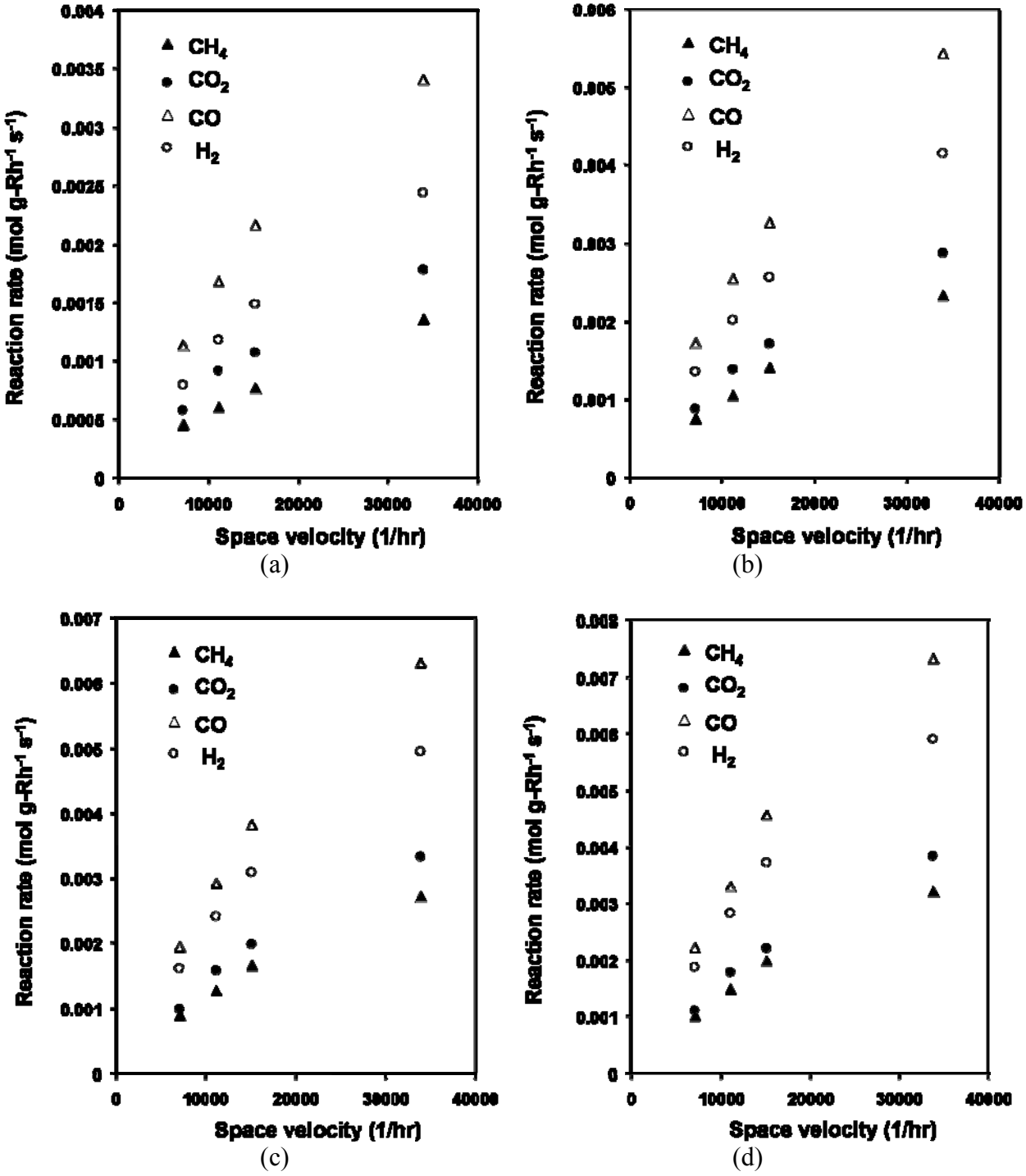

Fig 5.4. Reaction rate versus GHSV at 500°C (a), 550°C (b) 570°C (c), and 590°C (d). Inlet gas composition was 0.083 atm CH_4, 0.083 atm CO_2, 0.834 atm Ar.

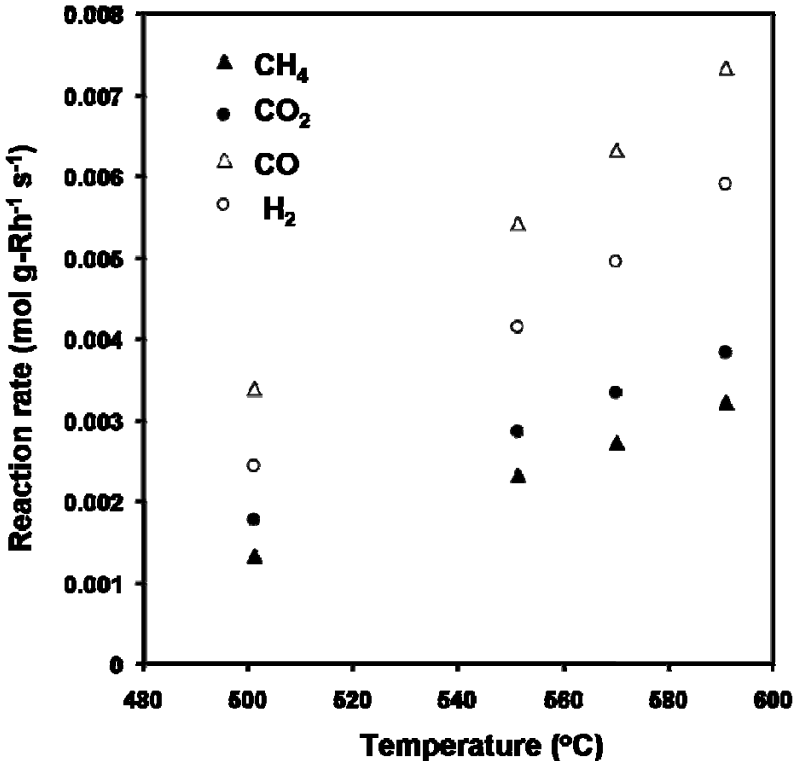

Fig 5.5. Reaction rate versus temperature at 34,000 1/hr. Inlet gas composition was 0.083 atm CH_4, 0.083 atm CO_2, 0.834 atm Ar.

Arrhenius plots of reaction rate and turnover frequency (TOF) versus 1000/T are shown in Figures 5.6 and 5.7, allowing simple calculation of activation energies, E_a, and rate constants, K, from the slope and intercept, respectively. An expression for the forward rate of reaction (approximated here as experimental net rate) can be generated as

$$r_i = KP_{CH4}{}^{\alpha}P_{CO2}{}^{\beta}.$$

$$r_i = k_0\exp(-Ea/RT)P_{CH4}{}^{\alpha}P_{CO2}{}^{\beta}.$$

If the partial pressures of CH_4 and CO_2 are kept constant then you can set

$$A = k_0P_{CH4}{}^{\alpha}P_{CO2}{}^{\beta}.$$

Then, the expression for the rate of reaction is simplified and the natural logarithm is taken to generate a convenient plot from which to gather the activation energies and rate constants.

$$r_i = A \exp(-Ea/RT)$$

$$\ln r_i = \ln A - (Ea/RT)$$

Results of calculations of activation energies and constants are seen in Table 5.1.

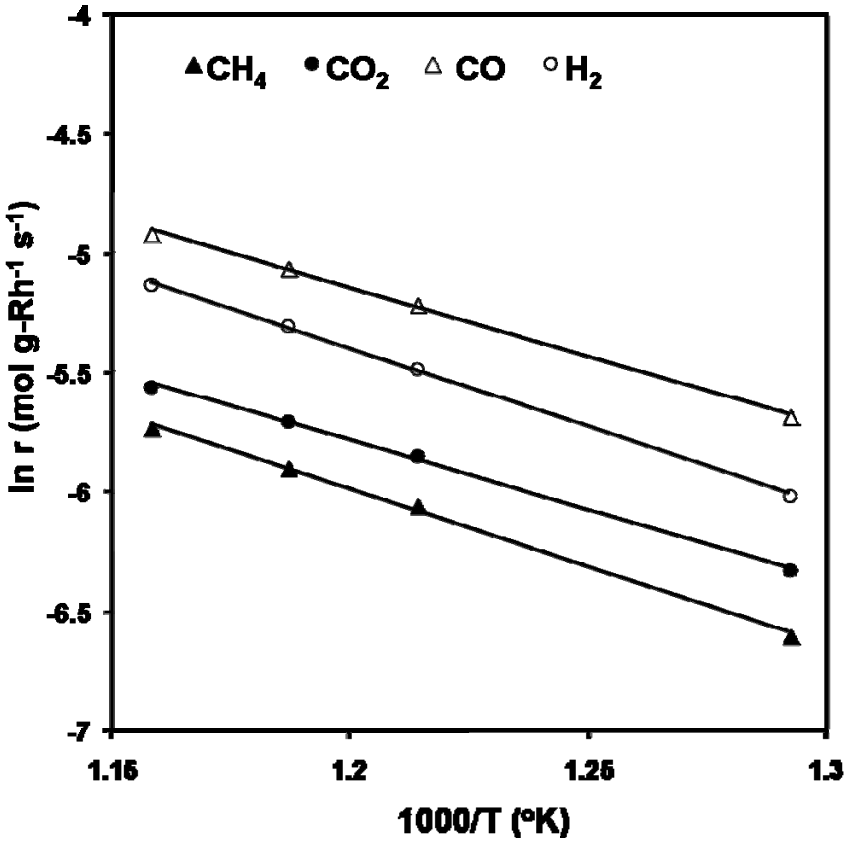

Fig 5.6. Natural logarithm of reaction rate versus 1000/temperature (°K) at 34,000 1/hr. Inlet gas composition was 0.083 atm CH_4, 0.083 atm CO_2, 0.834 atm Ar.

Turnover frequencies (molecules surface-atom-Rh^{-1} s^{-1}) were calculated based on a fresh catalyst dispersion *D* of 0.5 (surface-atoms-Rh/total-atoms-Rh), which is assumed to be stable throughout the experimental processes. TOF can be derived from reaction rate *r* from simple unit analysis:

$$r\left(\frac{moles_i}{gRh\,\sec}\right)\times\left(\frac{6.02E23 molecules_i}{mol_i}\right)\times MW_{Rh}\left(\frac{102.9 gRh}{molRh}\right)\times\left(\frac{mol_{Rh}}{6.02E23 atoms_{Rh}}\right)\times\frac{1}{D}\left(\frac{atomsRh}{surf.atomRh}\right)=TOF\left(\frac{molcule_i}{surf.atomRh\,\sec}\right)$$

This results in a simple definition of TOF in terms of r, MW_{Rh}, and D:

$$TOF = \frac{r \times MW_{Rh}}{D}.$$

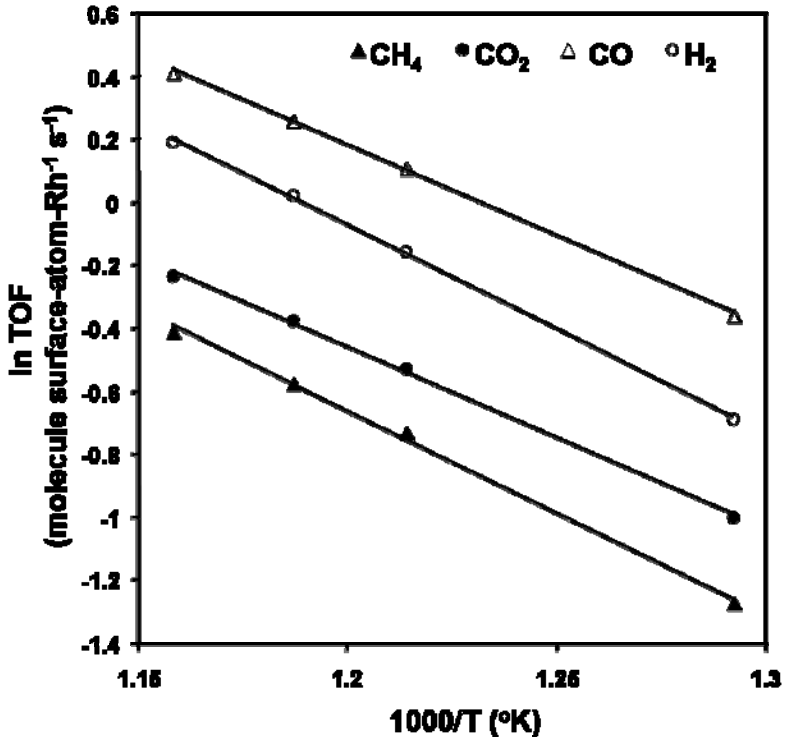

Fig 5.7. Natural logarithm of TOF versus 1000/temperature (°K) at 34,000 1/hr. Inlet gas composition was 0.083 atm CH_4, 0.083 atm CO_2, 0.834 atm Ar.

5.3 Varying inlet CO_2 partial pressure

Maintaining a constant inlet CH_4 partial pressure, outlet wet mole fractions are shown as a function of varying inlet CO_2 partial pressure for temperatures from 500-590°C in Fig 5.8. As CO_2 partial pressure increases from the limiting reactant to stoichiometric reforming ratio, the greatest changes in mole fractions are seen; CO and H_2 mole fraction increase, while CH_4 decreases. At each temperature, as the ratio of CO_2:CH_4 increases beyond unity, the mole fraction of CO increases while H_2 decreases and CH_4 appears to decrease slightly.

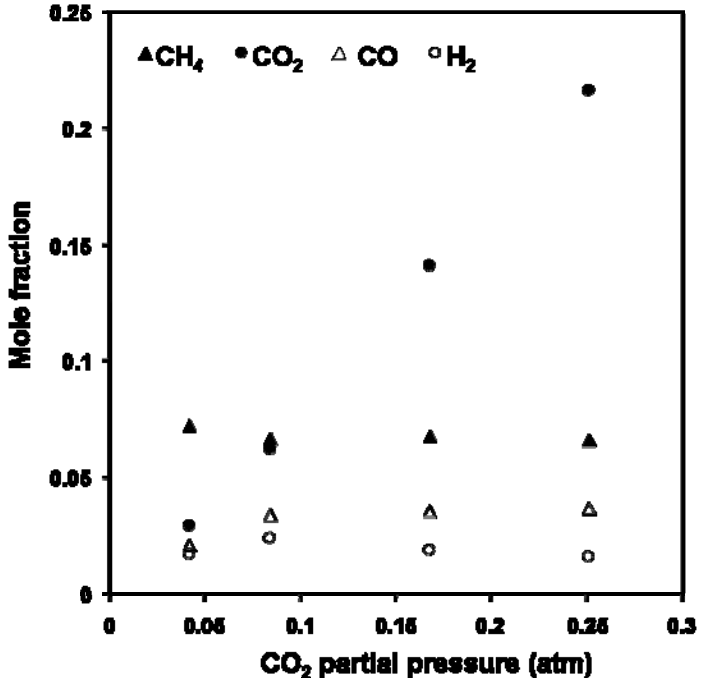
CH4
CO2
CO
H2
Mole fraction
0.25
0.2
0.15
0.1
0.05
0
0
0.05
0.1
0.15
0.2
0.25
0.3
CO2 partial pressure (atm)

(a)

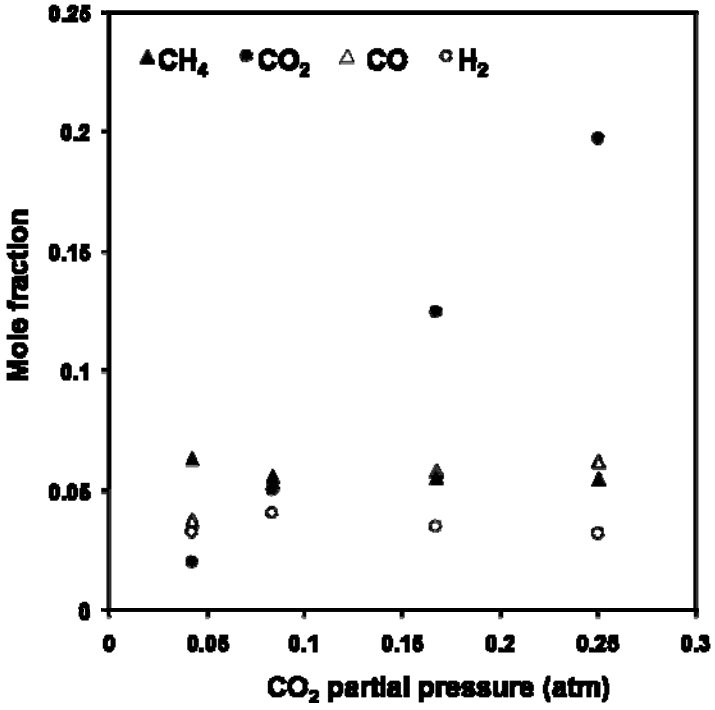
CH4
CO2
CO
H2
Mole fraction
0.25
0.2
0.15
0.1
0.05
0
0
0.05
0.1
0.15
0.2
0.25
0.3
CO2 partial pressure (atm)

(b)

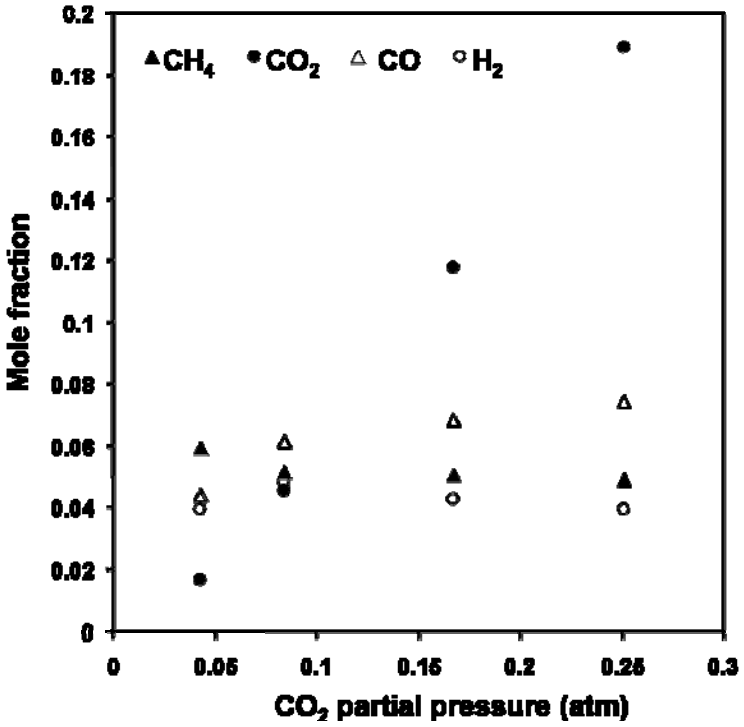

(c)

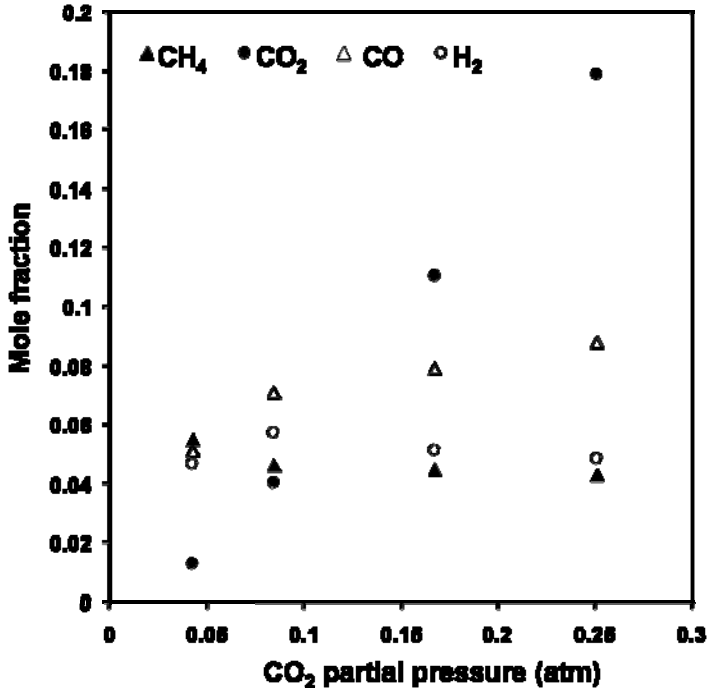

(d)

Fig 5.8. Mole fraction versus CO_2 partial pressure at 34,000 1/hr and 500°C (a), 550°C (b), 570°C (c) and 590°C. Inlet partial pressure of CH_4 fixed at 0.083 atm.

In Figure 5.9, mole fractions are plotted versus temperature for various ratios of CO_2:CH_4 at GHSV of 15,000 1/hr, along with calculated equilibrium mole fractions. At CO_2:CH_4 less than unity, the approach to equilibrium is closest, increasing with temperature. Significant equilibrium mole fractions of water are also calculated, increasing with CO_2:CH_4 and temperature, and surpassing the equilibrium CH_4 mole fraction at 550°C and CO_2:CH_4 of 3.

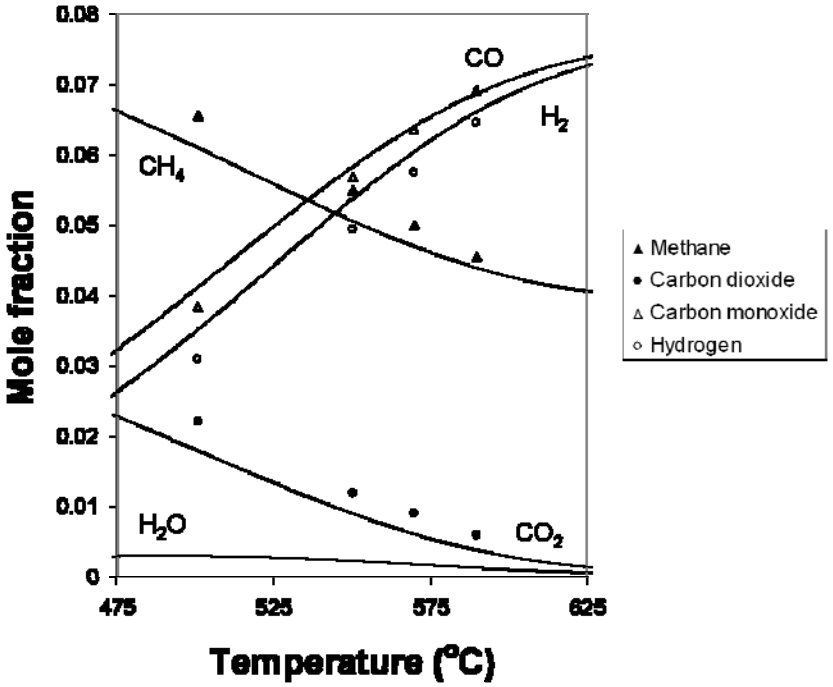

(a)

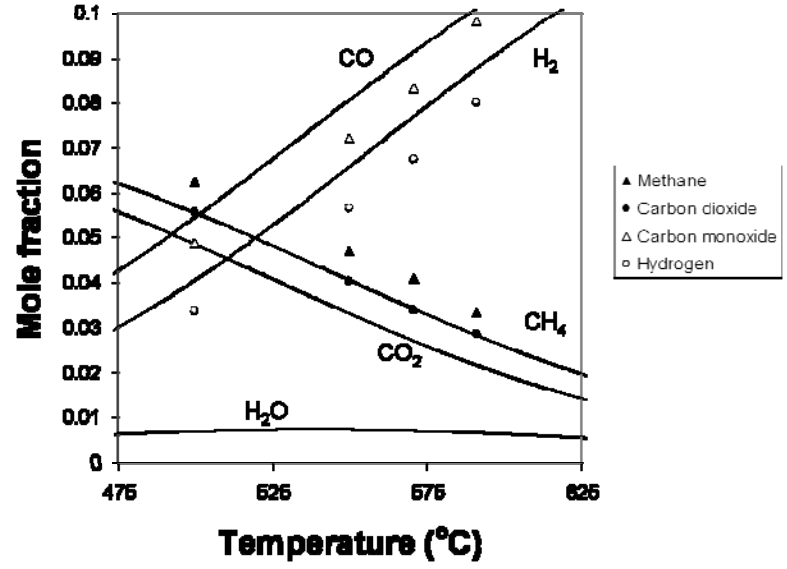
0.1
0.09
0.08
0.07
0.06
0.05
0.04
0.03
0.02
0.01
0
Mole fraction
CO
H2
CH4
CO2
H2O
475
525
575
625
Temperature (°C)
Methane
Carbon dioxide
Carbon monoxide
Hydrogen

(b)

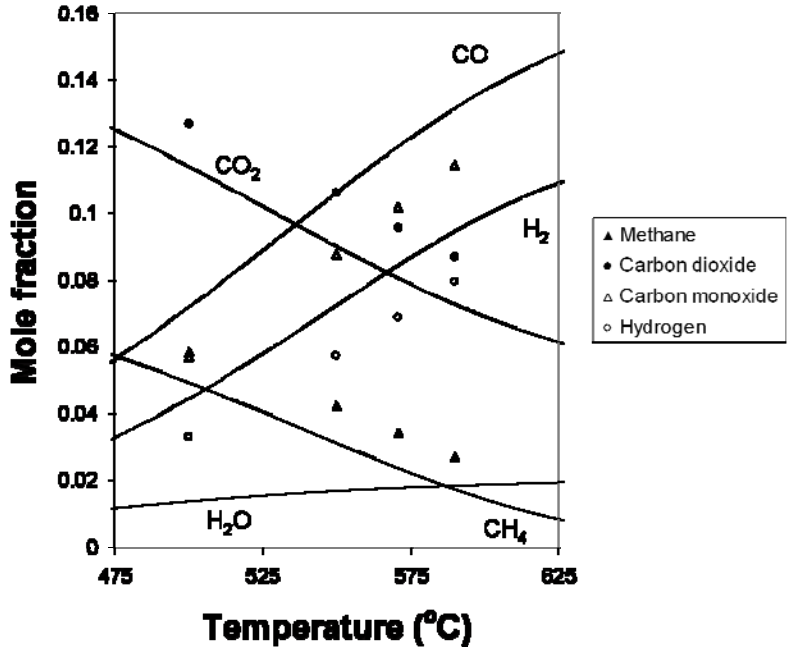
0.16
0.14
0.12
0.1
0.08
0.06
0.04
0.02
0
Mole fraction
CO
CO2
H2
H2O
CH4
475
525
575
625
Temperature (°C)
Methane
Carbon dioxide
Carbon monoxide
Hydrogen

(c)

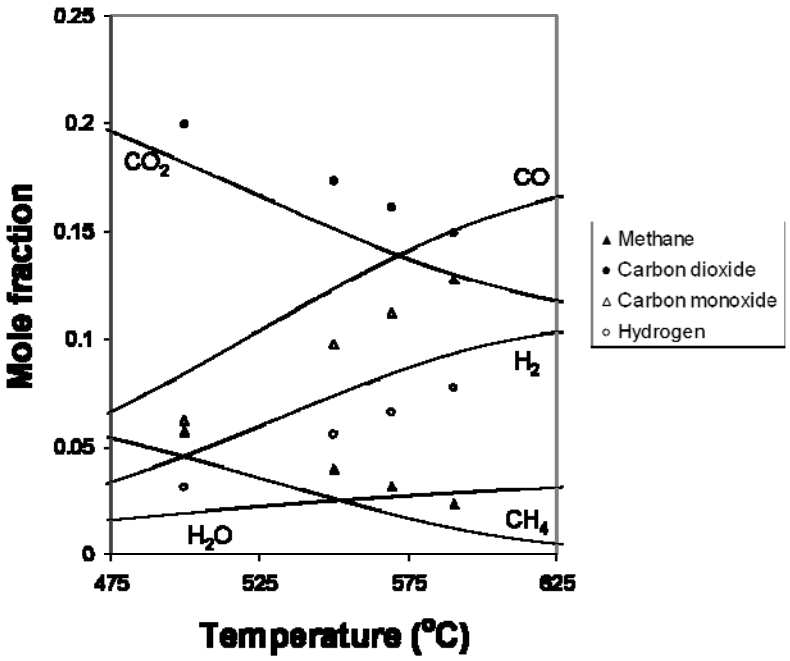

(d)

Fig 5.9. Mole fraction versus temperature at 15,000 1/hr and 0.083 atm CH_4, 0.042 CO_2, 0.875 Ar (a); 0.083 CH_4, 0.083 CO_2, 0.834 Ar (b); 0.083 CH_4, 0.17 CO2, 0.75 Ar (c); and 0.083 CH_4, 0.25 CO_2, 0.667 Ar (d). Solid lines represent equilibrium calculations.

Turnover rates and reaction rates were calculated and plotted versus CO_2 partial pressure in Figs 5.10 and 5.11. All rates increase markedly when CO_2:CH_4 increases from 0.5 to 1. After unity, The CO_2 rate increases the fastest with increasing inlet CO_2 partial pressure, followed by CO and CH_4. The H_2 rates decrease with increasing CO_2:CH_4 beyond unity. All rates increase with temperature.

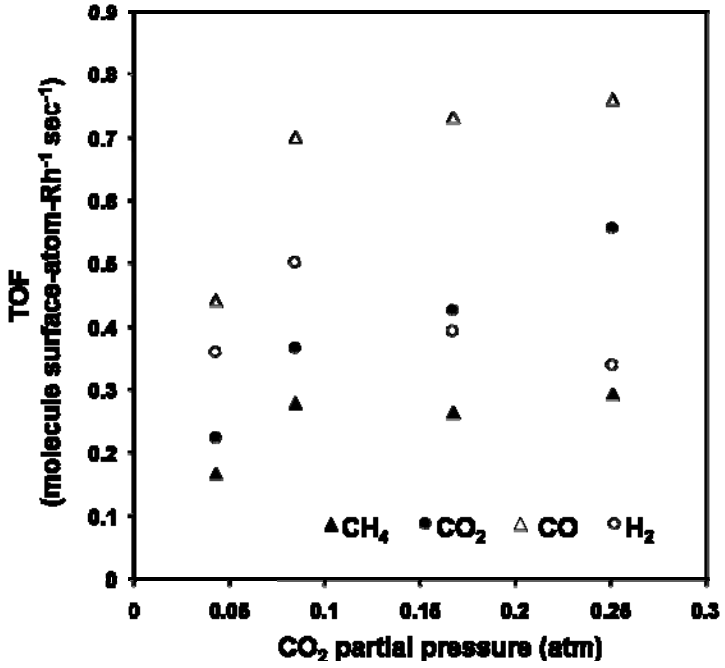
TOF
(molecule surface-atom-Rh^{-1} sec^{-1})
0.9
0.8
0.7
0.6
0.5
0.4
0.3
0.2
0.1
0
0
0.05
0.1
0.15
0.2
0.25
0.3
CO_2 partial pressure (atm)
CH_4
CO_2
CO
H_2

(a)

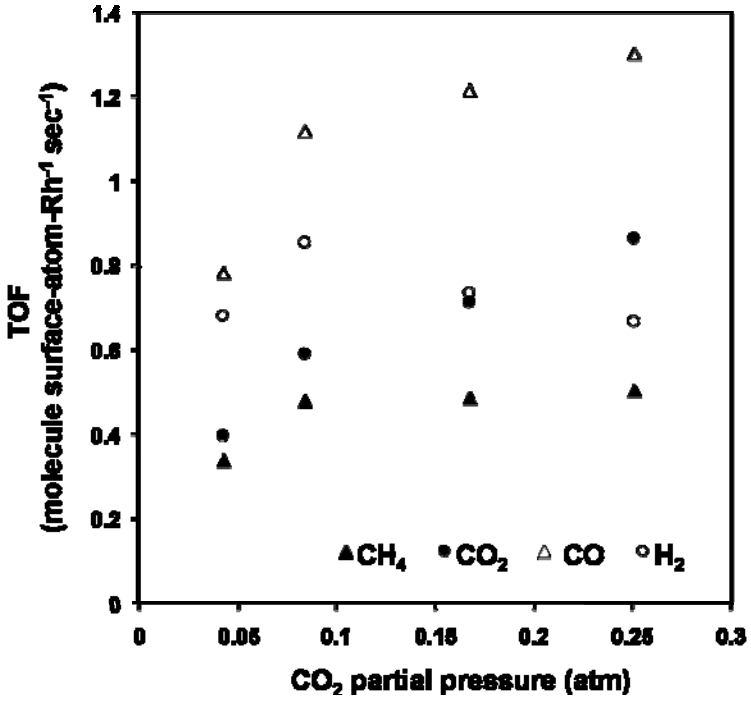
TOF
(molecule surface-atom-Rh^{-1} sec^{-1})
1.4
1.2
1
0.8
0.6
0.4
0.2
0
0
0.05
0.1
0.15
0.2
0.25
0.3
CO_2 partial pressure (atm)
CH_4
CO_2
CO
H_2

(b)

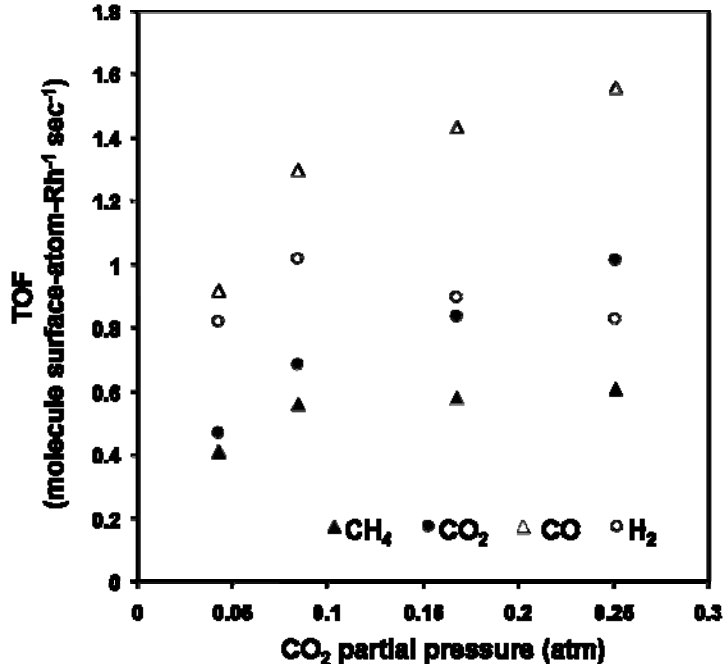

(c)

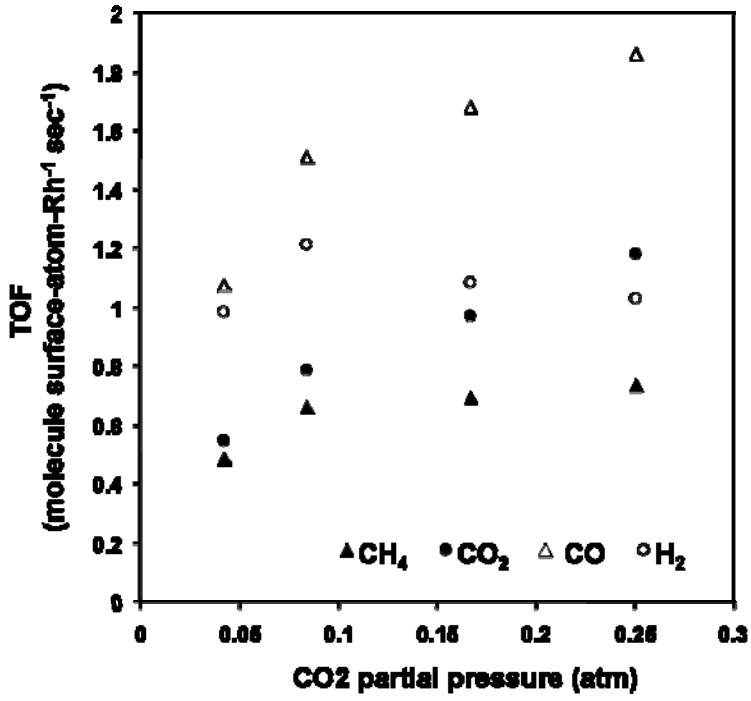

(d)

Fig 5.10. TOF versus CO_2 partial pressure at 34,000 1/hr and 500°C (a), 550°C (b), 570°C (c) and 590°C. Inlet partial pressure of CH4 fixed at 0.083 atm.

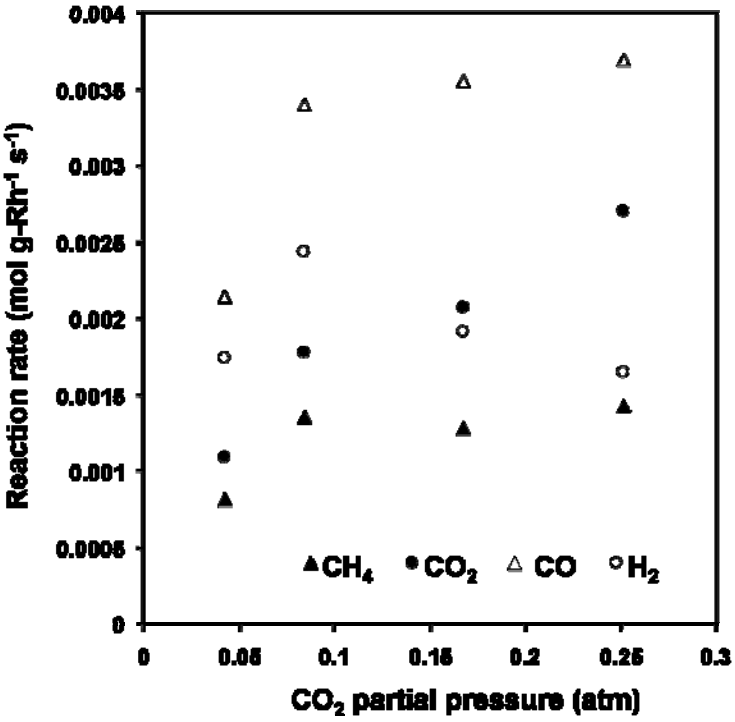
Reaction rate (mol g-Rh^{-1} s^{-1})
0.004
0.0035
0.003
0.0025
0.002
0.0015
0.001
0.0005
0
0
0.05
0.1
0.15
0.2
0.25
0.3
CO_2 partial pressure (atm)
CH_4
CO_2
CO
H_2

(a)

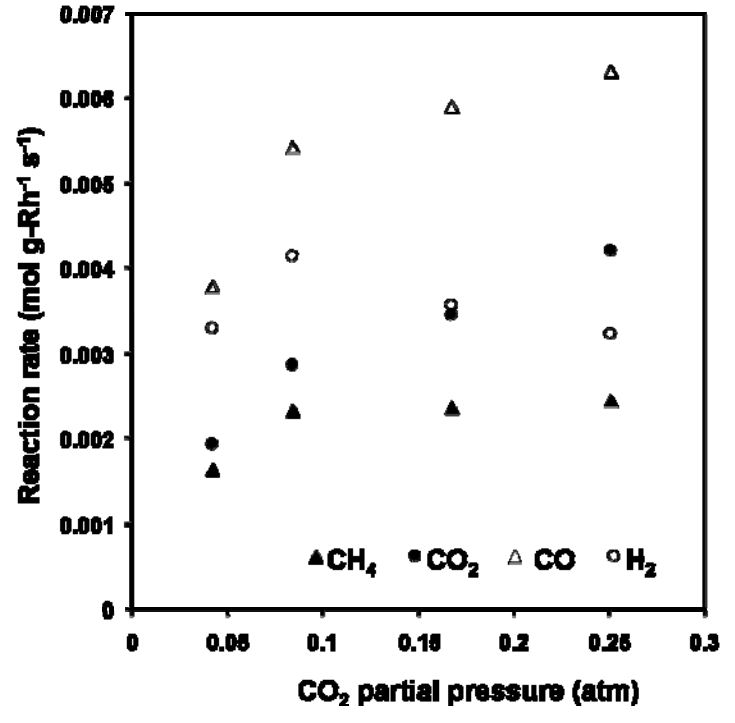
Reaction rate (mol g-Rh^{-1} s^{-1})
0.007
0.006
0.005
0.004
0.003
0.002
0.001
0
0
0.05
0.1
0.15
0.2
0.25
0.3
CO_2 partial pressure (atm)
CH_4
CO_2
CO
H_2

(b)

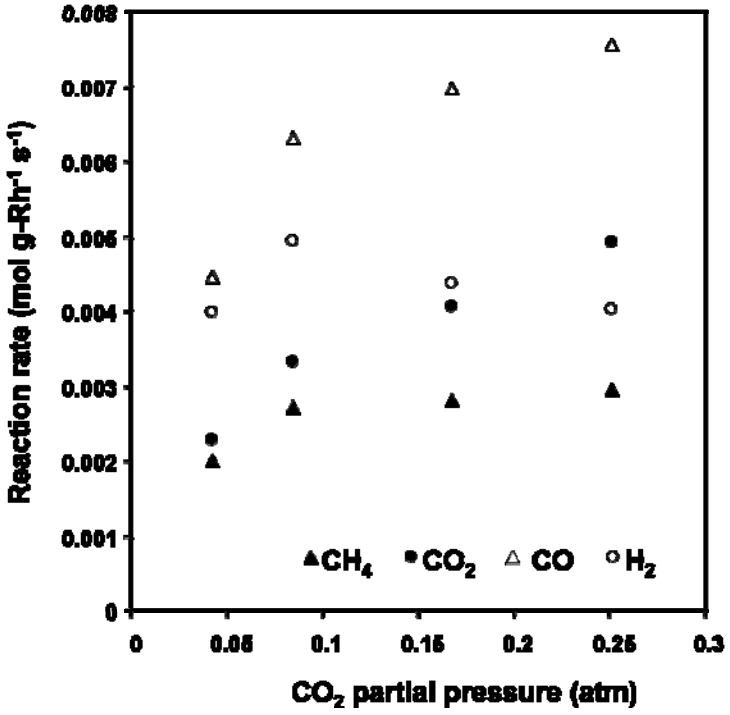

(c)

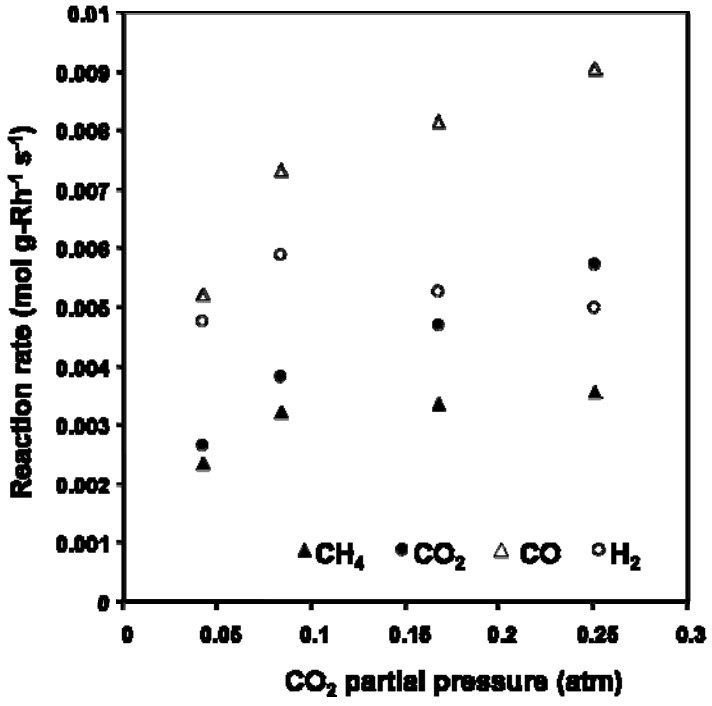

(d)

Fig 5.11. Reaction rate versus CO_2 partial pressure at 34,000 1/hr and 500°C (a), 550°C (b), 570°C (c) and 590°C. Inlet partial pressure of CH_4 fixed at 0.083 atm.

The natural log of reaction rates were plotted versus the natural log of inlet CO_2 partial pressures to obtain reaction order with respect to CO_2. Beginning with the forward rate expression

$$r_i = k_0 \exp(-Ea/RT) P_{CH4}^{\alpha} P_{CO2}^{\beta},$$

and taking temperature and CH_4 partial pressure to be constant, setting

$$B = k_0 \exp(-Ea/RT) P_{CH4}^{\alpha}$$

then, the expression for the rate becomes

$$r_i = B P_{CO2}^{\beta}.$$

Taking the natural logarithm produces a convenient form of equation to plot in which the slope yields the reaction order, β:

$$\ln r_i = \ln(B P_{CO2}^{\beta})$$

$$\ln r_i = \ln B + \beta \ln(P_{CO2})$$

Trendlines were fit to the log-log graphs, and reaction orders are reported in Table 5.2.

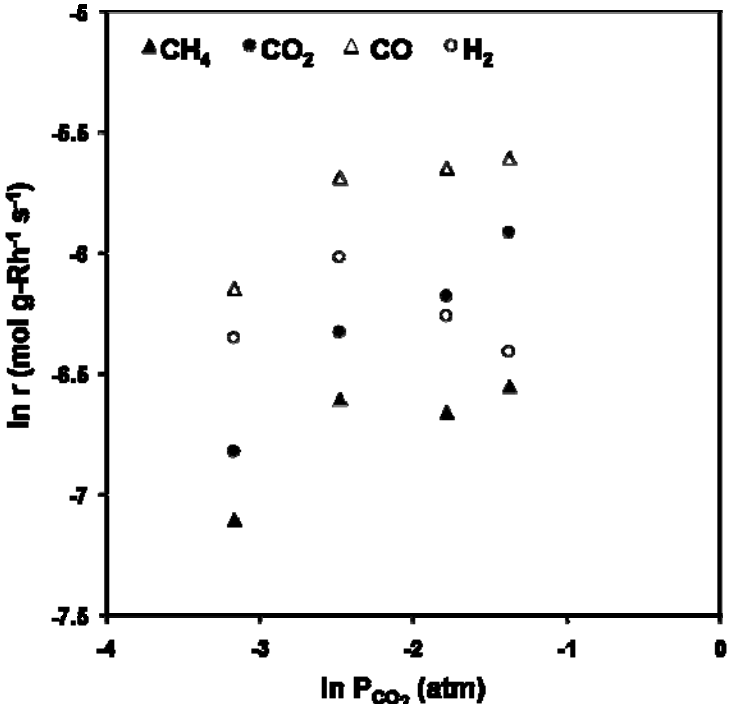

(a)

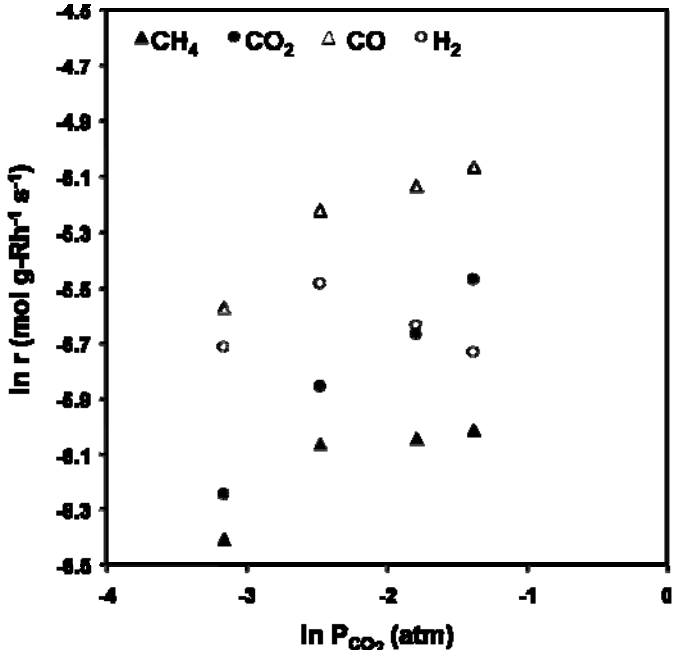
▲CH4 ●CO2 △ CO ○H2
ln r (mol g-Rh-1 s-1)
-4.5
-4.7
-4.9
-5.1
-5.3
-5.5
-5.7
-5.9
-6.1
-6.3
-6.5
-4
-3
-2
-1
0
ln PCO2 (atm)

(b)

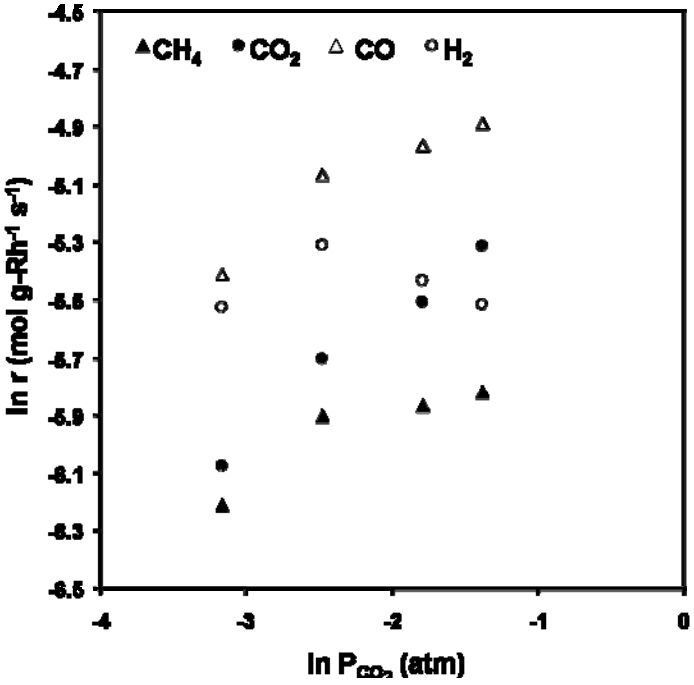
▲CH4 ●CO2 △ CO ○H2
ln r (mol g-Rh-1 s-1)
-4.5
-4.7
-4.9
-5.1
-5.3
-5.5
-5.7
-5.9
-6.1
-6.3
-6.5
-4
-3
-2
-1
0
ln PCO2 (atm)

(c)

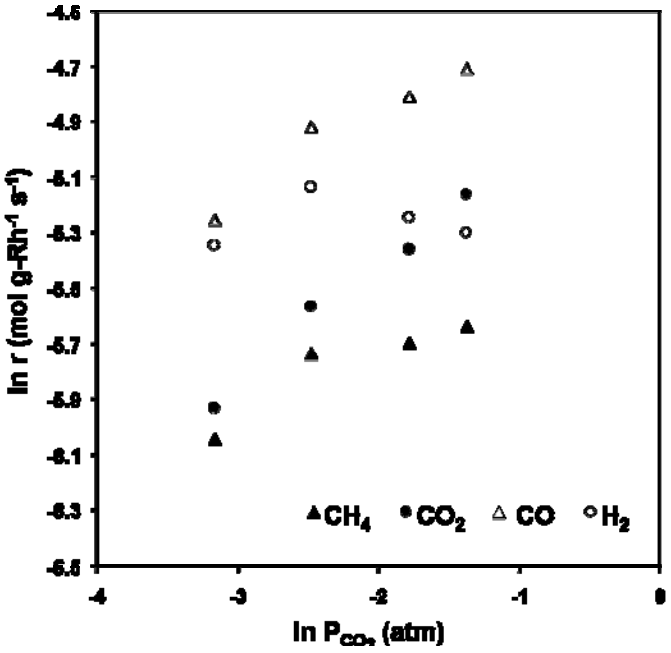

(d)

Fig 5.12. Natural logarithm of reaction rate versus natural logarithm of CO_2 partial pressure at 34,000 1/hr and 500°C (a), 550°C (b), 570°C (c) and 590°C. Inlet partial pressure of CH4 fixed at 0.083 atm.

5.4 Varying inlet CH_4 partial pressure

Wet mole fractions of effluent species are seen versus inlet CH_4 partial pressure in Fig 5.13. As CH_4 partial pressure increases, H_2 and CO mole fraction increase and CO_2 decreases. The most marked changes in mole fraction occur as CH_4:CO_2 increases from 0.5 to 1.

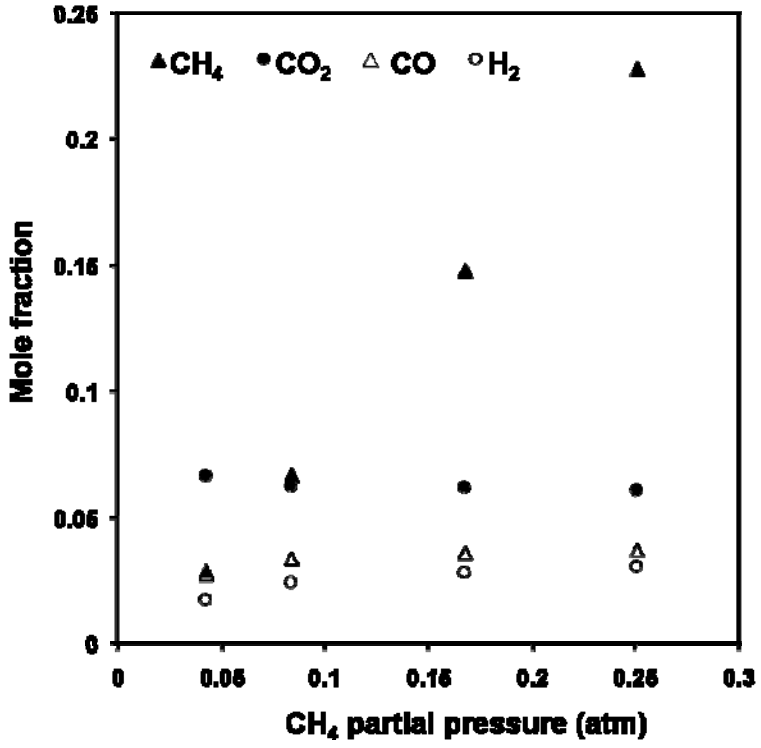
CH4
CO2
CO
H2
Mole fraction
0.25
0.2
0.15
0.1
0.05
0
0
0.05
0.1
0.15
0.2
0.25
0.3
CH4 partial pressure (atm)

(a)

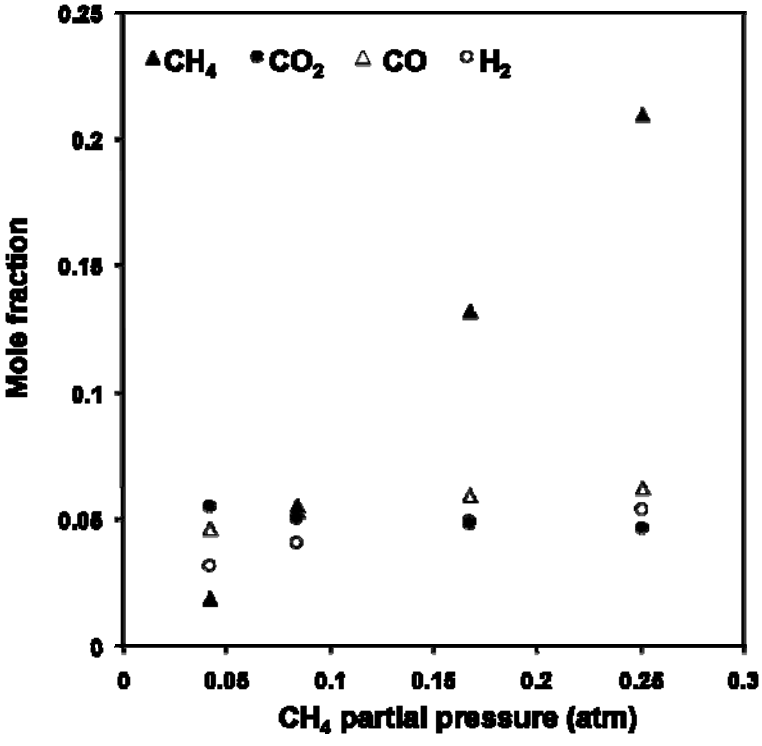
CH4
CO2
CO
H2
Mole fraction
0.25
0.2
0.15
0.1
0.05
0
0
0.05
0.1
0.15
0.2
0.25
0.3
CH4 partial pressure (atm)

(b)

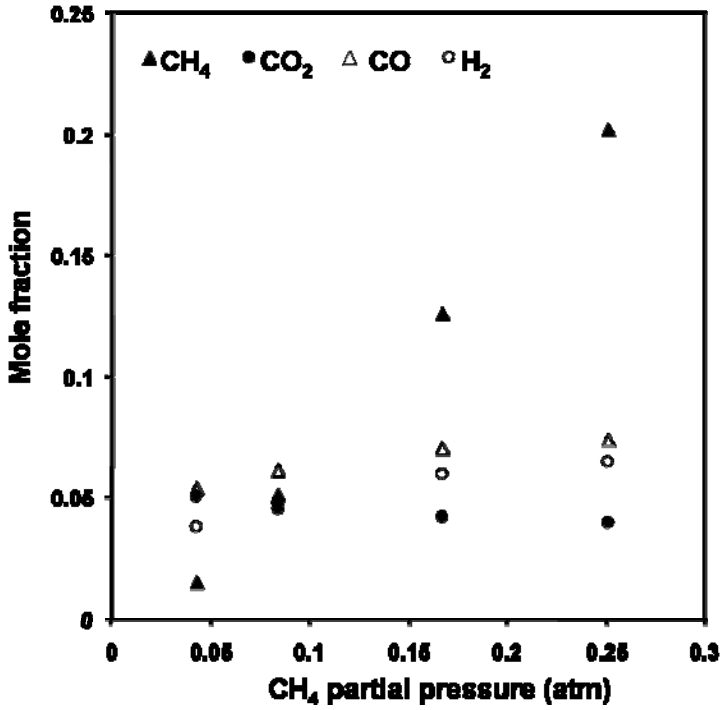

(c)

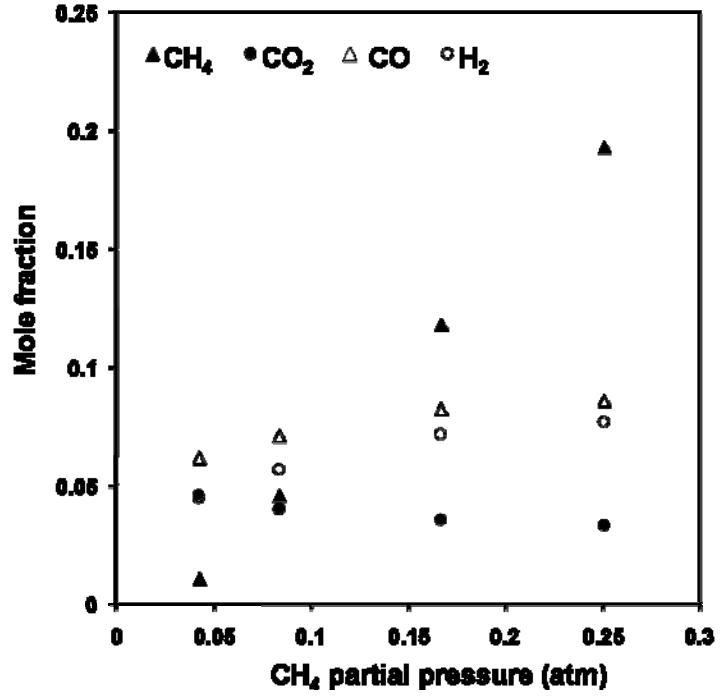

(d)

Fig 5.13. Mole fraction versus CH_4 partial pressure at 34,000 1/hr and 500°C (a), 550°C (b), 570°C (c) and 590°C. Inlet partial pressure of CO_2 fixed at 0.083 atm.

Mole fractions are plotted versus temperature for increasing CH_4 partial pressure in Fig 5.14 (a)-(d). Equilibrium mole fractions are also shown. For each CO_2:CH_4 ratio, and within the experimental temperature range, a strong correlation is seen between the equilibrium calculations and the experimental data. It is also seen that the equilibrium mole fraction of water decreases with increasing CH_4 partial pressure.

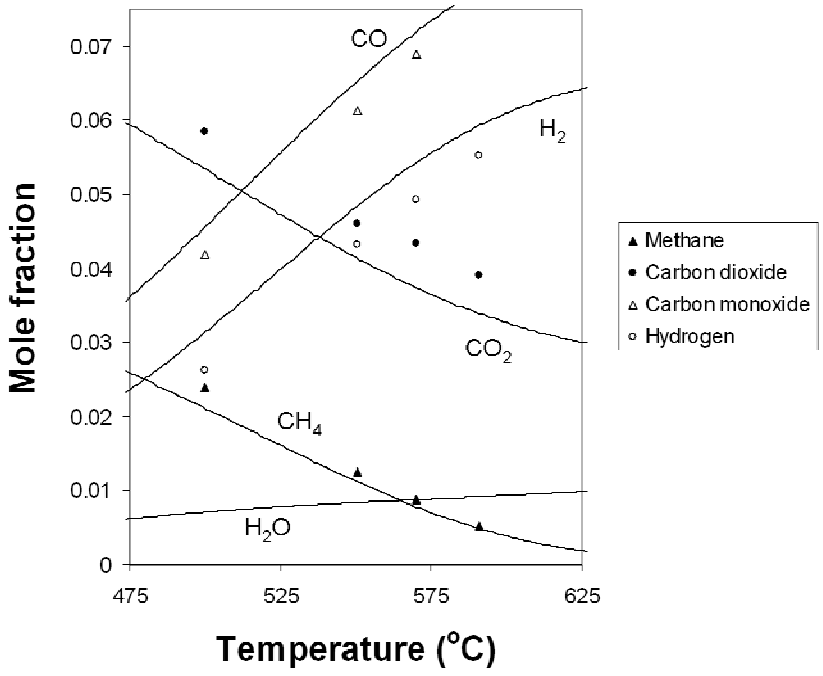

(a)

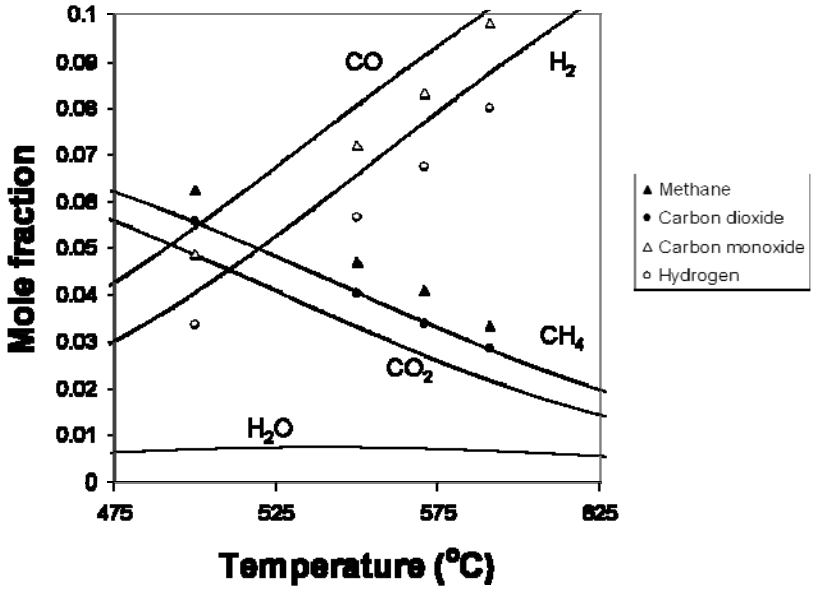
0.1
0.09
0.08
0.07
0.06
0.05
0.04
0.03
0.02
0.01
0
Mole fraction
CO
H2
CH4
CO2
H2O
475
525
575
625
Temperature (°C)
Methane
Carbon dioxide
Carbon monoxide
Hydrogen

(b)

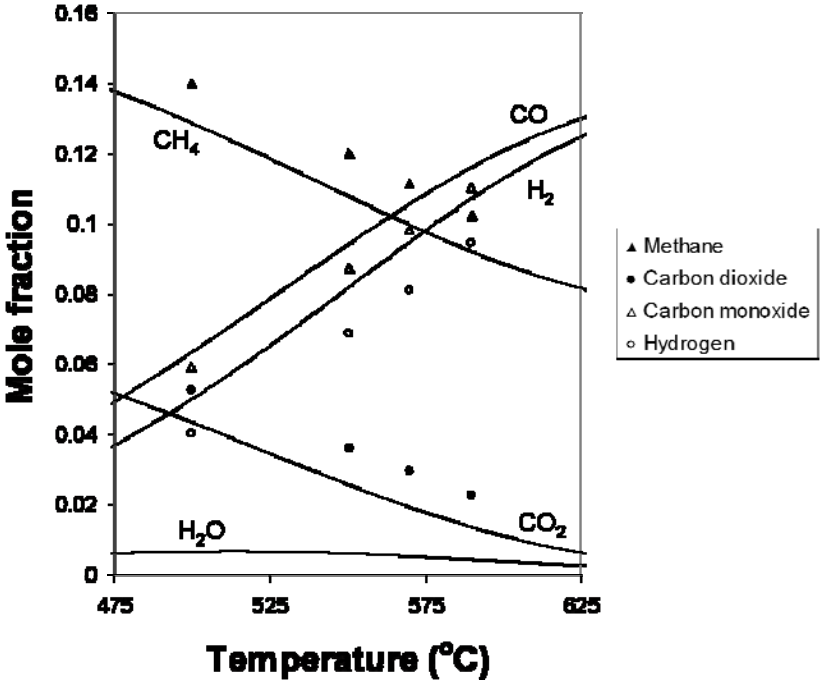
0.16
0.14
0.12
0.1
0.08
0.06
0.04
0.02
0
Mole fraction
CH4
CO
H2
H2O
CO2
475
525
575
625
Temperature (°C)
Methane
Carbon dioxide
Carbon monoxide
Hydrogen

(c)

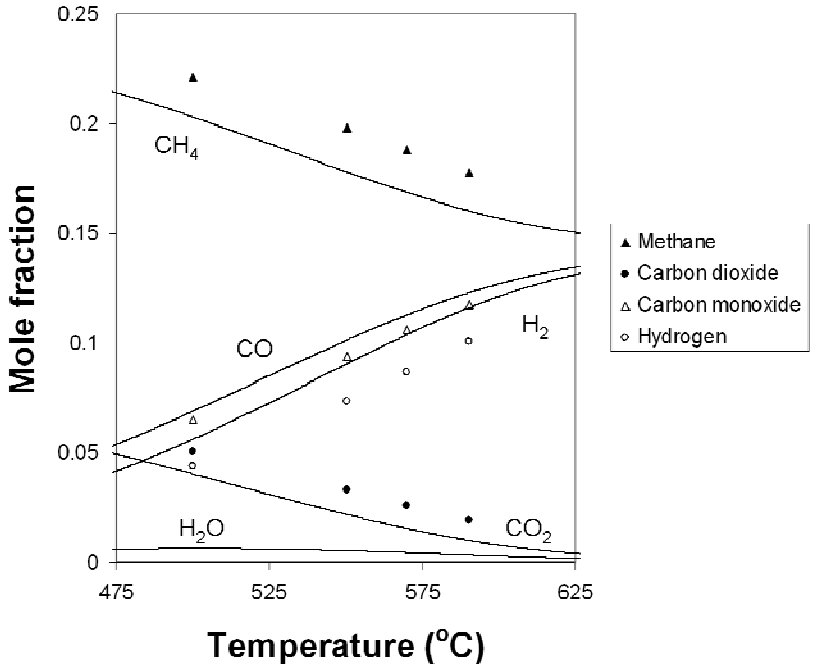

(d)

Fig 5.14. Mole fraction versus temperature at 15,000 1/hr and 0.083 atm CO_2, 0.042 CH_4, 0.875 Ar (a); 0.083 CH_4, 0.083 CO_2, 0.834 Ar (b); 0.17 CH_4, 0.083 CO_2, 0.75 Ar (c); and 0.25 CH_4, 0.083 CO_2, 0.667 Ar (d). Solid lines represent equilibrium calculations.

Turnover frequencies and reaction rates are shown versus CH_4 partial pressure at temperatures of 500-590°C in Figs 5.15-5.16. All rates increase with increasing CH_4 partial pressure, with highest rates seen at the highest temperature. CO turnover and reaction rates are greatest, followed by H_2, CO_2, and CH_4.

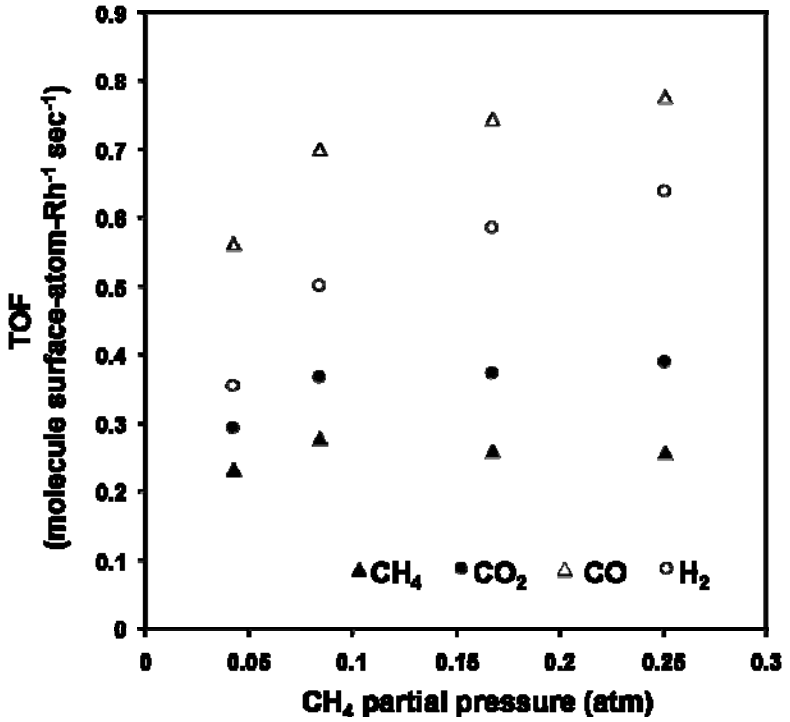
TOF
(molecule surface-atom-Rh-1 sec-1)
0.9
0.8
0.7
0.6
0.5
0.4
0.3
0.2
0.1
0
0
0.05
0.1
0.15
0.2
0.25
0.3
CH4 partial pressure (atm)
CH4
CO2
CO
H2

(a)

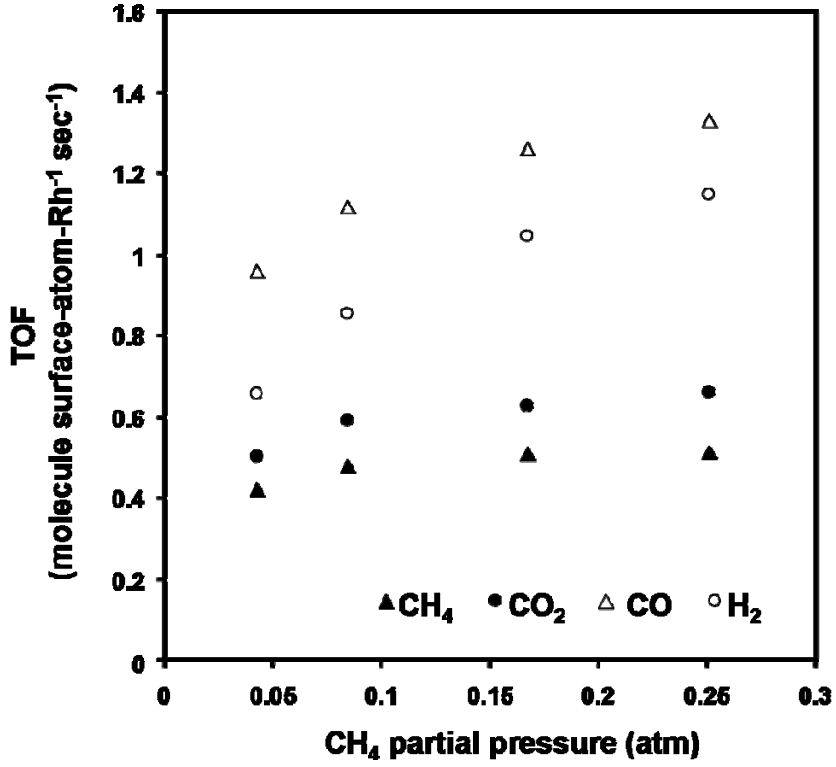
TOF
(molecule surface-atom-Rh-1 sec-1)
1.6
1.4
1.2
1
0.8
0.6
0.4
0.2
0
0
0.05
0.1
0.15
0.2
0.25
0.3
CH4 partial pressure (atm)
CH4
CO2
CO
H2

(b)

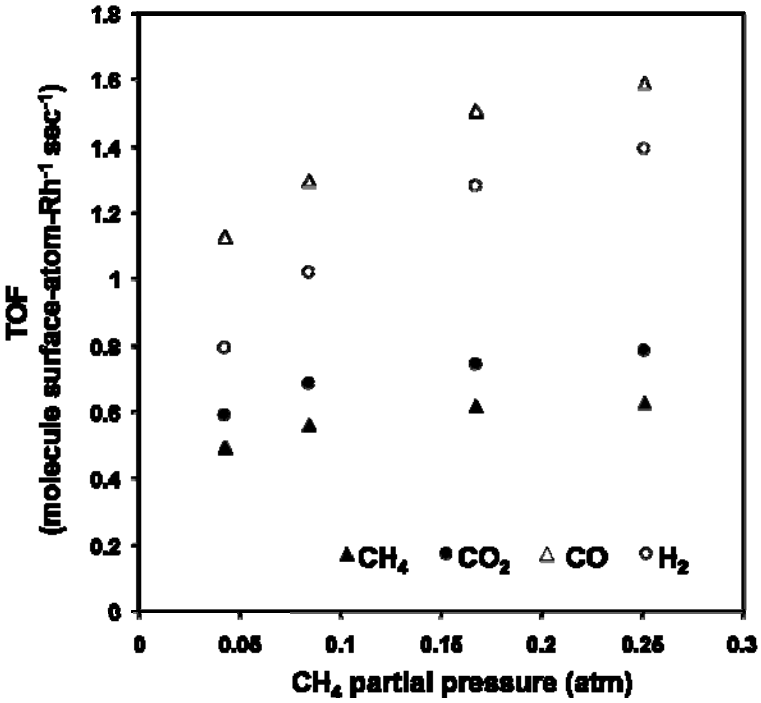

(c)

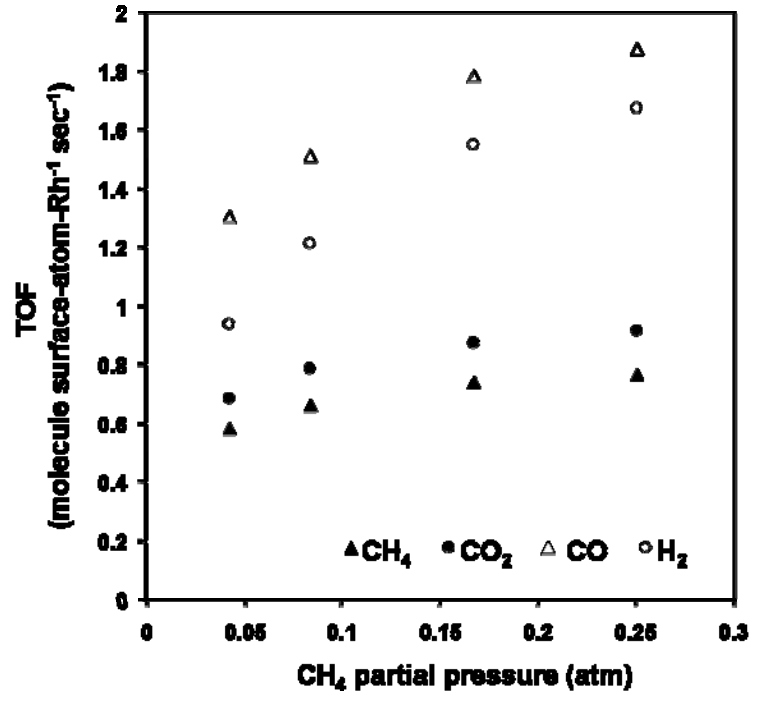

(d)

Fig 5.15. TOF versus CH_4 partial pressure at 34,000 1/hr and 500°C (a), 550°C (b), 570°C (c) and 590°C. Inlet partial pressure of CO_2 fixed at 0.083 atm.

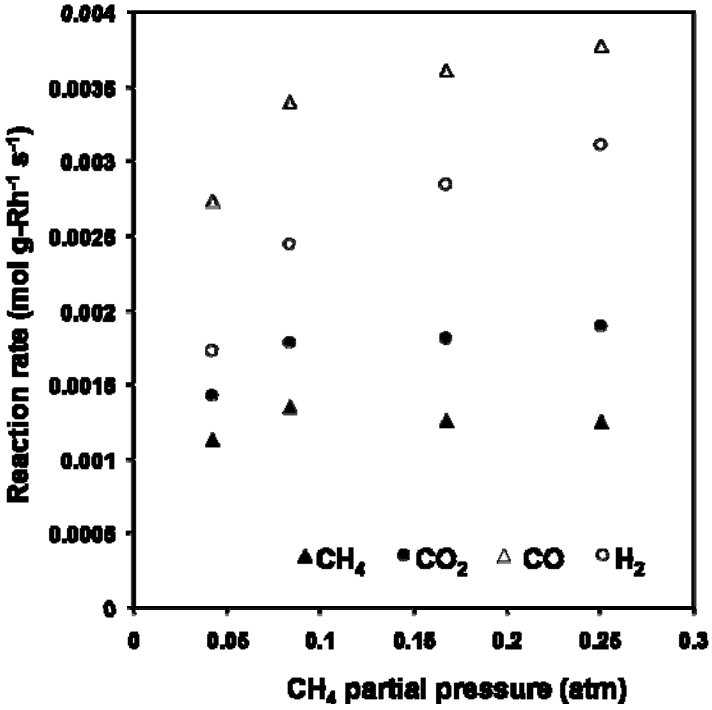
Reaction rate (mol g-Rh^{-1} s^{-1})
0.004
0.0035
0.003
0.0025
0.002
0.0015
0.001
0.0005
0
0
0.05
0.1
0.15
0.2
0.25
0.3
CH_4 partial pressure (atm)
CH_4
CO_2
CO
H_2

(a)

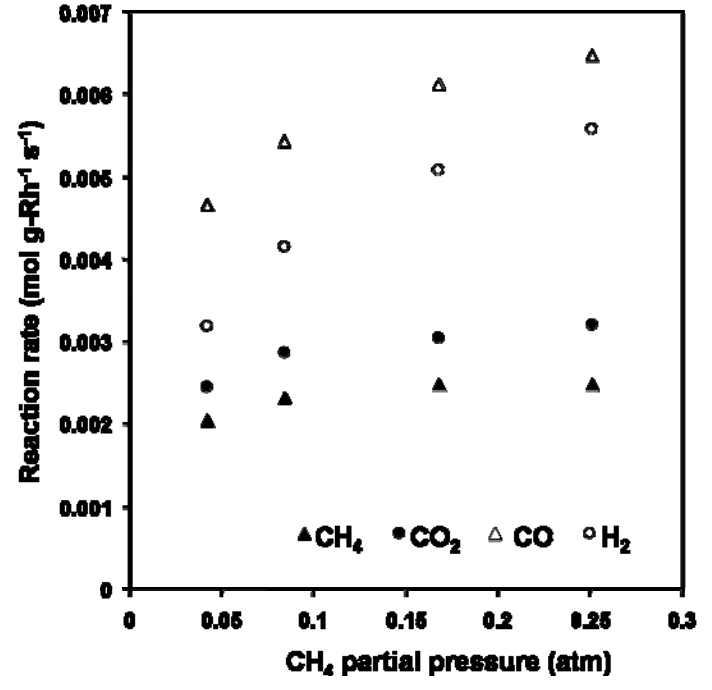
Reaction rate (mol g-Rh^{-1} s^{-1})
0.007
0.006
0.005
0.004
0.003
0.002
0.001
0
0
0.05
0.1
0.15
0.2
0.25
0.3
CH_4 partial pressure (atm)
CH_4
CO_2
CO
H_2

(b)

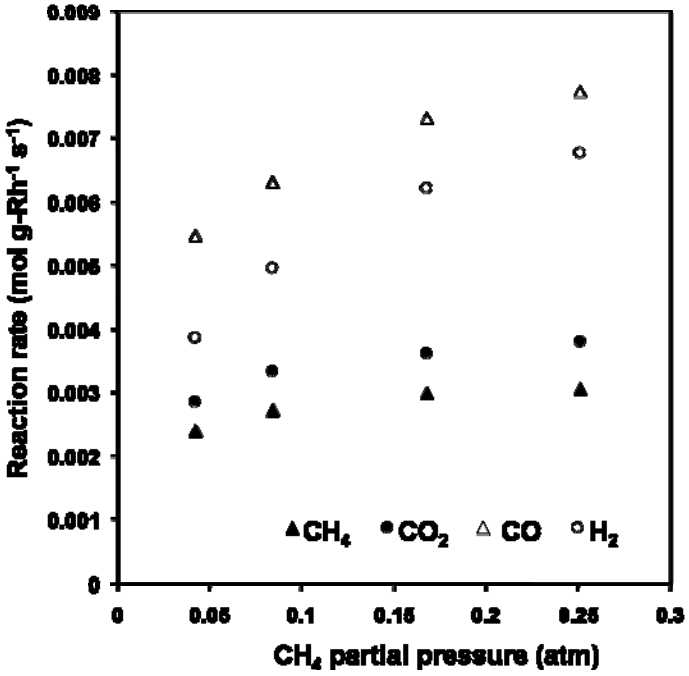

(c)

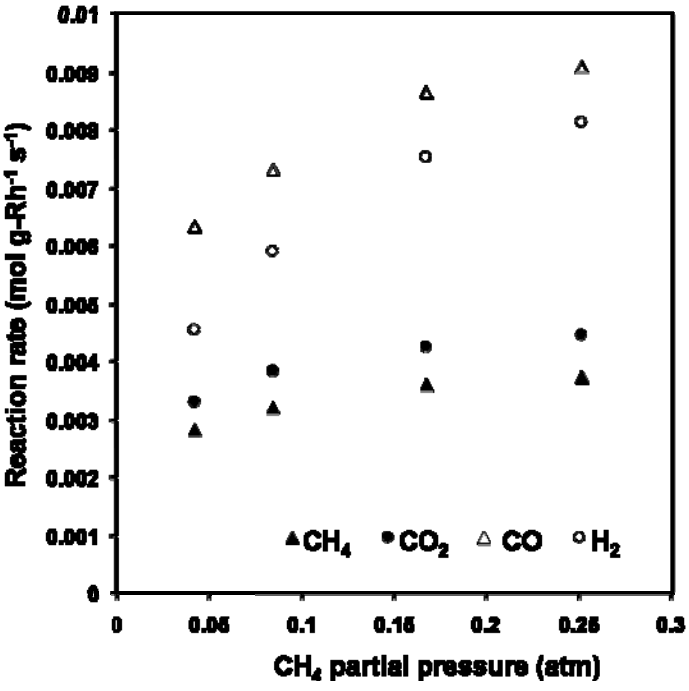

(d)

Fig 5.16. Reaction rate versus CH_4 partial pressure at 34,000 1/hr and 500°C (a), 550°C (b), 570°C (c) and 590°C. Inlet partial pressure of CO_2 fixed at 0.083 atm.

As conducted previously for the CO_2 reaction order, CH_4 reaction order was determined at varying temperatures by plotting the natural logarithm of reaction rate versus the natural log of the inlet CH_4 partial pressure. Beginning with the forward rate expression

$$r_i = k_0 \exp(-Ea/RT) P_{CH4}^{\alpha} P_{CO2}^{\beta},$$

and taking temperature and CO_2 partial pressure to be constant, setting

$$C = k_0 \exp(-Ea/RT) P_{CO2}^{\beta}$$

then, the expression for the rate becomes

$$r_i = C P_{CH4}^{\alpha}.$$

Taking the natural logarithm produces a convenient form of equation to plot in which the slope yields the reaction order, α:

$$\ln r_i = \ln(C P_{CH4}^{\alpha})$$

$$\ln r_i = \ln C + \alpha \ln(P_{CH4})$$

Trendlines were fit to the log-log graphs, and reaction orders are reported in Table 5.2.

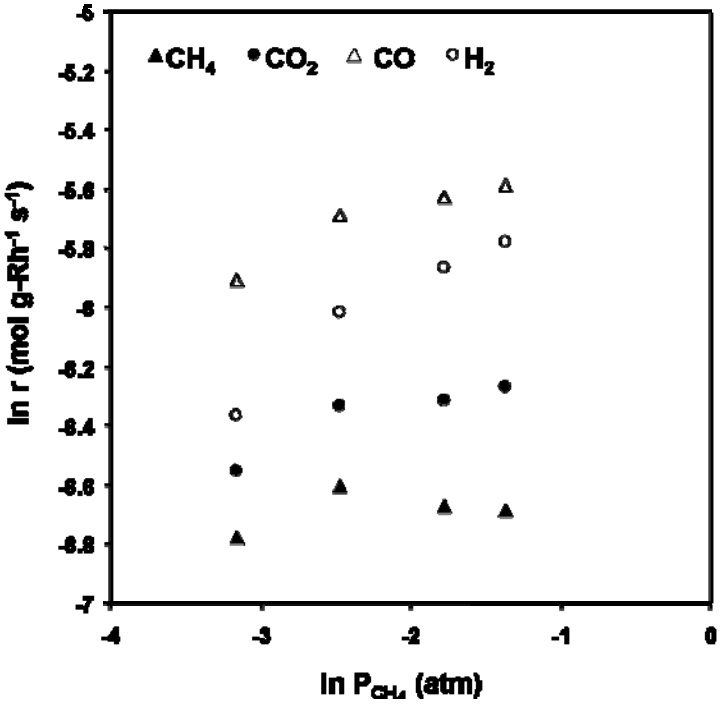
▲CH4 ●CO2 △CO ○H2
ln r (mol g-Rh-1 s-1)
ln PCH4 (atm)
-5
-5.2
-5.4
-5.6
-5.8
-6
-6.2
-6.4
-6.6
-6.8
-7
-4
-3
-2
-1
0

(a)

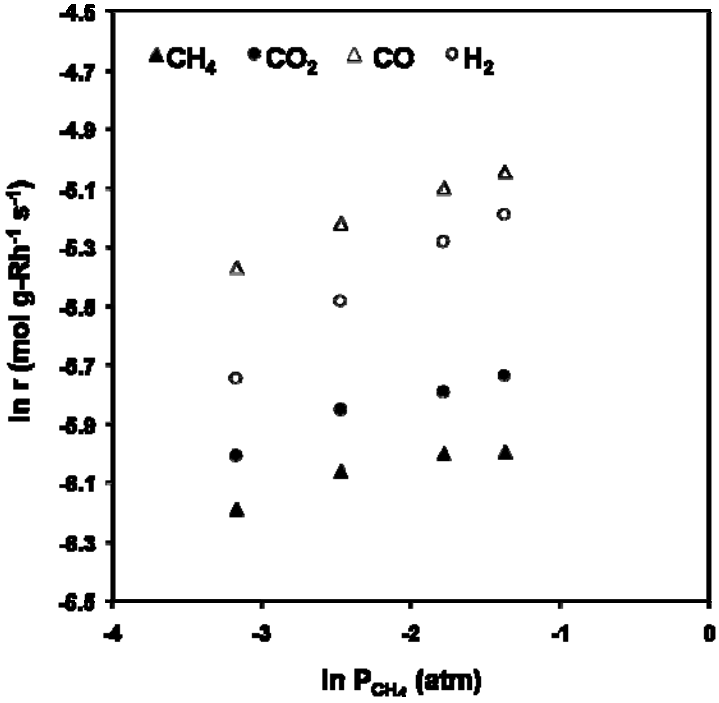
▲CH4 ●CO2 △CO ○H2
ln r (mol g-Rh-1 s-1)
ln PCH4 (atm)
-4.5
-4.7
-4.9
-5.1
-5.3
-5.5
-5.7
-5.9
-6.1
-6.3
-6.5
-4
-3
-2
-1
0

(b)

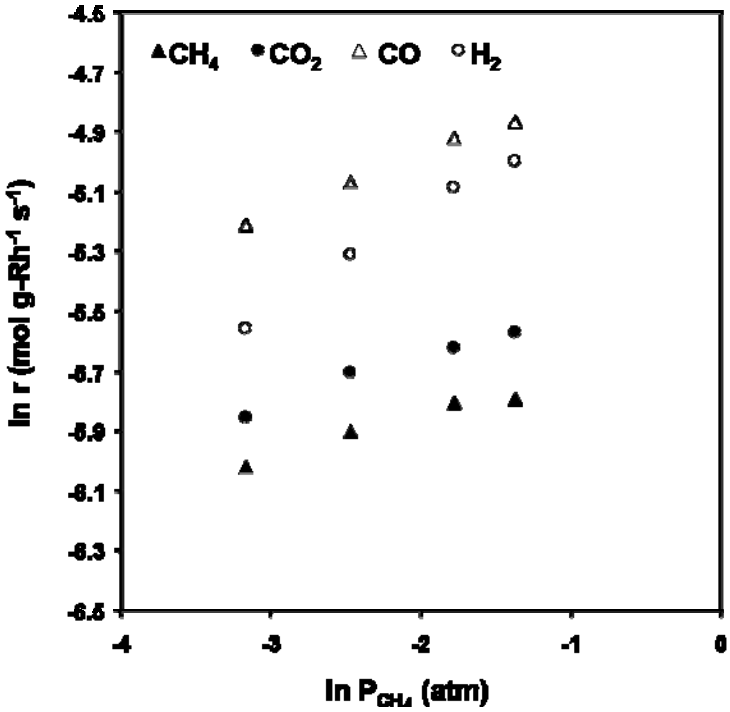

(c)

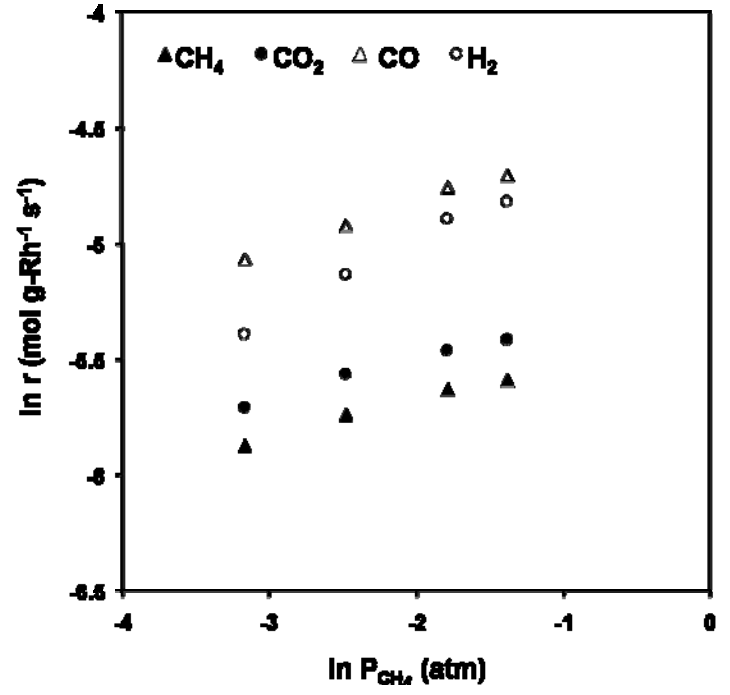

(d)

Fig 5.17. Natural logarithm of reaction rate versus natural logarithm of CH_4 partial pressure at 34,000 1/hr and 500°C (a), 550°C (b), 570°C (c) and 590°C. Inlet partial pressure of CO_2 fixed at 0.083 atm.

Rates and activation energies for dry reforming at various CO_2:CH_4 ratios and temperatures over Rh/Al_2O_3 are summarized in Table 5.1. The rate constants can be calculated using the reported values of A under specific conditions, and the reaction orders reported in Table 5.2. From Table 5.1, it is shown that the activation energies for r_{CO2} and r_{CO} are equivalent at $0.5 \leq CO_2:CH_4 \leq 2$. The highest activation energies are for r_{CH4} at low CO_2:CH_4 ratios, and for r_{H2} for high CO_2:CH_4 ratios. The lowest activation energies are seen for r_{CO2} at high CO_2:CH_4 ratios.

In Table 2, it is shown that when CO_2 is the limiting reactant, the CO_2 reaction order (β) for each species is very high. For r_{CH4}, the reaction order in CH_4 (α) is less than β when CO_2:CH_4 is less than unity, but α is greater than β when CO_2:$CH_4 > 1$. For r_{CO2}, β is greater than α. For r_{CO}, α is less than β when CO_2:CH_4 is less than unity, but α is greater than β when CO_2:$CH_4 > 1$. Also, for r_{CO}, α is about equal to β at high CO_2:CH_4 ratios. The value of α is greatest for r_{H2}, but β is negative for CO_2:$CH_4 \geq 1$, decreasing with decreasing temperature.

Table 5.1. Temp = °C; P = atm; r = 1000 moles g-$Rh^{-1}s^{-1}$; TOF – molecules surface-atom-$Rh^{-1}s^{-1}$; Ea = kCal mol^{-1}; $A = k_o P_{CH4}^{\alpha} P_{CO2}^{\beta}$.

			CH_4				CO_2				CO				H_2			
Temp	P_{CH4}	P_{CO2}	r	TOF	E_a	lnA	r	TOF	E_a	lnA	r	TOF	E_a	lnA	r	TOF	E_a	lnA
600	0.083	0.042	0.83	0.17			1.10	0.23			2.18	0.44			1.76	0.36		
550	0.083	0.042	1.66	0.34	15.04	3.24	1.95	0.40	13.26	1.85	3.82	0.78	13.2	2.47	3.32	0.68	14.95	3.4
570	0.083	0.042	2.03	0.42			2.31	0.48			4.49	0.92			4.01	0.83		
590	0.083	0.042	2.39	0.49			2.67	0.55			5.25	1.08			4.80	0.99		
600	0.083	0.083	1.37	0.28			1.79	0.37			3.42	0.70			2.45	0.50		
550	0.083	0.083	2.35	0.48	12.79	1.74	2.88	0.59	11.35	1.07	5.45	1.12	11.34	1.71	4.17	0.86	13.02	2.47
570	0.083	0.083	2.75	0.57			3.35	0.69			6.34	1.30			4.98	1.02		
590	0.083	0.083	3.25	0.67			3.85	0.79			7.33	1.51			5.93	1.22		
600	0.083	0.166	1.20	0.27			2.08	0.43			3.57	0.73			1.92	0.40		
550	0.083	0.166	2.38	0.49	14.29	2.67	3.48	0.72	12.2	1.78	5.93	1.22	12.32	2.39	3.59	0.74	15.04	3.55
570	0.083	0.166	2.85	0.59			4.09	0.84			7.01	1.44			4.40	0.91		
590	0.083	0.166	3.39	0.70			4.73	0.97			8.19	1.69			5.30	1.09		
600	0.083	0.249	1.44	0.30			2.71	0.56			3.71	0.76			1.66	0.34		
550	0.083	0.249	2.47	0.51	13.52	2.26	4.22	0.87	11.1	1.31	6.34	1.31	13.2	3.00	3.26	0.67	16.37	4.26
570	0.083	0.249	2.99	0.62			4.95	1.02			7.60	1.56			4.06	0.84		
590	0.083	0.249	3.60	0.74			5.76	1.19			9.07	1.87			5.02	1.03		
600	0.042	0.083	1.15	0.24			1.44	0.30			2.75	0.56			1.73	0.36		
550	0.042	0.083	2.07	0.43	13.56	2.07	2.47	0.51	12.54	1.63	4.69	0.96	12.52	2.26	3.21	0.66	14.45	3.07
570	0.042	0.083	2.44	0.50			2.89	0.59			5.51	1.13			3.89	0.80		
590	0.042	0.083	2.85	0.59			3.34	0.69			6.37	1.31			4.57	0.94		
600	0.083	0.083	1.37	0.28			1.79	0.37			3.42	0.70			2.45	0.50		
550	0.083	0.083	2.35	0.48	12.79	1.74	2.88	0.59	11.35	1.07	5.45	1.12	11.34	1.71	4.17	0.86	13.02	2.47
570	0.083	0.083	2.75	0.57			3.35	0.69			6.34	1.30			4.98	1.02		
590	0.083	0.083	3.25	0.67			3.85	0.79			7.33	1.51			5.93	1.22		
600	0.166	0.083	1.28	0.26			1.82	0.37			3.63	0.75			2.86	0.59		
550	0.166	0.083	2.50	0.51	15.56	3.47	3.06	0.63	12.33	1.92	6.15	1.26	12.93	2.8	5.10	1.05	14.35	3.49
570	0.166	0.083	3.03	0.62			3.65	0.75			7.35	1.51			6.25	1.29		
590	0.166	0.083	3.63	0.75			4.27	0.88			8.69	1.79			7.56	1.55		
600	0.249	0.083	1.26	0.26			1.91	0.39			3.79	0.78			3.12	0.64		
550	0.249	0.083	2.51	0.52	16.21	3.89	3.23	0.67	12.36	1.99	6.50	1.34	13.04	2.93	5.60	1.15	14.22	3.5
570	0.249	0.083	3.08	0.63			3.83	0.79			7.77	1.60			6.80	1.40		
590	0.249	0.083	3.76	0.77			4.47	0.92			9.13	1.88			8.15	1.68		

Table 5.2. Temp = °C; $r = k_o e^{-Ea/RT} P_{CH4}{}^{\alpha} P_{CO2}{}^{\beta}$; β_1 for $CO_2:CH_4 \leq 1$; β_2 for $CO_2:CH_4 \geq 1$.

	CH_4			CO_2			CO			H_2		
Temp	α	β_1	β_2	α	β_1	β_2	α	β_1	β_2	α	β_1	β_2
500	0.0397	0.72	0.03	0.1445	0.71	0.36	0.1723	0.66	0.0738	0.32	0.483	-0.355
550	0.109	0.5	0.04	0.1456	0.56	0.34	0.1833	0.51	0.136	0.312	0.33	-0.22
570	0.13	0.439	0.073	0.155	0.537	0.35	0.196	0.5	0.1631	0.317	0.311	-0.186
590	0.157	0.44	0.09	0.163	0.53	0.36	0.208	0.4868	0.19	0.33	0.3	-0.15

Mass balances

Calculations of atom balances for H, C, and O, were conducted to measure the extent at which the GC measurements accounted for all of the species in the effluent mixture. The calculation for percent difference for a specific atom N_i, is given as

$$\frac{Ni_f - Ni_o}{Ni_o} \times 100$$

where Ni_f is the number of atoms detected and Ni_o is the number of atoms fed into the reactor. Results for atom balances are shown in Table 5.3 for varying CO_2:CH_4 ratios and varying temperatures. As expected, as the equilibrium mole fraction of H_2O increases, so does the percentage of H and O atoms that go unaccounted for in the GC measurements of CH_4, CO_2, H_2, and CO.

Table 5.3. Atom balances are shown for varying CO_2:CH_4 ratios and varying temperatures (°C).

		Atom balances (percent difference)		
Temp	CO2:CH4	H	C	O
500	0.5	0.60	1.93	-0.43
550	0.5	0.01	1.71	-1.05
570	0.5	-0.28	1.25	-1.62
590	0.5	0.13	1.57	-1.17
500	1	-1.74	1.60	-1.05
550	1	-3.28	1.36	-1.96
570	1	-3.25	1.47	-2.26
590	1	-3.53	1.62	-2.15
500	2	-4.14	0.79	-1.86
550	2	-7.29	0.29	-3.18
570	2	-8.12	0.30	-3.61
590	2	-9.18	0.29	-3.96
500	3	-7.55	-1.37	-3.56
550	3	-10.44	-1.08	-4.35
570	3	-11.94	-1.04	-4.75
590	3	-13.50	-0.89	-5.08

5.5 Deactivation

During the studies with the Rh/γ-Al_2O_3 monolith catalyst, there was no observed deactivation on the reactor after 24 hours of testing. However, since coke buildup is an important aspect of dry reforming of CH_4 and CO_2, tests were conducted to determine where carbon formation would occur on a catalyst known to form coke during operation.

Plug-flow reactor studies were also performed using a packed bed of Ni based catalyst. Flowing a stoichiometric feed of CO_2 and CH_4, it was found that the Ni catalyst quickly deactivated due to coke build up, plugging the reactor. As seen in Fig 5.18, reforming initially occurred for the first hour, producing a product mixture with H_2:CO ratios greater than unity. However, as coke began to build up, the reactor became plugged, considerable flow to release through the

thermocouple insertion point, increasing the residence time of the gas that actually passed through the reactor. This resulted in an apparent increasing levels of conversion as measured by the GC. The Ni catalyst is shown in the reactor following the study in Fig 5.19.

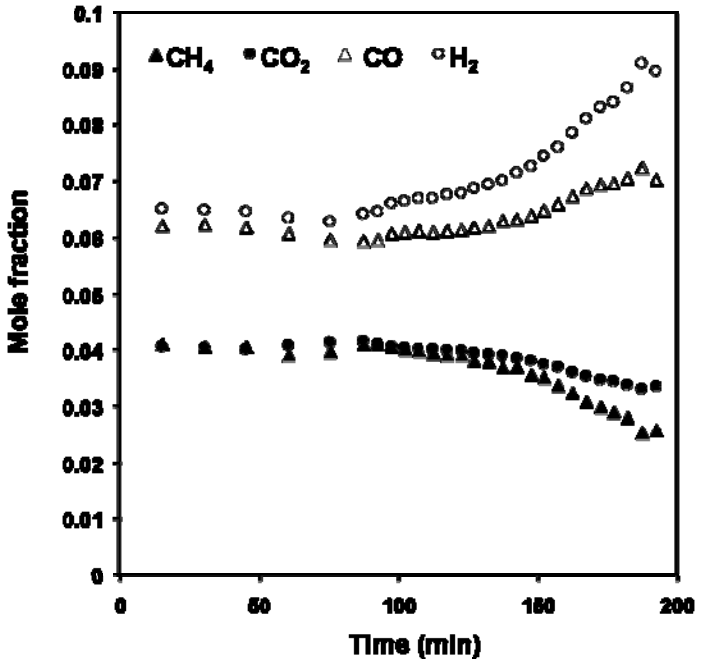

Fig 5.18: Mole fraction versus time at 15,000 1/hr and 540°C for Ni catalyst and inlet gas composition of 0.083 atm CH_4, 0.083 atm CO_2, 0.834 atm Ar.

Fig 5.19. Nickel catalyst following stoichiometric reforming studies. The catalyst began as spherical pellets, but became engrossed by solid carbon buildup.

The extent of catalyst deactivation was also studied on the Rh/γ-Al_2O_3 monolith throughout the reforming investigations. Periodically, initial test conditions were repeated to see if any change in activity had occurred. As seen in Fig. 5.20, activity was consistent for a reforming time period of 25 hours.

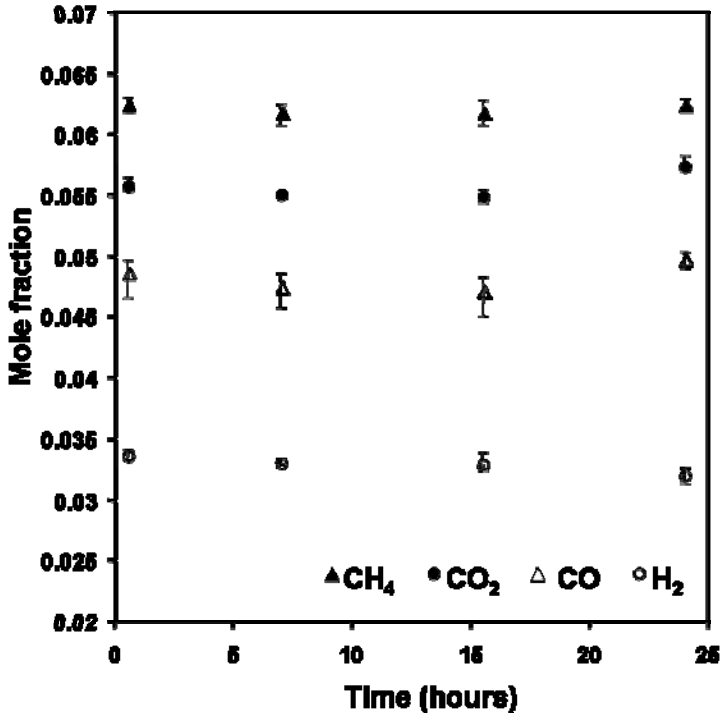

Fig 5.20. Mole fraction versus time at 15,000 1/hr and 500°C for Rh catalyst and inlet gas composition of 0.083 atm CH_4, 0.083 atm CO_2, 0.834 atm Ar.

Deactivation on Rh was also studied using thermogravimetric analysis. Mass percent change was measured versus time for a stoichiometric feed of reforming gas at two isothermal temperatures, as seen in Figs 5.21 and 5.22. The mass percent change at 550°C was greater than the mass percent change at 590°C. After the dry reforming run at 550°C in the TGA, the catalyst sample was subjected to an oxidizing atmosphere to measure the mass percent change simultaneously differential thermal analysis. The quantitative results from this experiment were

inconclusive. However, it was witnessed that the yellowish Rh/γ-Al_2O_3 powder turned dark gray after the reforming, and was then returned to its original yellowish color after the oxidation.

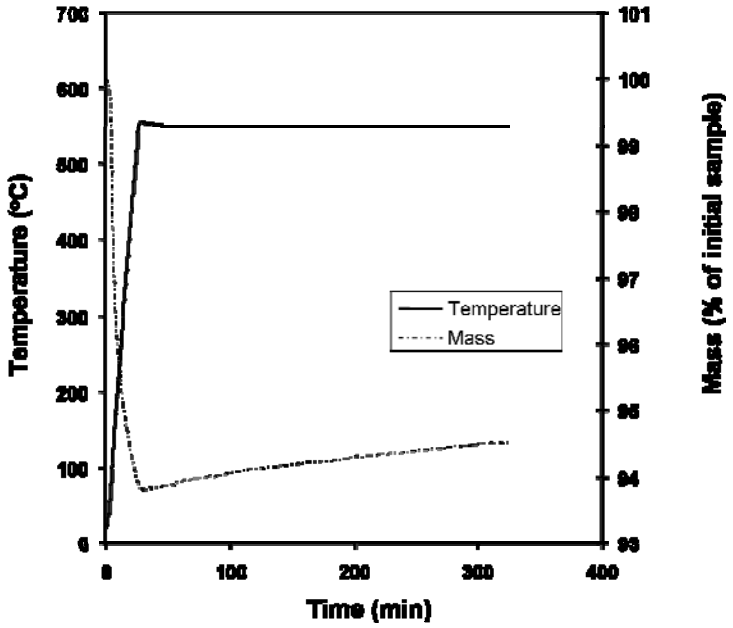

Fig 5.21. Mass percent change versus time for temperature ramping to 550°C for Rh catalyst and inlet gas composition of 0.083 atm CH_4, 0.083 atm CO_2, 0.834 atm Ar

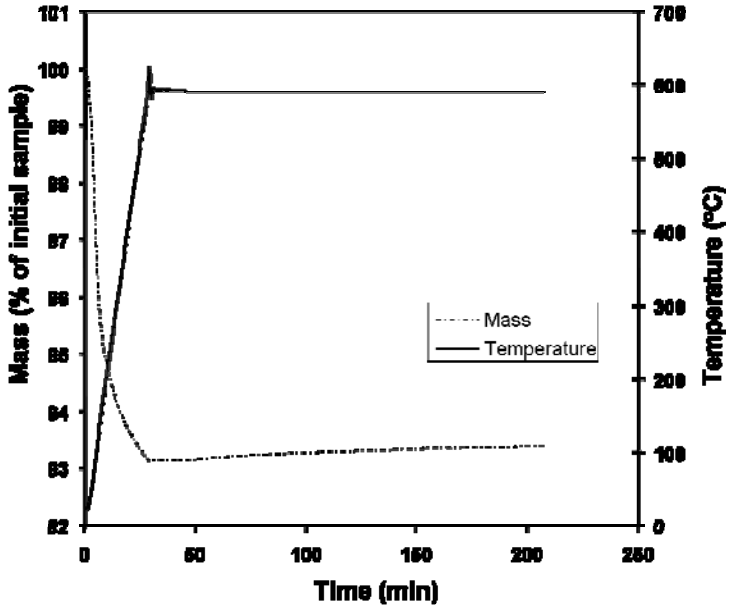

Fig 5.22. Mass percent change versus time for temperature ramping to 590°C for Rh catalyst and inlet gas composition of 0.083 atm CH_4, 0.083 atm CO_2, 0.834 atm Ar

5.6 Catalyst poisoning from heavy metal deposition.

During dry reforming testing with the Rh/γ-Al_2O_3 monolith, deactivation from coke buildup was experienced due to faulty procedure. A thin copper tube was used to push the monolith into the reactor, which resulted in a deposition of Cu onto the catalyst, facilitating coke buildup and catalyst deactivation. This was avoided by using a glass tube instead of the copper tube.

6. DISCUSSION

In the temperature range in which thermodynamics predict severe coking to occur, the Ni based catalyst produced large amounts of coke while the Rh/γ-Al_2O_3 monolith catalyst was stable, displaying an impressive kinetic inhibition towards the pathways which lead to coke formation. Thermodynamic calculations indicated that CO disproportionation would be the likely route to carbon deposition during dry reforming, and the Rh/γ-Al_2O_3 monolith proved to inhibit this side reaction. At low space velocities, experimental measurements of CH_4, CO_2, H_2, and CO mole fractions were within at least 5 % of thermodynamic equilibrium calculations which were conducted without allowing for the formation of solid carbon. While a catalyst cannot alter the thermodynamics of a reaction in terms of the enthalpy or Gibbs free energy, which dictates equilibrium conditions, it can produce a new reaction pathway which serves to inhibit certain intermediate steps, altering the concentrations of product species. This was exhibited by the Rh/γ-Al_2O_3 monolith catalyst.

As net reaction rates over the Rh/γ-Al_2O_3 monolith were found to be increasing with increasing space velocity up to 34,000 1/hr, it was postulated that the reaction was not kinetically controlled, but rather limited by transport in the form of bulk mass transfer. For this reason, a kinetic study of the forward reaction rates was not appropriate. At the highest space velocity, however measured mole fractions were far off from equilibrium (30-40 % away). For these reasons, an examination of the dry reforming kinetics in terms of net rates including secondary processes, but estimated as unaffected by approach to equilibrium, was conducted.

It was found that the activation energy of r_{CO2} was equal to the activation energy of r_{CO} at all feed ratios except for CO_2:CH_4 of 3. This suggests that the kinetically relevant step which produces CO is the same step which consumes CO_2. The likely elementary step, as originally proposed by Bodrov, is:

$$CO_2 + * \rightarrow CO + O*$$

This also means that the kinetically relevant pathway to CO production lies in the activation of CO_2, rather than the activation of CH_4, subsequent H extraction, and C oxidation seen in steps 1-6 proposed by Wei and Iglesia.

For r_{CH4}, it is seen that the activation energy decreases with increasing CO_2:CH_4. This likely means that CH_4 activation is facilitated by the presence of CO_2 or one of its products of dissociation, such as O. While CH_4 activation may be also aided by the presence of H_2O (or OH) which would be present at higher CO_2:CH_4 ratios, H_2O cannot be produced unless CH_4 is first activated. So, it is postulated that adsorbed O facilitates CH_4 activation, agreeing with Erdohelyi's conclusions but disagreeing with Rostrup-Nielsen's findings over Ni.

These findings gives two-fold support to the prediction that ceria would be a positive contributor to the dry reforming catalyst. Firstly, ceria has been shown to possess high numbers of basic sites, which selectively favor the conversion of CO_2 to CO, which has been shown here to be a slow step. Secondly, ceria has been shown to be a good oxygen storage component, with the ability to store and release O, which can activate the CH_4. With CH_4 activation commonly assumed to be rate limiting, ceria would aid the kinetics of both slow steps.

At stoichiometric reforming conditions, the activation energy for r_{H2} is about equal to the activation energy for r_{CH4}. However, Ea for r_{H2} increases with increasing CO_2:CH_4, as opposed to Ea for r_{CH4}. This may mean that H atoms combine with excess O atoms to form OH, which then combines with another H atom to form H_2O, significantly competing with the formation of H_2 and increasing the activation energy.

The mechanism proposed by Wei and Iglesia is valid within these conclusions based on calculations using net rates, except for the fact that CO_2 activation becomes a kinetically relevant step. Dependency on CO_2 is further substantiated when reaction orders are examined. For r_{CH4}, the average reaction order for CH_4 is 0.11, while the average reaction order for CO_2 is 0.29. For r_{CO2}, the average reaction order for CH_4 is 0.15, while the average reaction order for CO_2 is 0.47. This appears to conflict with Wei and Iglesia's findings that r_{CH4} and r_{CO2} were solely dependent on CH_4; Wei and Iglesia's finding that r_{CO2} is solely dependent on CH_4 is most remarkable, suggesting that CO_2 is not catalytically converted to another species unless CH_4 is present.

7. CONCLUSIONS

It has been shown that a Rh/γ-Al_2O_3 monolith can be an effective catalyst for CO_2-reforming of methane at CO_2:CH_4 ratios from 0.3-3.0, showing stable activity at conditions which thermodynamically predict the formation of solid carbon. TGA tests did reveal slight mass increases on Rh/γ-Al_2O_3 powder at stoichiometric feed ratios and temperatures of 550°C and 590°C, so it is recommended that further studies be performed to determine the cause for the change in mass and the identity of the deposited species. In addition, it is suggested that alternative Rh-based catalyst formulations, including ceria promotion, be designed to hasten the kinetics of the slowest steps and further suppress carbon deposition. As the dry reforming of methane has been shown to be highly dependent on CO_2 in regimes of relatively high conversions, likely due to the facilitation of CH_4 activation by O, it is recommended that other oxygen-containing species be added to the system, either in the form of H_2O or pure O_2. The addition of pure O_2 would also serve the purpose of adding energy for the strongly endothermic reforming reaction, which is commonly heat-transfer limited at levels of high-throughput, via partial oxidation of methane.

CMASS Technology Demonstrations

1. Executive Summary

Catalytic ammonia synthesis and decomposition experiments were conducted to determine the scaling for ammonia synthesis and decomposition reactors onboard a Walrus reference vehicle. It was determined that in order to synthesize 100 tons of ammonia over 72 hours, a 0.67 m^3 bed of iron-based catalyst weighing 2.2 tons would be needed at operating conditions of 150 bar, 435 °C, and space velocity of 15,000 $Nm^3/m^3/hr$. To decompose ammonia at a rate of 100 tons over 72 hours, a nickel-based reactor would need to be 0.72 m^3 and would weigh 0.82 tons, while a rhodium based reactor would be 0.67 m^3 and would weigh only 0.33 tons at operating conditions of atmospheric pressure, 615 °C, and space velocity of 3,200 ml NH_3 STP/cm^3 catalyst/hr. The performance of the catalyst systems went as expected and deliverables were met according to schedule. This report satisfies the program deliverables and thus completes the program.

2. Ammonia Synthesis

2.1 Introduction

Experiments were performed using a Parr Instruments benchtop pressure vessel to synthesize ammonia (NH_3) from nitrogen (N_2) and hydrogen (H_2) gas in the presence of an iron-based catalyst. The purpose of the experiments was to determine the catalytic reaction rate of ammonia synthesis under different operating conditions, which can then be used to extrapolate the size and performance of the Walrus reference vehicle system.

The catalyst was procured from Süd-Chemie specifically for the ammonia synthesis process and is used widely throughout the ammonia synthesis industry. Unlike traditional iron-based catalyst ammonia synthesis catalysts, Süd Chemie's AmoMax-10 is based on a non-stoichiometric ferrous oxide, so-called wustite ($Fe_{1-x}O$). This catalyst has been shown to provide a higher activity than the stoichiometric ferrous oxide, magenetite (Fe_3O_4), due to the cubical crystal structure of wustite which provides superior pore structure and higher surface area, as well as better mechanical strength than the magnetite-based catalyst. Other additives which serve to promote and stabilize the catalyst include aluminum oxide, calcium oxide, potassium oxide, and other undisclosed co-catalysts, with each additive composing less than 5 percent of the catalyst by weight. The bulk density of the un-reduced Amomax-10 catalyst is between 3.0 and 3.3 kg/l and was purchased at a sample price of $500/liter.

The primary results, discussed in detail in the **Results** section, are that the catalyst performed as expected in terms of reaction rates of NH_3 synthesis. All goals were met in terms of time and performance.

2.2 Experimental Setup

The ammonia synthesis reactor is shown in a schematic in Figure 1. It consists of a high-pressure, high-temperature Parr Instruments Model 4642 vessel assembly. The removable vessel holds an internal volume of 2 liters and contains a suspended catalyst basket capable of holding a maximum of 150 cm^3 of catalyst. To ensure that the inlet mixture of N_2 and H_2 flowed directly through the catalyst bed, a stainless steel tube was fitted from the gas inlet inside the top of the reactor down to the crest of the catalyst basket, shifting the point of mixing closer to the catalyst bed. The vessel is sealed with a high-temperature flexible graphite gasket with 35 ft-lbs of torque, allowing a maximum pressure rating of 1900 psi. The reactor pressure is read by a pressure transducer atop the vessel, and the reactor temperature is read by a J-type thermocouple inserted into a thermowell inside of the vessel. The thermocouple also serves as the reference for the PID temperature controller, Parr Instruments Model 4835. The temperature controller serves to heat and control the temperature via a Parr Instruments heater assembly Model 4913 which encases the reactor vessel.

The mass flowrate and stoichiometry of the inlet H_2 and N_2 are controlled with Aalborg GFC17 mass flow controllers which are fed by tanks of ultra-high-purity gas, delivered at 500 psi via high pressure regulators. After passing through the reactor vessel, the gaseous mixture exits into a high-pressure condensing unit at room temperature. As the hot gas flows out the top of the condensing unit, thermal energy is absorbed via a heat exchanger comprised of an adjacent, parallel channel of cooling water flow. This exchange of heat causes the ammonia to condense into liquid phase and drip down to accumulate at the bottom of the sampling vessel. After a given amount of time, the condensed ammonia was released into an Erlenmeyer flask which was resting in an ice bath. The ammonia was then weighed to determine the production

rate and reaction rate. In addition, the gaseous mixture exiting from the top of the condensing unit was sent to an Agilent 3000 Micro GC instrument to analyze the concentrations of the species and detect any ammonia that failed to condense.

An alternative method of measuring the production rate and reaction rate was also employed to minimize the uncertainty of the measurement. The cooling water flow was turned off to the heat exchanger, thus allowing any produced NH_3 to remain in the vapor phase, the exit at the top of the condensing unit was closed with an on-off valve, and the line to the GC was removed. With all of the reacted and un-reacted products still in vapor phase, the gaseous mixture released into the condensing unit and was then channeled out the bottom of the condensing unit to the line connecting to the Agilent 3000 Micro GC instrument to analyze the concentrations of the species. Finally, the products were vented to a hood. This method of analysis allowed for simultaneous detection of all species in the entire product stream.

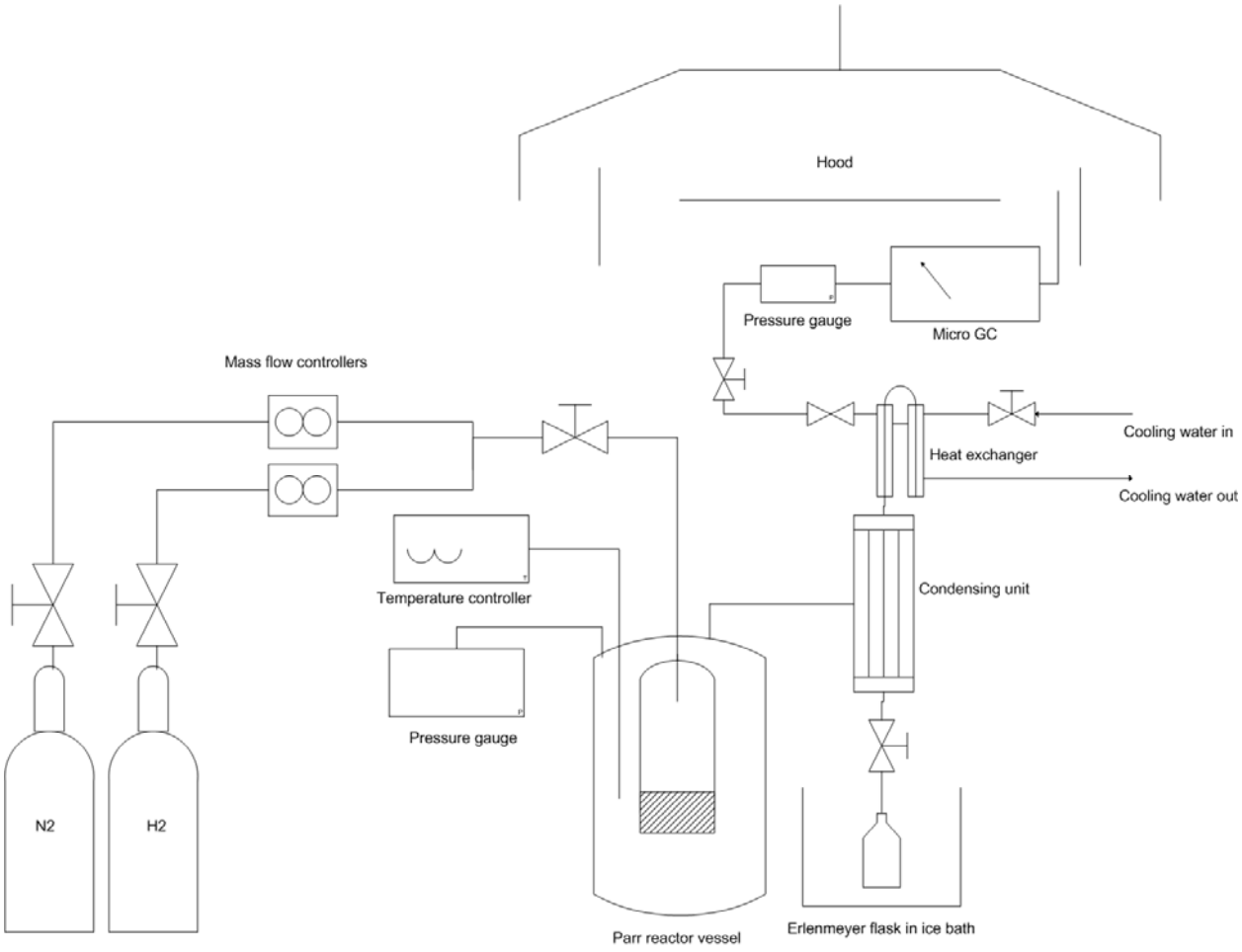

Figure 1: Schematic of ammonia synthesis system.

Figure 2: Parr Instruments reactor assembly fixed to the condensing unit which is attached to an Erlenmeyer flask resting in an ice bath.

Figure 3: Parr Instruments 4835 temperature controller and Aalborg GFC17 mass flow controllers.

Figure 4: Agilent 3000 Micro GC and notebook computer to acquire gas chromatograph data.

2.3 Experimental Procedure

1) Reactor assembly.
    a. The reactor vessel was removed from the heating unit, opened, and the iron catalyst was loaded into the catalyst basket.
    b. A graphite gasket was placed around the diameter of the opened vessel and the vessel was closed.
    c. The split ring was fastened around the top of the vessel, and the reactor was sealed with 35 ft-lbs of torque via a torque wrench.
    d. The final ring enclosure was finger-tightened and the vessel was placed back into the heating unit.
2) Mass flow controllers were powered on and the temperature controller was set to the desired temperature.
3) All connections were checked on the reactor and condensing unit and the cooling water was turned on. The line to the GC was unattached so that the gas would initially vent directly to the hood. All valves were closed.
4) Purging and charging the system.
    a. The nitrogen tank was linked directly to the reactor vessel and the valve between the gas inlet on the reactor and the nitrogen regulator was opened.
    b. The nitrogen tank was opened and the delivery pressure was slowly increased to 300 psi, so that 300 psi of nitrogen filled the reactor.
    c. The outlet valve on the nitrogen regulator was closed.

d. The outlet valve from the bottom of the condenser was opened slowly so that the high pressure gas was vented from the reactor until the pressure gauge read 50 psi.

e. In the same manner, 300 psi of nitrogen was added to the reactor and purged twice more.

f. Finally, 300 psi of nitrogen was charged into the reactor and the vessel was sealed.

5) The mass flow controllers were attached to the respective gas cylinders and to a tee connection which fed into the reactor.

6) With the setpoint of the MFCs set to zero, the gas cylinders were opened and the delivery pressure was increased to 300 psi.

7) The valve between the gas inlet on the reactor and the MFCs was opened causing the reactor pressure to decrease slightly below 300 psi.

8) The MFCs were set to deliver a 3:1 stoichiometric ratio of hydrogen to nitrogen at 700 ml/min hydrogen and 233 ml/min nitrogen.

9) As the pressure built inside the reactor, the delivery pressure at the gas cylinders was increased to maintain a pressure differential of about 25-50 psi. This was done until the maximum pressure of 500 psi was reached on the inlet of the MFCs, and the reactor pressure read 450 psi.

10) The outlet gas valve was opened from the top of the condensing unit, and a downstream needle valve was used to control the outlet flow from the reactor. In order to ensure a constant mass balance in and out of the reactor, the outlet flow was adjusted such that the

reactor pressure was fixed at 450 psi. A more sensitive pressure transducer was used as reference while making small adjustments to the outlet flow with the needle valve.

11) The line to the GC was attached.

12) GC samples were taken until a 3:1 ratio of hydrogen and nitrogen was seen, indicating that steady state had been reached.

13) Any condensed ammonia was then purged from the bottom of the condenser by quickly opening and shutting the valve.

14) The time was recorded and a sample was then accumulated over a desired time period of between 5 and 8 hours. During this time, constant attention was given to the outlet flowrate to ensure that the pressure stayed fixed at 450 psi.

15) Every half hour, the reactor temperature and pressure were recorded, as well as GC samples taken. In addition, the cooling water flowrate was measured by using a stopwatch to time how long it took to fill a 250 ml graduated cylinder.

16) One hour before the sample period would end, an ice bath was filled so that an Erlenmeyer flask would be brought down to a cool temperature before liquid ammonia was released into the flask.

17) When the end of the sampling time had been reached, a needle valve was opened slowly to allow liquid ammonia to drip into the Erlenmeyer flask. Once all of the liquid had been drained, the valve was closed.

18) The flask containing the ammonia was then taken to a scale and weighed.

19) Reactor shutdown.

    a. The heating unit was turned off.

    b. The valve at the top of the condensing unit was closed.

c. Gas cylinders were closed and the MFCs were set to zero flowrate.

d. The valve at the bottom of the condenser was opened slowly to purge the gas from the system.

e. The MFCs were then detached at both ends and powered off.

f. The temperature controller was powered off, the line to the GC was detached, and the cooling water to the heat exchanger was turned off.

20) After the reactor had cooled, the vessel was removed, opened, and the catalyst was removed and weighed.

2.4 Results

Experimental determination of ammonia production rates and catalytic reaction rates were found to be consistent with expected trends and were found to be on the order of expected values. As Figure 5 shows, the molar fraction of ammonia in the outlet stream initially increases with increasing temperature due to kinetics, but then becomes limited by the thermodynamic equilibrium, which decreases with increasing temperature.

After conducting the synthesis experiments with a catalyst bed of 0.42 kg, it was hypothesized that the same ammonia production rate could be met with less catalyst. It was expected that the rate of the synthesis was being limited by thermodynamics rather than the amount of catalyst, so the amount of catalyst was reduced to 0.017 kg, based on the expected reaction rate at 31 bar from the expected trend shown in Figure 8.

The hypothesis was confirmed when the space velocity was increased to 10,000 1/hr from 400 1/hr and roughly the same output of NH_3 was achieved. The discrepancies between NH_3 mole fractions at a given temperature and different space velocities is attributed to uncertainties

arising from different methods of NH3 measurement. At the space velocity of 400 1/hr, the mole fraction was calculated based on the weight of a sample of condensed ammonia taken over a given time period. This was likely to be significantly less than the total amount of ammonia synthesized, as it did not take into account the ammonia which was in vapor phase or the ammonia that was vaporized as the condenser was opened to take the sample. The data obtained at a space velocity of 10,000 1/hr was obtained through a more sensitive GC analysis.

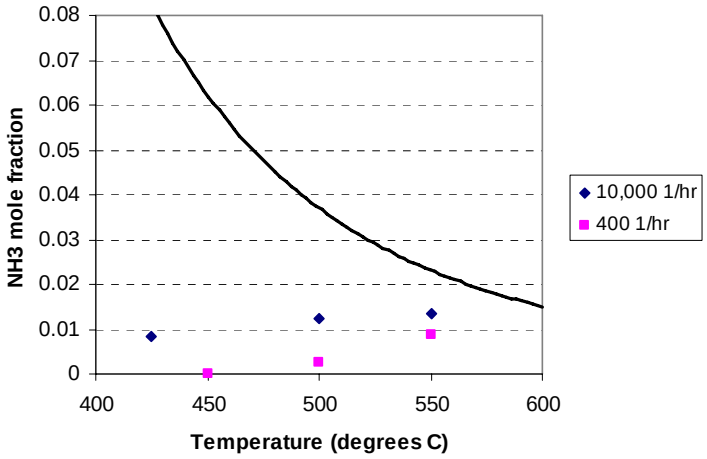

Figure 5: NH_3 mole fraction is shown as a function of temperature at 31 bar. The solid line represents the equilibrium limitation. With a constant inlet flowrate of 700 ml/min H_2 and 233 ml/min N_2 at STP, the higher space velocity data was acquired with a catalyst bed of 0.017 kg, while the lower space velocity was acquired with a bed of 0.42 kg.

NH_3 production rates and reaction rates are shown as a function of temperature in Figures 6 and 7. The rate of reaction increases initially due to increasing temperature, but begins to slow as the reaction becomes more significantly influenced by the thermodynamic equilibrium.

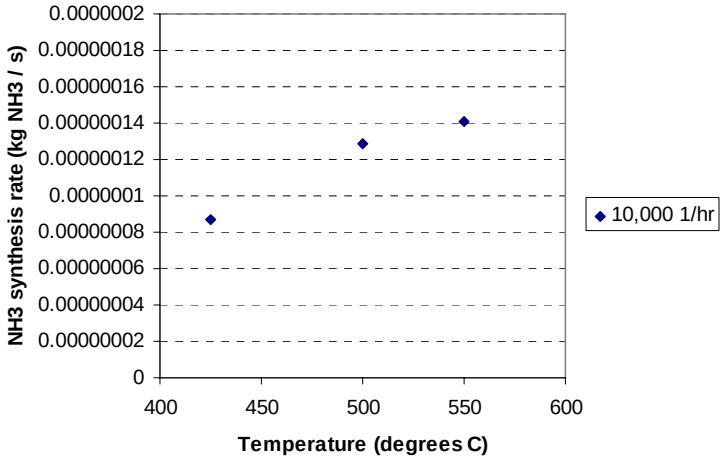

Figure 6: NH_3 synthesis rate is shown versus temperature. Weight of the catalyst = 0.017 kg.

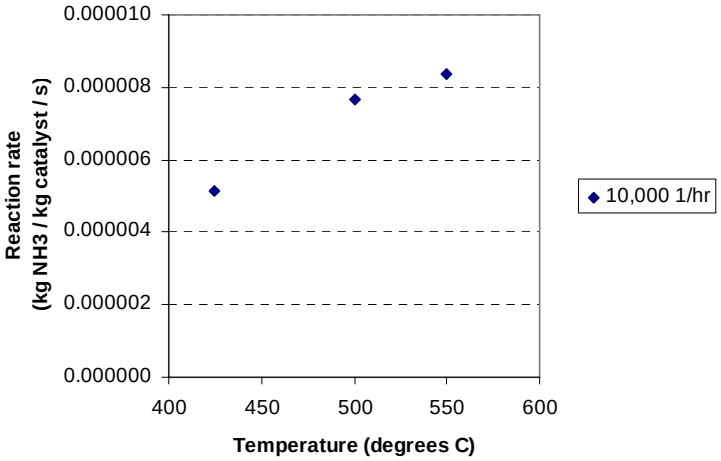

Figure 7: NH_3 reaction rate is shown versus temperature.

In Figures 8 and 9, NH_3 production is shown versus pressure. The experimentally determined reaction rate was compared to previously reported reaction rates by Süd-Chemie and it was found that the experimental data aligned with the expected trend. As shown in Figure 9, as pressure decreases, the catalyst performance tends to decreases linearly until a critical point is reached where the rate at which the reaction rate decreases begins to increase non-linearly. In

Figure 9, the wustite catalyst is compared with the magnetite catalyst, and demonstrates much better performance at lower pressures.

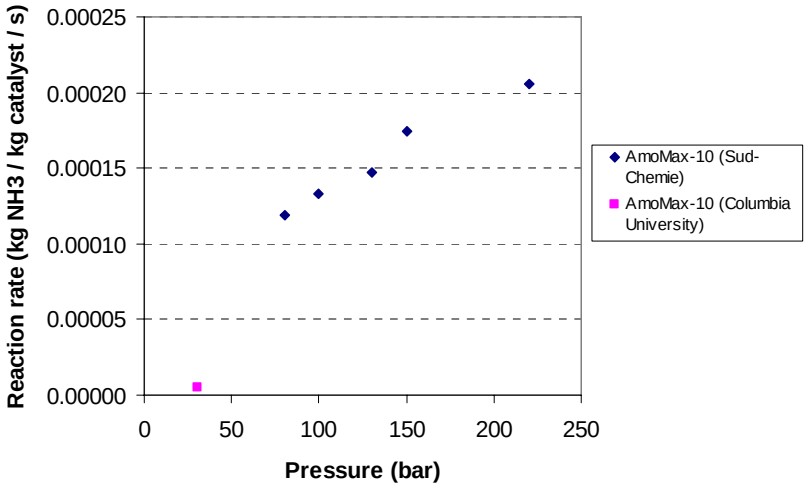

Figure 8: Reaction rates for the Süd-Chemie Amomax iron catalyst are shown versus pressure at 425 degrees Celsius. The experimental data provided by Süd-Chemie align with the expected trend connecting to experimental data acquired in this experiment.

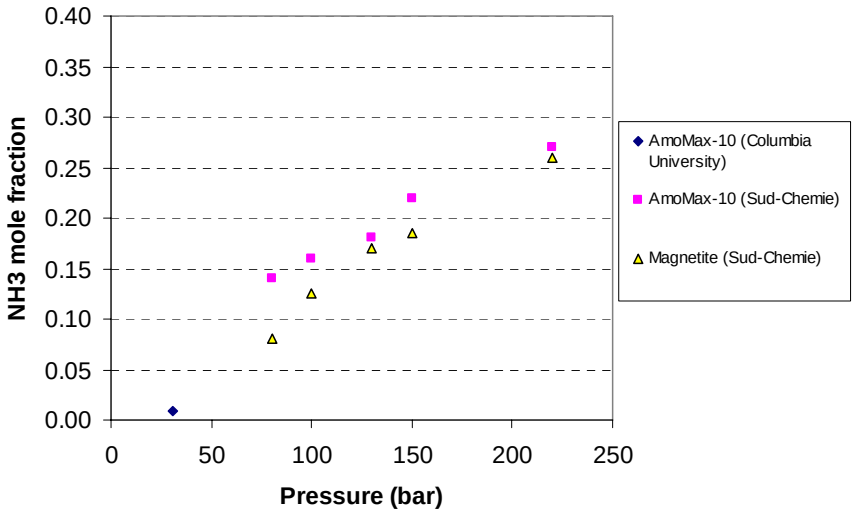

Figure 9: NH_3 mole fraction is shown versus pressure for different iron-based catalysts at a temperature of 425 degrees Celsius.

Figures 10 and 11 demonstrate effluent NH_3 mole fraction and NH_3 reaction rate versus temperature at a pressure of 150 bar and space velocity of 15,000 1/hr. For the AmoMax-10 catalyst, NH_3 output meets the thermodynamic equilibrium at 435 degrees Celsius.

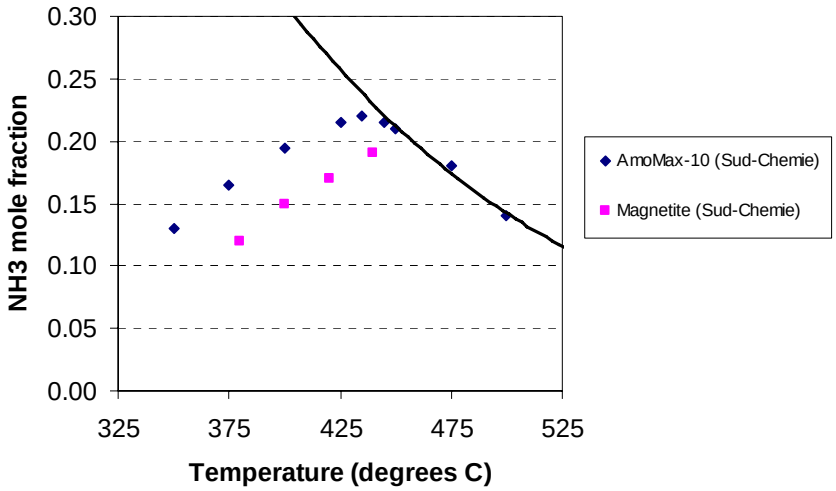

Figure 10: NH_3 mole fraction versus temperature for different iron-based catalysts at 150 bar and 15,000 1/hr, provided by Süd-Chemie. The solid line represents the thermodynamic equilibrium.

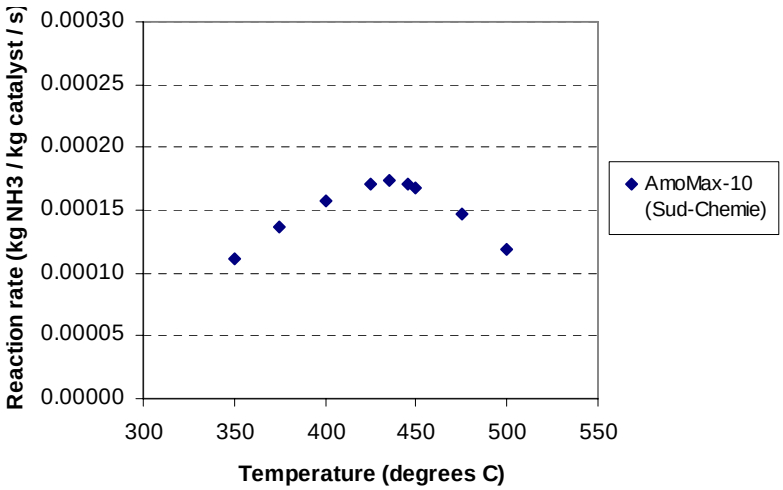

Figure 11: Reaction rate versus temperature for AmoMax-10 catalyst at 150 bar and 15,000 1/hr, provided by Süd-Chemie.

Finally, in Figures 12 and 13 and in Tables 1 and 2, a catalytic ammonia synthesis reactor is scaled to decompose 100 tons of ammonia over 72 hours (0.35 kg/s). In Figure 12, it is demonstrated that a minimum reactor size is reached at a temperature of about 435 degrees

Celsius. In Figure 13, it is shown that an optimal reactor would operate at about 150 bar, before diminishing marginal returns are seen with increasing pressure further. Table 1 summarizes results with respect to reactor size and weight. In order to synthesize ammonia at a rate of 0.35 kg/s at 150 bar, 435 degrees Celsius, and a space velocity of 15,000 1/hr, a 0.67 m^3 catalyst bed weighing 2.2 tons would be needed. Table 2 shows reaction rates and reactor sizes calculated from literature in which experiments were performed to compare the efficiency of different catalyst formulations, including Ruthenium based catalysts.

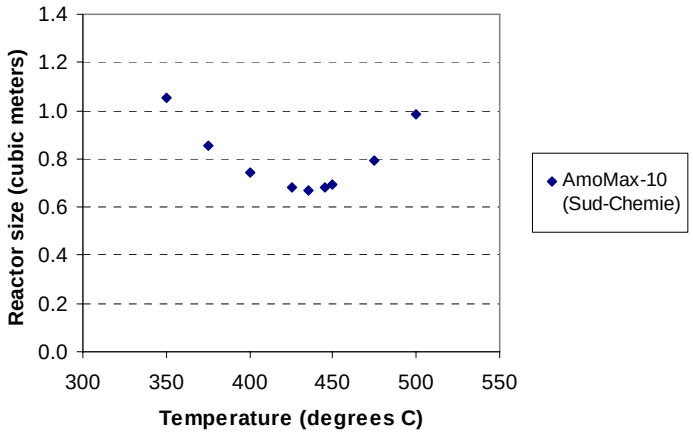

Figure 12: For a system which synthesizes 100 tons of NH_3 over 72 hours at a pressure of 150 bar and space velocity of 15,000 1/hr, reactor size is shown versus temperature.

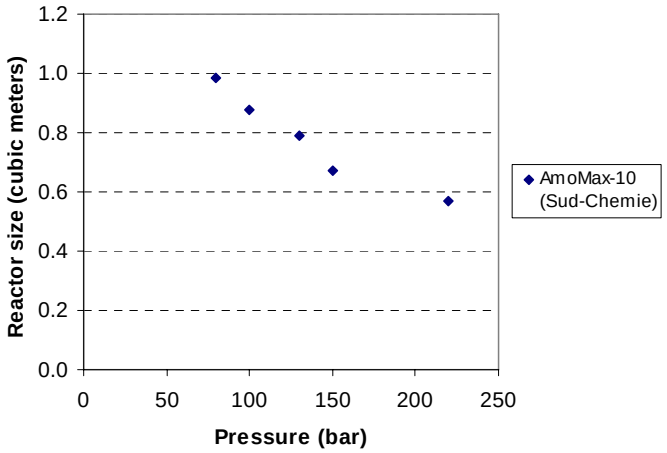

Figure 13: For a system which synthesizes 100 tons of NH_3 over 72 hours at 425 degrees C and space velocity of 15,000 1/hr, reactor size is shown versus pressure.

Table 1: Dependence of NH_3 reaction rates, reactor size, and reactor weight on pressure, temperature, and space velocity. Reactor size and weight are scaled to synthesize 100 tons of ammonia over 72 hours. Reaction rates at 31 bar were determined experimentally, while reaction rates at 150 bar were calculated from results in literature provided by Süd-Chemie.

Pressure (bar)	Temperature (degrees C)	Space Velocity (1/hr)	NH_3 reaction rate (kg NH_3 / kg catalyst / s)	Reactor Size (cubic meters)	Reactor Weight (tons)
31	425	10000	5.14E-06	22.7	75
31	500	10000	7.64E-06	15.3	50
31	550	10000	8.35E-06	14	46
150	400	15000	1.57E-04	0.74	2.5
150	435	15000	1.74E-04	0.67	2.2
150	475	15000	1.47E-04	0.79	2.6

Table 2: Dependence of NH_3 reaction rates and reactor sizing on catalyst formulation, temperature, pressure, and space velocity. Reactor size is scaled to synthesize 100 tons of ammonia over 72 hours. Data was taken from literature and calculations were performed to determine reaction rates and reactor size.

Catalyst	Temperature (degrees C)	Pressure (bar)	Space Velocity (1/hr)	Reaction Rate (kg NH3 / m^3 catalyst / s)	Reactor Size (cubic meters)
Cs-Ba-Ru/C	430	140	--	0.17	2.1
Iron	430	140	--	0.08	4.2
Ru/MgO	510	50	14000	0.13	2.7
Cs-Ru/MgO	392	50	14000	0.15	2.3
Ba-Ru/MgO	411	50	16000	0.35	1.0
Iron	450	107	16000	0.36	0.97

3. Ammonia Decomposition

3.1 Introduction

Experiments were completed using a stainless steel bulkhead flow-reactor to determine the performance of $NiO/CaO/Al_2O_3$ and Rh/Al_2O_3 catalysts with respect to their ability to decompose ammonia (NH_3) into nitrogen (N_2) and hydrogen (H_2). The purpose of these experiments was to determine the relationship between the conversion efficiency of a given catalyst with the operating temperature of the decomposition reactor. This data is then used to extrapolate the size and performance of a Walrus reference vehicle system.

Two different catalyst formulations were compared in these experiments. The first catalyst was designed by Süd-Chemie Inc. and recommended by engineers in the catalyst division to fulfill the goals of these experiments. The product name of the spherical catalysts with diameter ranging from 2-4 mm is G-90 and contains the chemical formulation $NiO/CaO/Al_2O_3$. In terms of weight percent, the catalyst is 57-87 % aluminum oxide, 10-25 % nickel oxide, and 3-18 % calcium oxide. The density of the catalyst, in terms of the mass contained inside a fixed packed bed with volume approximated as a cylinder, was measured to be 1.04 g/cm^3. A one-liter sample of the catalyst was obtained at a cost of $500 from Süd-Chemie.

The second catalyst tested, from Engelhard Corp., was a Rh/Al_2O_3 monolith. This catalyst was 4 % Rh by weight, and was measured to have a density of 0.44 g/cm^3 in terms of a fixed monolith with the volume approximated as a cylinder. The Rh monoliths were donated from Engelhard Corp. by Dr. Robert Farrauto but can be purchased at an estimated price of $2,600/liter.

The primary results, discussed in detail in the **Results** section, are that the catalyst performed as expected in terms of reaction rates of NH_3 decomposition. All goals were met in terms of time and performance.

3.2 Experimental Setup

The ammonia decomposition reactor is shown in a schematic in Figure 1. It consists of a stainless steel bulkhead reactor core, loaded with either pellets or a monolith catalyst, inside of a two-stage furnace. The furnace temperature was controlled via two Variac voltage transformers. K-type thermocouples were imbedded directly inside of the catalyst bed and downstream of the bed, and temperature readings were acquired with an Omega OMB-DAQ-54 data acquisition system. The mass flow rate of each inlet gas into the reactor was controlled with Aalborg mass flow controllers of model number GFC17, which were fed gas from cylinders of pure anhydrous ammonia, argon, and hydrogen. The outlet flow from the catalytic reactor was sent to an Agilent 3000 Micro GC instrument to analyze the concentrations of particular species in the outlet stream and finally vented to a hood.

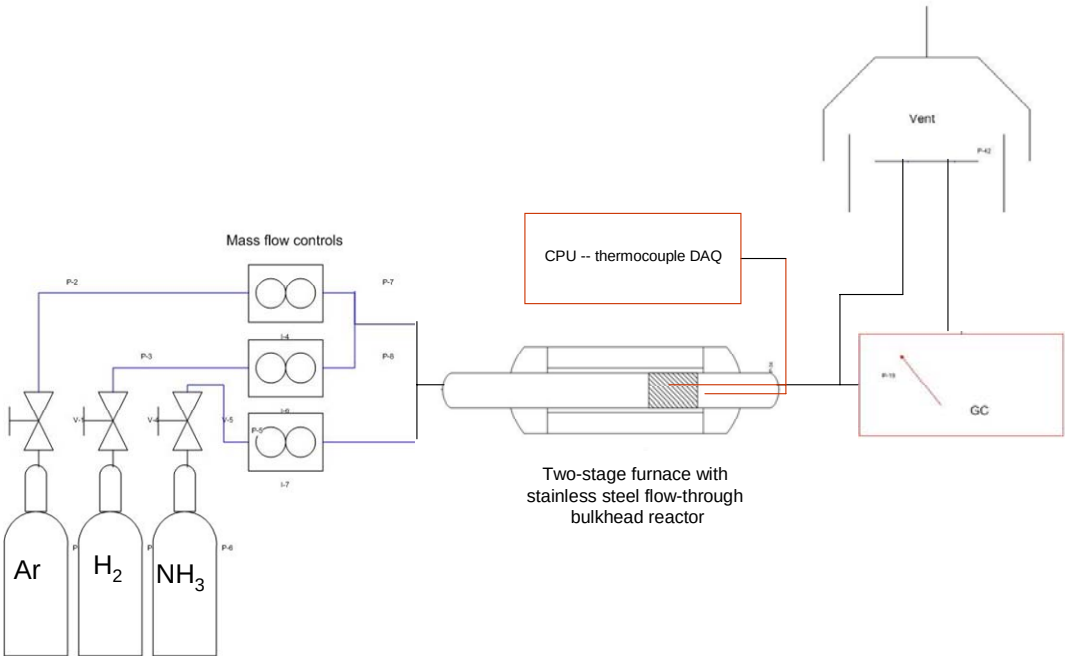

Figure 1: Schematic of ammonia decomposition system.

Figure 2: Two-stage furnace opened to show stainless steel bulkhead reactor. Beneath the furnace are the Variac voltage controllers as well as the Omega data acquisition hardware to acquire temperature readings.

Figure 3: Aalborg GFC17 mass flow controllers.

Figure 4: Agilent 3000 Micro GC and notebook computer to acquire gas chromatograph data.

3.3 Experimental Procedure

14. Reactor assembly.

a. Thermocouples were inserted into stainless steel bulkhead reactor such that the first thermocouple was centered radially in the reactor and imbedded 1 cm into the catalyst bed axially, and the second was 3.54 cm downstream from the first thermocouple, also centered radially.

b. The bulkhead reactor was loaded with 2 cm of pellets (5.7 cm^3) or with a 1.2 cm long monolith (3.42 cm^3).

    i. If using pellets, a non-catalytic wire mesh was used to pack the bed tight so that there was no bypass.

c. The reactor was placed inside the furnace such that the catalyst bed began at a point 47 cm downstream into furnace where it was experimentally determined that the furnace provided a constant temperature profile for a distance greater than the catalyst bed.

15. Tube connections were checked from gas cylinders to mass flow controllers (MFCs), from the MFCs to the connecting tee, from the tee to the reactor, and from the reactor to the hood. The line from the reactor outlet to the GC was left unattached initially so that outlet from the pre-reduction step was vented directly to the hood.

16. The MFCs were plugged in to warm up; the local setpoints on the units were checked to be set at zero ml/min of outlet flow.

    a. After 30 minutes of warming up, the valves at the gas cylinders were opened to provide a pressure of about 25-40 psi to the MFCs while leaving the outlet flow off.

17. The two-stage furnace was turned on (the Variacs were set high initially to gain the first 400 degrees C, then backed off to the appropriate setting on the Variac to gain rest of the heat).
18. Pre-reduction.
    a. Once the furnace reached steady state at 500 degrees C in the catalyst bed, the local setpoints on the MFCs were adjusted such that a mixture of 200 ml/min Ar and 25 ml/min H_2 were flowed into the reactor for 1 hr to pre-reduce the catalyst.
    b. The H_2 flow was then turned off via the MFC setpoint, and the H_2 tube from the MFC to the inlet tee was unscrewed at the tee and capped.
    c. The system was flushed with 200 ml/min Ar for 30 minutes.
19. A tube connecting the outlet flow from the reactor to the GC was attached.
20. The connection at the inlet tee was switched from the Ar tube to the NH_3 tube.
21. NH_3 was fed in at the lowest flowrate (100ml/min for pellets or 60 ml/min for monolith) until no Argon is seen on chromatogram (at least 60 minutes).
22. When steady state was reached at the first chosen temperature and space velocity, sampling with the GC was initiated.
    a. When the GC turned on to take a sample, temperature was recorded. Since the thermocouple reading was instantaneous but the GC sample was taken after the gas had traveled approximately 10 m downstream through 1/8 inch ID tubing, there was a short time lag (approximately 2 minutes) between the temperature readings and the GC sample. But, if steady state conditions were met for a time greater than the lag time, a correction for the offset was not needed.

b. As many samples were taken as needed to ensure that the system was in steady state.

23. NH_3 flowrate was then increased to achieve the next desired space velocity. The Variak was adjusted to reach the same temperature in the catalyst bed as seen with previous run.
24. When steady state was reached again with the new flowrate, sampling resumed with the GC. This procedure was repeated at different flowrates (space velocities) while maintaining the same catalyst temperature.
25. Once sampling was exhausted at a particular temperature, NH_3 flow was reduced back to the initial space velocity.
26. The Variac was adjusted to attain steady state at the next highest temperature, and the GC samplings repeated at the same space velocities as sampled previously.
27. The Variac was adjusted to attain steady state at the next highest temperature, and the GC samplings were repeated at the same space velocities as sampled previously.
28. Once three temperatures were tested with varying space velocities, the furnace was shut down, the system was flushed with argon for 30 minutes, and the MFCs were powered down.

3.4 Calculations

Prior to data collection, the Micro GC was calibrated to provide a correlation between the area under a chromatogram peak of a particular gas and its concentration in mole fraction. An example of the linear correlation is seen in Figure 5. A linear trendline and equation was fit to the calibration data so that a particular area would correlate to a particular mole fraction when the outlet gas from the reactor was sampled.

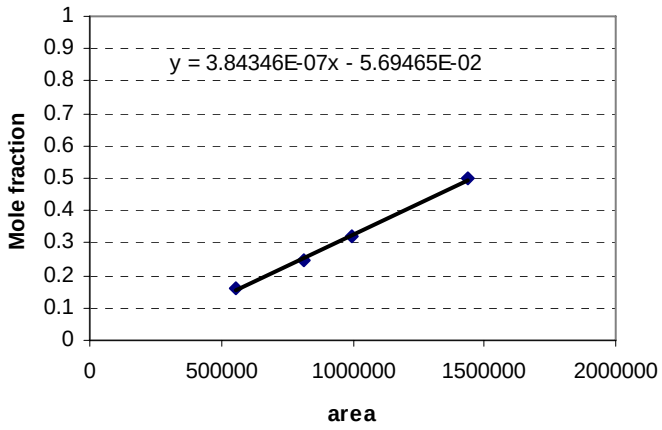

Figure 5: A sample GC calibration for N_2. The equation for the line of best fit provides a simple correlation between area under the N_2 peak of the chromatogram and its mole fraction.

An example of the calculations which provide mole fractions from the data acquired from the Micro GC are seen in Table 1. When ammonia is present in a molar fraction of about 25 %, the equation y = (3.6395E-07)*(*area*)+(7.7897E-02) serves as a reasonable linear correlation to calculate the exact molar fraction. At much smaller concentrations, another equation is used to provide a better fit.

Table 1: Sample calculations for the concentration of NH_3 at a particular space velocity and temperature. The mean average and standard deviation was taken from the calculations of mole fraction.

Temp (oC)	Flow rate (ml/min)	Space velocity (ml NH_3 STP/cm^3 catalyst/hr)	Area of NH3 from GC	Concentration of NH3 (mole fraction)	Avg.	St. dev.
				y = (3.6395E-07)*(area)+(7.7897E-02)		
505.8	100	1053	484132	0.2595	0.2578	0.0017
505.9	100	1053	484295	0.2596		
505.9	100	1053	482498	0.2588		
506.3	100	1053	476006	0.2561		
506.4	100	1053	476981	0.2566		
506.5	100	1053	475410	0.2559		

3.5 Results

Figures 6, 7, and 8 show a direct comparison between the performance of the different catalysts at 505, 575, and 615 °C, respectively. The data in these figures show that the nickel based catalyst has superior performance at low space velocities, for all temperatures, but has similar or poorer performance compared to the rhodium based catalyst at higher space velocities, for all temperatures.

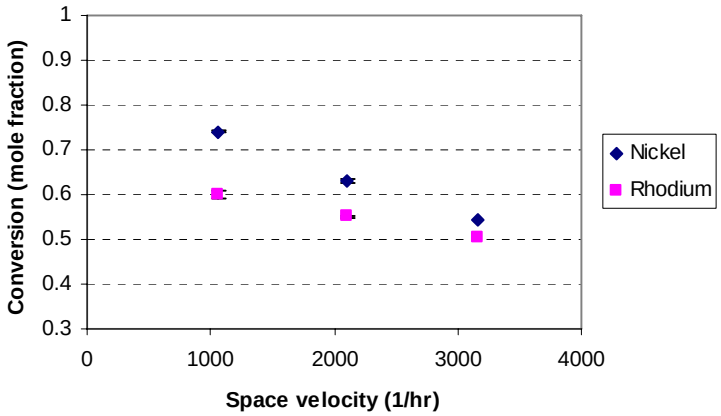

Figure 6: Dependence of conversion of ammonia (in mole fractions decomposed) on the space velocity (ml NH_3 STP / cm^3 catalyst / hr) for a reactor core temperature of 505 °C. Y-error bars represent standard deviations.

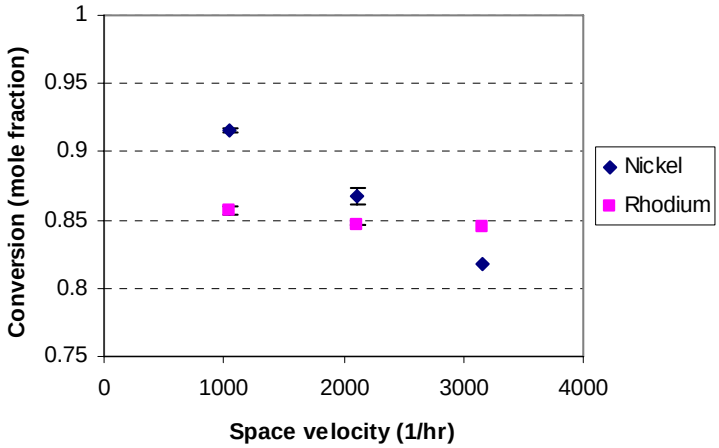

Figure 7: Dependence of the conversion of ammonia (in mole fraction decomposed) on the space velocity for a reactor core temperature 575 °C. Y-error bars represent standard deviations.

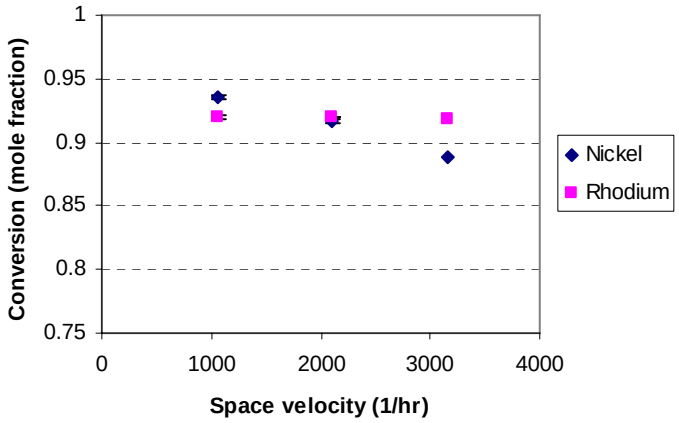

Figure 8: Dependence of the conversion of ammonia (in mole fraction decomposed) on the space velocity for a reactor core temperature 615 °C. Y-error bars represent standard deviations.

Figures 9, 10, and 11 show the dependence of the individual species concentrations at the reactor outlet on the space velocity for the nickel catalyst, for temperatures of 505, 575, and 615 °C. The data match the anticipated trends, in that nitrogen and hydrogen mole fractions decrease as the ammonia decomposition rate decreases. Figures 12, 13, and 14 show similar data for the rhodium catalyst, and this data matches the anticipated trends as well.

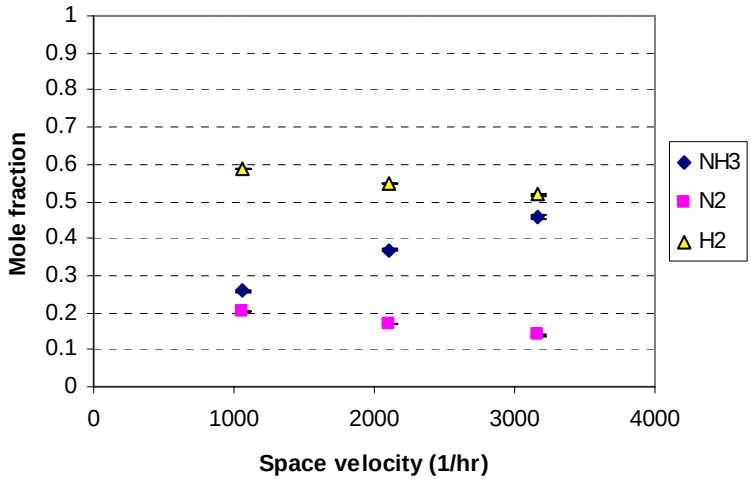

Figure 9: Dependence of the individual species mole fractions on the space velocity for a reactor core temperature 505 °C, nickel catalyst. Y-error bars represent standard deviations.

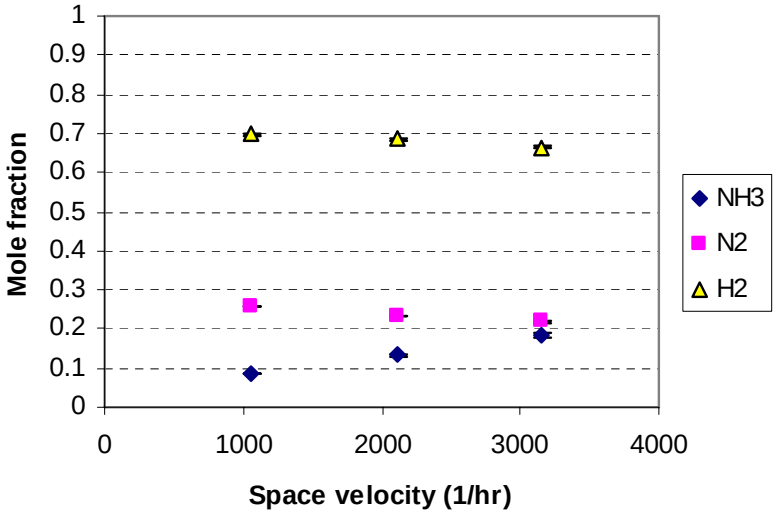

Figure 10: Dependence of the individual species mole fractions on the space velocity for a reactor core temperature 575 °C, nickel catalyst. Y-error bars represent standard deviations.

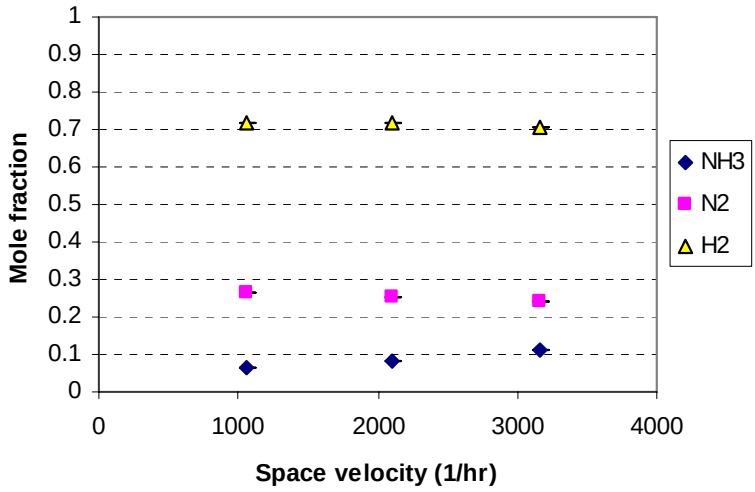

Figure 11: Dependence of the individual species mole fractions on the space velocity for a reactor core temperature 615 °C, nickel catalyst. Y-error bars represent standard deviations.

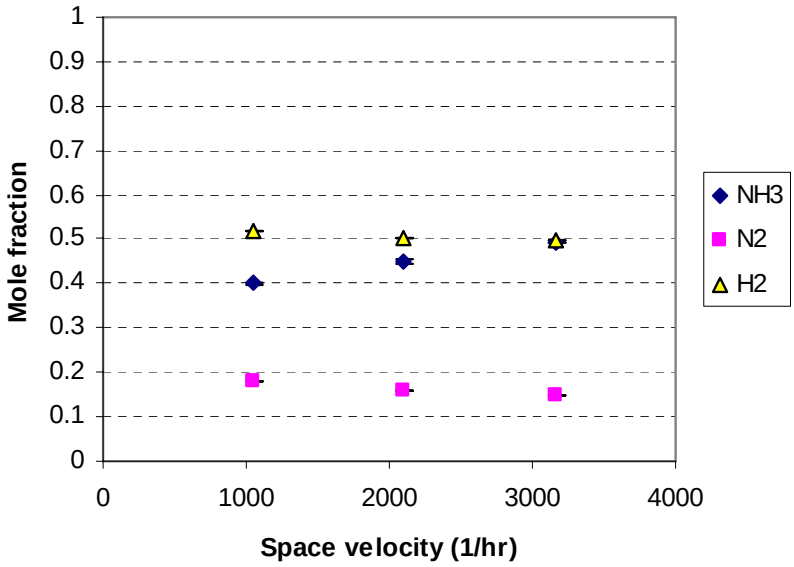

Figure 12: Dependence of the individual species mole fractions on the space velocity for a reactor core temperature 505 °C, Rhodium catalyst. Y-error bars represent standard deviations.

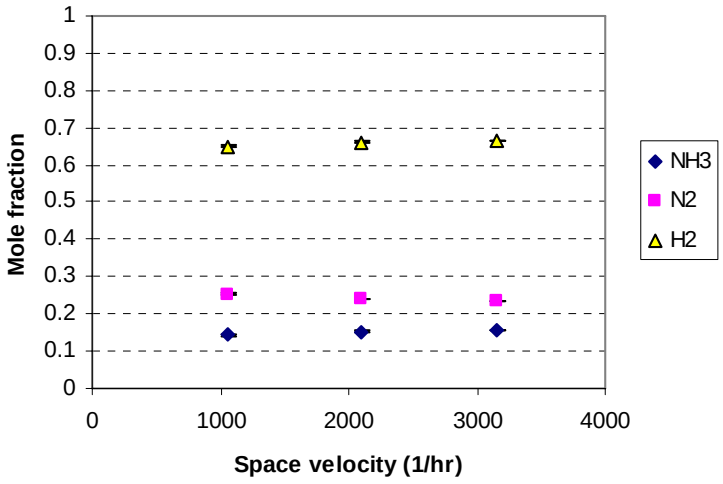

Figure 13: Dependence of the individual species mole fractions on the space velocity for a reactor core temperature 575 °C, rhodium catalyst. Y-error bars represent standard deviations.

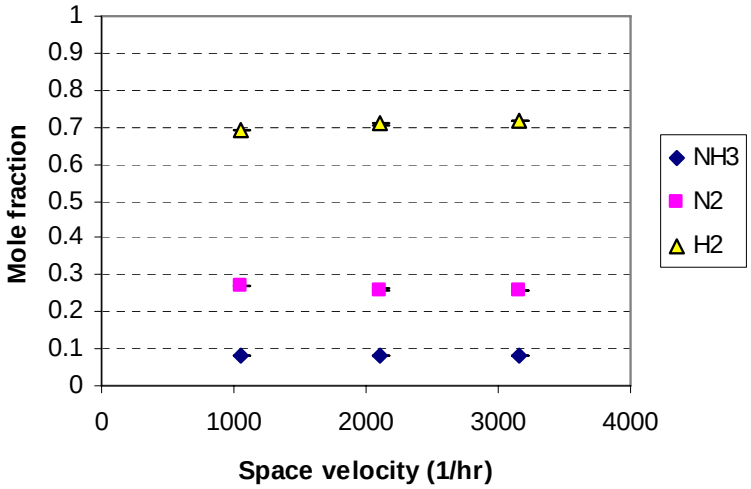

Figure 14: Dependence of the individual species mole fractions on the space velocity for a reactor core temperature 615 °C, rhodium catalyst. Y-error bars represent standard deviations.

The next set of data, plotted in Figures 15 and 16, shows the performance of the nickel and rhodium catalysts, respectively, over nearly four hours of operation. The data show that the catalyst activity held reasonably steady during the experimental period, thus any reducing of the

catalyst (burning away of the oxides during initial use) is negligible and the catalyst performance can be assumed to be steady state.

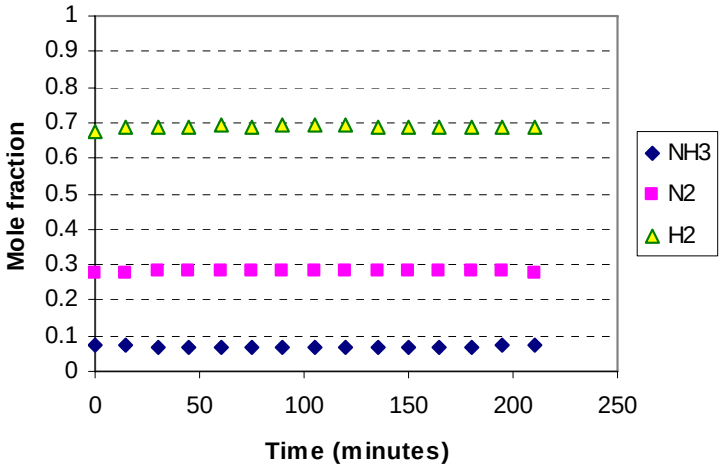

Figure 15: Dependence of the effluent molar fractions of ammonia, nitrogen, and hydrogen with time for the nickel catalyst at 575 °C and a space velocity of 790 (1/hr).

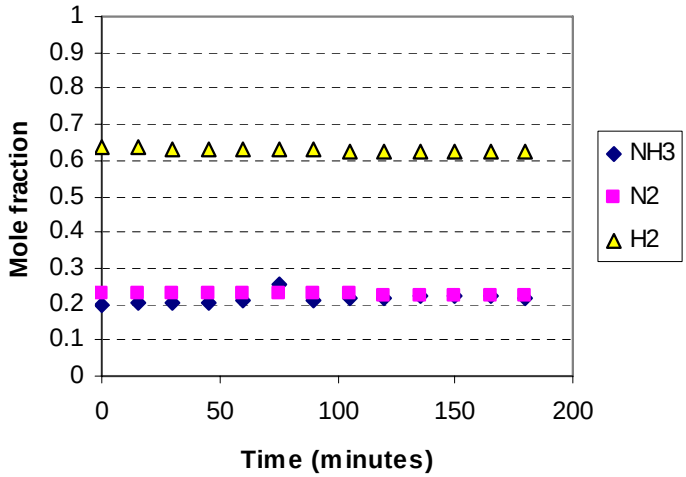

Figure 16: Dependence of the effluent molar fractions of ammonia, nitrogen, and hydrogen with time for the rhodium catalyst at 550 °C and a space velocity of 2100 (1/hr).

In Figures 17 and 18, the reaction rate for ammonia decomposition is shown versus temperature for the nickel and rhodium catalysts. The rhodium catalyst demonstrates higher

reaction rates than the nickel catalyst at each process condition in terms of grams ammonia decomposed per second per gram catalyst.

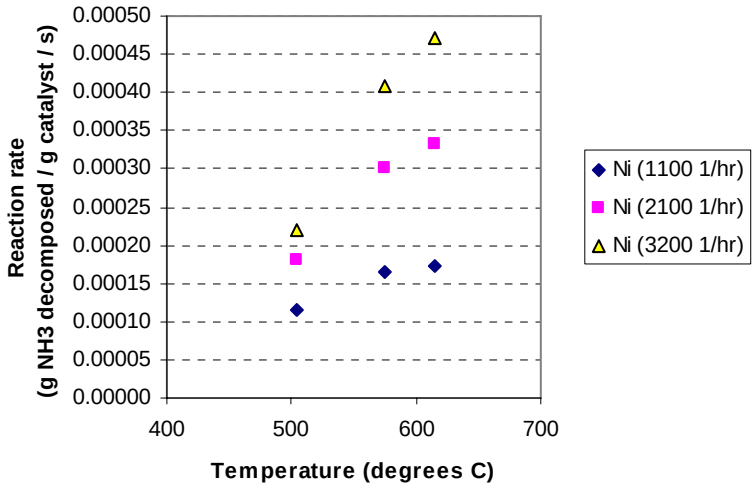

Figure 17: Dependence of the reaction rate for ammonia decomposition on temperature at varying space velocities for the nickel catalyst.

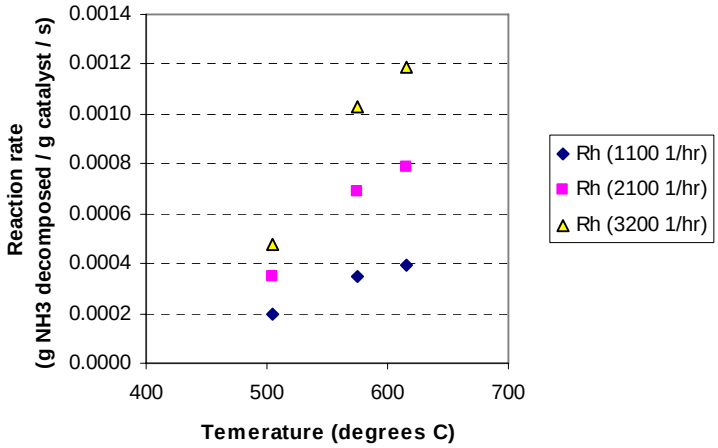

Figure 18: Dependence of the reaction rate for ammonia decomposition on temperature at varying space velocities for the rhodium catalyst.

Finally, in Table 2, an ammonia decomposition reactor was scaled to decompose 100 tons of ammonia over 72 hours (a rate of 0.35 kg/s) at each tested process condition. Corresponding hydrogen synthesis rates are also shown. In order to meet the desired rate of 0.35 kg NH_3

decomposed per second at 615 °C and a space velocity of 3200 1/hr, a nickel-based reactor would need to be 0.72 m^3 and would weigh 0.82 tons, while a rhodium based reactor would be 0.67 m^3 and would weigh only 0.33 tons.

Table 2: Dependence of hydrogen production rates, ammonia decomposition rates, and reactor size and weight on catalyst type, temperature, and space velocity. Reactor size and weight are scaled to decompose 100 tons of ammonia over 72 hours. Weight of Ni catalyst = 5.9 g and weight of Rh catalyst = 1.5 g.

Catalyst (base metal)	Temperature (degrees C)	Space Velocity (ml NH_3 STP/ cm^3 catalyst/hr)	H_2 synthesis rate (L H_2 STP/ g catalyst/s)	NH_3 decomposition rate (g NH_3 decomposed/ g catalyst/s)	Reactor Size (cubic meters)	Reactor Weight (tons)
Ni	505	1100	0.00025	0.00011	2.92	3.35
Ni	505	2100	0.00039	0.00019	1.87	2.14
Ni	505	3200	0.00047	0.00022	1.54	1.76
Rh	505	1100	0.00043	0.00020	4.00	1.94
Rh	505	2100	0.00076	0.00035	2.26	1.10
Rh	505	3200	0.00103	0.00048	1.67	0.81
Ni	575	1100	0.00036	0.00017	2.04	2.34
Ni	575	2100	0.00065	0.00030	1.12	1.28
Ni	575	3200	0.00088	0.00040	0.83	0.95
Rh	575	1100	0.00075	0.00035	2.27	1.10
Rh	575	2100	0.00147	0.00069	1.16	0.56
Rh	575	3200	0.00220	0.00103	0.77	0.38
Ni	615	1100	0.00037	0.00017	1.94	2.22
Ni	615	2100	0.00072	0.00034	1.01	1.16
Ni	615	3200	0.00101	0.00047	0.72	0.82
Rh	615	1100	0.00085	0.00040	2.01	0.98
Rh	615	2100	0.00170	0.00079	1.01	0.49
Rh	615	3200	0.00255	0.00119	0.67	0.33

LITERATURE CITED

1. EPA, *Landfill Methane Outreach Program.* 2006.
2. Themelis, N.J., *The environmental impacts: Assessing waste-to-energy and landfilling in the US.* Waste Management World, 2002: p. 35-41.
3. Themelis, N.J. and P.A. Ulloa, *Methane generation in landfills.* Renewable Energy, 2006. **32**(7): p. 1243-1257.
4. Weitz, K.A., et al., *The impact of municipal solid waste management on greenhouse gas emissions in the United States.* Journal of the Air & Waste Management Association, 2002. **52**(9): p. 1000-1011.
5. Administration, E.I., *Emissions of Greenhouse Gases in the United States 2003.* Comparison of global warming potentials from the IPCC's second and third assessment reports, 2003.
6. W. Qin, F.N.E., T.T. Tsotsis, *Fundamental and environmental aspects of landfill gas utilization for power generation.* Chemical Engineering Journal, 2001. **82**: p. 157-172.
7. Richardson, J.T. and S.A. Paripatyadar, *Carbon dioxide reforming of methane with supported rhodium.* Applied Catalysis, 1990. **61**(2): p. 293-309.
8. Wang, S., G.Q. Li, and G.J. Millar, *Carbon Dioxide Reforming of Methane To Produce Synthesis Gas over Metal-Supported Catalysts: State of the Art.* Energy & Fuels, 1996. **10**(4): p. 896-904.
9. Fischer, F. and H. Tropscii, *Conversion of methane into hydrogen and carbon monoxide.* Brennstoff-Chemie, 1928. **9**: p. 39-46.
10. Bodrov, I.M. and L.O. Apel'baum, *Reaction kinetics of methane and carbon dioxide on a nickel surface.* Kinetika i Kataliz, 1967. **8**(2): p. 379-82.
11. Rostrup-Nielsen, J.R., *Equilibriums of decomposition reactions of carbon monoxide and methane over nickel catalysts.* Journal of Catalysis, 1972. **27**(3): p. 343-56.
12. Rostrup-Nielsen, J.R., *Production of synthesis gas.* Catalysis Today, 1994. **18**(4): p. 305-24.
13. Erdohelyi, A., J. Cserenyi, and F. Solymosi, *Activation of methane and its reaction with carbon dioxide over supported rhodium catalysts.* Journal of Catalysis, 1993. **141**(1): p. 287-99.
14. Rostrup-Nielsen, J.R. and J.H. Bak Hansen, *Carbon dioxide-reforming of methane over transition metals.* Journal of Catalysis, 1993. **144**(1): p. 38-49.
15. Zhang, Z.L., et al., *Reforming of methane with carbon dioxide to synthesis gas over supported rhodium catalysts. I. Effects of support and metal crystallite size on reaction activity and deactivation characteristics.* Journal of Catalysis, 1996. **158**(1): p. 51-63.
16. Sigl, M., et al., *CO2 reforming of methane over vanadia-promoted Rh/SiO2 catalysts.* Topics in Catalysis, 1999. **8**(3,4): p. 211-222.
17. Ranganathan, E., *Methanol steam reforming over Pd/ZnO and Pd/CeO2 catalysts.* Applied Catalysis A: General, 2005. **289**(2): p. 153-162.
18. Noronha, F.B., *Correlation between catalytic activity and support reducibility in the CO2 reforming of CH4 over Pt/CexZr1-xO2 catalysts.* Chemical Engineering Journal, 2001. **82**: p. 21-31.
19. Wei, J. and E. Iglesia, *Structural requirements and reaction pathways in methane activation and chemical conversion catalyzed by rhodium.* Journal of Catalysis, 2004. **225**(1): p. 116-127.